

# Attosecond chronoscopy of photoemission

Renate Pazourek,<sup>\*</sup> Stefan Nagele,<sup>†</sup> and Joachim Burgdörfer<sup>‡</sup>

*Institute for Theoretical Physics, Vienna University of Technology, 1040 Vienna, Austria, EU*

(published 12 August 2015)

Recent advances in the generation of well-characterized subfemtosecond laser pulses have opened up unpredicted opportunities for the real-time observation of ultrafast electronic dynamics in matter. Such attosecond chronoscopy allows a novel look at a wide range of fundamental photophysical and photochemical processes in the time domain, including Auger and autoionization processes, as well as photoemission from atoms, molecules, and surfaces, complementing conventional energy-domain spectroscopy. Attosecond chronoscopy raises fundamental conceptual and theoretical questions as to which novel information becomes accessible and which dynamical processes can be controlled and steered. Several of these questions, currently a matter of lively debate, are addressed in this review. The focus is placed on one prototypical case, the chronoscopy of the photoelectric effect by attosecond streaking. Is photoionization instantaneous or is there a finite response time of the electronic wave function to the photoabsorption event? Answers to this question turn out to be far more complex and multifaceted than initially thought. They touch upon fundamental issues of time and time delay as observables in quantum theory. Recent progress of our understanding of time-resolved photoemission from atoms, molecules, and solids is reviewed. Unresolved and open questions are highlighted and future directions are discussed addressing the observation and control of electronic motion in more complex nanoscale structures and in condensed matter.

DOI: [10.1103/RevModPhys.87.765](https://doi.org/10.1103/RevModPhys.87.765)

PACS numbers: 32.80.Fb, 42.50.Hz, 42.65.Re, 33.80.–b

## CONTENTS

I. Introduction	765
II. Time and Time Delay as Observables in Photoemission	766
A. <i>S</i> matrix and reduced density matrix for photoemission	767
B. Time-delay operator	769
C. Photoionization from a model atom	771
III. Coulomb Scattering and Coulomb Time Delay	772
IV. Attosecond Streaking of Photoemission	775
A. Streaking principle	775
B. Attosecond streaking for short-ranged potentials	777
C. Streaking in the presence of a Coulomb field	778
D. Dipole-laser coupling	780
V. Time-resolved Photoionization of Many-electron Atoms	781
VI. Time-resolved Photoionization of Molecules	785
VII. Time-resolved Photoemission from Surfaces	789
VIII. Time Ordering in Two-photon Double Ionization	791
IX. Attosecond Streaking of Tunneling Time?	794
X. Concluding Remarks	797
Acknowledgments	797
References	797

## I. INTRODUCTION

Following electronic dynamics in real time, watching the formation or breaking of chemical bonds, the transfer of electrons from one constituent to another, or the ejection of electrons from an atom or molecule has been a dream and challenge of time-resolved quantum physics for a long time.

The extent to which such ultrafast processes are accessible to measurements at all has remained a matter of debate. Observing the temporal electronic evolution requires interrogation of the system on ultrafast time scales. Yet such probes are subject to both time-energy and position-momentum uncertainty. Moreover, they are prone to distortion of the very evolution that is to be observed.

On an even more fundamental level, the question is posed as to whether and how time-domain information, referred to in the following as chronoscopy, can add to and complement the information accessible through high-resolution spectroscopy, i.e., time-integral measurements in the energy domain. Pioneered by the advances in femtosecond chemistry (Rosker, Dantus, and Zewail, 1988; Zewail, 1988, 2000a, 2000b) the application of ultrafast laser technology to atoms, molecules, nanostructures, and solid surfaces has revolutionized the time-honored field of photoelectron spectroscopy. Observation of the motion of atomic constituents on their natural time scale came into reach. While for resolving the atomic motion in molecules in time, for example, by creating and taking snapshots of a vibronic wave packet, laser pulses with a duration of several femtoseconds ( $10^{-15}$  s) are sufficient, accomplishing a similar feat for the electronic motion in atoms, molecules, or condensed matter requires subfemtosecond, that is attosecond (as), time resolution ( $1 \text{ as} = 10^{-18} \text{ s}$ ). Advances during the last decade in the development of phase-controlled few-cycle infrared (IR) laser pulses (cycle period  $T_{\text{IR}} \approx 2.7 \text{ fs}$  at  $\lambda = 800 \text{ nm}$ ) and  $\sim 100$  as extreme ultraviolet (XUV) pulses, temporally well correlated with each other through the underlying high-harmonic generation (HHG) process (Drescher *et al.*, 2001; Hentschel *et al.*, 2001; Paul *et al.*, 2001), have opened up the possibility to observe and to control electronic dynamics in matter in real

<sup>\*</sup>renate.pazourek@tuwien.ac.at

<sup>†</sup>stefan.nagele@tuwien.ac.at

<sup>‡</sup>joachim.burgdoerfer@tuwien.ac.at

time and have developed into a new field called attosecond physics [see, e.g., Agostini and DiMauro (2004), Reider (2004), Scrinzi *et al.* (2006), Bucksbaum (2007), Corkum and Krausz (2007), Kling and Vrakking (2008), Krausz and Ivanov (2009), Chang (2011), Gallmann, Cirelli, and Keller (2012), Plaja, Torres, and Zair (2013), Schultz and Vrakking (2013), Kim, Villeneuve, and Corkum (2014), Krausz and Stockman (2014), Lepine, Ivanov, and Vrakking (2014), and Peng *et al.* (2015) for reviews of the subject]. Previously, time-resolved electronic dynamics was accessible only for highly excited states. In such Rydberg states with quantum numbers  $n \gg 1$ , the intrinsic time scale given by the period of a Bohr orbit  $\tau_n = 150 \text{ as} \times n^3$  reaches picoseconds (for  $n \approx 30$ ) or even nanoseconds (for  $n \approx 300$ ) and can be conveniently interrogated by microwave pulses (Gallagher, 2005) or electric pulses from arbitrary-form pulse generators (Dunning *et al.*, 2009). Only with the advent of attosecond pulses, time-resolved dynamics near the ground state ( $n \approx 1$ ) and deep into the quantum regime came into reach.

Currently available tools are mostly based on pump-probe-like settings combining a  $\sim 100$  as XUV pulse as a pump with a phase-controlled IR pulse as a probe. They include the attosecond streaking technique (Drescher *et al.*, 2001; Hentschel *et al.*, 2001; Itatani *et al.*, 2002; Kienberger *et al.*, 2004; Yakovlev, Bammner, and Scrinzi, 2005; Sansone *et al.*, 2006) and RABBIT (reconstruction of attosecond harmonic beating by interference of two-photon transitions) (Véniard, Taïeb, and Maquet, 1996; Paul *et al.*, 2001; Muller, 2002; Toma and Muller, 2002; Haessler *et al.*, 2009; Caillat *et al.*, 2011; Klünder *et al.*, 2011). The roles of pump and probe are reversed in attosecond transient absorption (ATA) (Goulielmakis *et al.*, 2010; Wang *et al.*, 2010; Gaarde *et al.*, 2011; Holler *et al.*, 2011; Santra *et al.*, 2011; Chen *et al.*, 2012, 2013; Pabst *et al.*, 2012; Gallmann *et al.*, 2013; Ott *et al.*, 2013, 2014; Beck, Neumark, and Leone, 2015) where the IR pulse creates the wave packet while the modulation of the absorption of the attosecond XUV pulse probes the time evolution of the electronically excited system. A promising variant of attosecond streaking is the so-called attosecond clock (“attoclock”) (Eckle, Pfeiffer *et al.*, 2008; Eckle, Smolarski *et al.*, 2008; Pfeiffer *et al.*, 2011, Pfeiffer *et al.*, 2013; Pfeiffer, Cirelli *et al.*, 2011) or angular streaking which employs a near-circularly rather than a linearly polarized IR field. Up to now, experiments in which the excitation by an attosecond pump pulse is timed by an attosecond clock have not yet become available, but promise novel and complementary insights. These different realizations of attosecond chronoscopy have in common that they are capable of delivering real-time information on electronic processes on ultrafast time scales. Precisely which information is actually encoded and how it can be retrieved is, however, still a widely open question and understanding of the emergent chronoscopic information is still in its infancy. On the most fundamental level, it revolves around the lively debated issue of time and time delays as observables in quantum dynamics and the linear as well as nonlinear response of quantum systems to ultrafast perturbations. It, furthermore, is closely linked to the quantum-to-classical correspondence since timing, the notion of sequentiality of events and clocks, appears

to be an intrinsically classical concept. For large systems with many degrees of freedom (open quantum systems) classical time information is expected to emerge from time-dependent quantum dynamics via decoherence and dephasing (Zurek, 2003; Gardiner and Zoller, 2004; Weiss, 2012).

In view of an almost explosive growth of the literature in the field of attosecond physics in recent years ( $\sim 1500$  articles with the word “attosecond” in the title have been hitherto published which have been cited by another 8000 articles), we focus the discussion in this review article on the insights gained as well as on the many unresolved issues that have emerged for a few prototypical examples, most notably the first time-resolved realization of the photoelectric effect (Cavalieri *et al.*, 2007; Schultze *et al.*, 2010; Klünder *et al.*, 2011). Experiments on the photoelectric effect have provided a first glimpse of timing and time delay in photoemission. Time delay as a quantum dynamical observable was originally introduced by Eisenbud (1948) and Wigner (1955) for single-channel resonant scattering. Later, Smith (1960) generalized this approach to a multichannel context by the introduction of a lifetime matrix. This time delay is referred to as the Eisenbud-Wigner-Smith (EWS) delay. Photoemission representing a half-scattering process allows the application and extension of this concept. The corresponding delay  $t_{\text{EWS}}$  can be viewed as a finite time shift in the formation of the outgoing electronic wave packet during the photoemission event. Photoionization has been found to not be instantaneous as conventionally thought, but the departure of the outgoing wave packet is temporally shifted relative to the arrival of the XUV pulse, typically by a few attoseconds.

We review in the following the theoretical framework which unambiguously identifies  $t_{\text{EWS}}$  as an observable accessible by attosecond chronoscopy. The key is the determination of phase shifts in the presence of a probing IR field. We first discuss both one- and two-electron systems and address the influence of electronic correlation on the time-resolved photoemission processes. Extension to molecules reveals the influence of the internal geometric structure of the ionized complex on the formation of the outgoing wave packet. Photoemission from solid surfaces serves as a prime example for decoherence due to multiple scattering, connecting coherent quantum dynamics and classical transport. The recent extension to two-photon ionization reveals another novel observable: the time elapsed between two photoabsorption (photoemission) events. We also inquire into a possible scenario for probing the notion of tunneling time by attosecond streaking. We conclude by pointing to future directions. Unless otherwise stated, atomic units (a.u.) are used.

## II. TIME AND TIME DELAY AS OBSERVABLES IN PHOTOEMISSION

Attempts to observe electronic dynamics or, more generally, quantum dynamics in the time domain raise many interesting conceptual questions. Among them are the following: What can be learned from the time-dependent wave function of the electrons  $\Psi(t)$  or from the expectation value of an observable  $\langle O \rangle_t$  at a time  $t$  that cannot be inferred from the stationary (i.e., time-independent) final state observed at

$t \rightarrow \infty$  in a conventional spectroscopic measurement? On an even more fundamental level, is the time of a transition, or are time intervals  $\Delta t$  between elementary processes (or “quantum jumps”) physically meaningful observables? As highlighted in the following, time-resolved photoemission touches upon many of those aspects.

### A. S matrix and reduced density matrix for photoemission

Photoemission is described in first-order perturbation theory by the transition amplitude

$$a_{i \rightarrow f}^{(1)}(t) = -i \int_{-\infty}^t dt' \langle \Phi_f | e^{iH_0 t'} V(t') e^{-iH_0 t'} | \Phi_i \rangle, \quad (2.1)$$

where in the dipole approximation the interaction operator with the electromagnetic field of the ionizing XUV pulse is given in the so-called velocity gauge in terms of the vector potential  $\vec{A}$  by (Scully and Zubairy, 1997)

$$V(t) = \sum_{i=1}^N \vec{p}_i \cdot \vec{A}(t) / c \quad (2.2)$$

or alternatively in the length gauge (Göppert-Mayer, 1931) in terms of the electric field  $\vec{F}$  by

$$V(t) = \sum_{i=1}^N \vec{r}_i \cdot \vec{F}(t). \quad (2.3)$$

Physical observables should be independent of the choice of the gauge [Eqs. (2.2) and (2.3)]. This holds true if Eq. (2.1) is evaluated for exact initial and final states  $|\Phi_{i,f}\rangle$ . More generally, numerically exact solutions of the time-dependent Schrödinger equation yield gauge-independent transition probabilities  $|a_{i \rightarrow f}(t \rightarrow \infty)|^2$ . In contrast, in approximate treatments, notably within the framework of the strong-field approximation (SFA) for nonperturbative interactions of matter with strong IR fields, a strong dependence on the choice of the gauge has been observed (Bauer, Milošević, and Becker, 2005; Chirilă and Lein, 2006).

In Eq. (2.1) the initial bound state  $|\Phi_i\rangle$  and the final continuum state  $|\Phi_f\rangle$  are solutions of the stationary Schrödinger equation

$$H_0 |\Phi_{i,f}\rangle = E_{i,f} |\Phi_{i,f}\rangle \quad (2.4)$$

of the unperturbed system described by the Hamiltonian  $H_0$ . In the following examples  $H_0$  can represent atoms, molecules, or solid surfaces. The canonical position and momentum coordinates of the electrons are denoted by  $(\vec{r}_i, \vec{p}_i; i = 1, \dots, N)$ .

An attosecond pulse with carrier frequency  $\omega_{\text{XUV}}$  and duration  $\tau_{\text{XUV}}$  corresponding to a Fourier-limited pulse with spectral width  $\Delta\omega \sim 2\pi/\tau_{\text{XUV}}$  will generate a coherent superposition of final states  $|\Phi_f\rangle = |\Phi_{ejs}\rangle$ , i.e., a wave packet,

$$|\Psi(t)\rangle = \sum_{j,s} \int d\epsilon e^{-iE_{ejs}t} a_{ejs}(t) |\Phi_{ejs}\rangle, \quad (2.5)$$

where  $\epsilon$  characterizes the energy and  $j$  all other quantum numbers of the emitted electron [e.g., angular momentum  $\ell$ , spin quantum numbers  $S, M_S$ , and emission direction  $\hat{k} = (\theta, \varphi)$ ] while  $s$  stands for all quantum numbers of the  $N - 1$  electron state of the residual ionic complex  $I$ . For later reference we note that the asymptotic limit  $t \rightarrow \infty$  of Eq. (2.5) can be related to the scattering operator  $S$  (or  $S$  matrix) for the transition driven by the XUV field,

$$|\Psi_{t \rightarrow \infty}\rangle = S_{\text{XUV}} |\Phi_i\rangle. \quad (2.6)$$

The photoelectron spectrum corresponds to the expectation value of the projector  $P_{\epsilon j} = |\epsilon j\rangle \langle \epsilon j|$  onto continuum energy eigenstates of the emitted electron. After conclusion of the pulse at  $\tau_{\text{XUV}}$ , the Hamiltonian of the entire system eventually separates into channel Hamiltonians

$$H_0 = H_e + H_I^{(N-1)}, \quad (2.7)$$

with

$$H_e |\epsilon j\rangle = \epsilon_j |\epsilon j\rangle \quad (2.8)$$

the Schrödinger equation describing the emitted electron, and

$$H_I^{(N-1)} |s\rangle = E_s |s\rangle \quad (2.9)$$

the Schrödinger equation for the residual complex. The one-electron state  $|\epsilon j\rangle$  emerging from the interacting  $N$  electron system can be viewed as a Dyson orbital [see, e.g., Nicholson *et al.* (1999) and Ortiz (2003) and references therein]. The energy of the entire system is accordingly given by

$$E_{ejs} = \epsilon_j + E_s. \quad (2.10)$$

The expectation value,

$$\langle \Psi(t) | P_{\epsilon j} | \Psi(t) \rangle = \sum'_s |a_{ejs}(t)|^2, \quad (2.11)$$

represents the time-dependent photoionization probability, where the sum extends over the subset (denoted by the prime) of ionic states that are energetically accessible

$$|\epsilon + E_s - E_i - \omega_{\text{XUV}}| \lesssim \frac{\Delta\omega_{\text{XUV}}}{2} \quad (2.12)$$

within the spectral bandwidth [full width at half maximum (FWHM)]  $\Delta\omega_{\text{XUV}}$  of the pulse. Time-integral spectroscopy corresponds to a time average over time intervals  $\Delta t$  large compared to the pulse duration

$$\langle P_{\epsilon j} \rangle_{\Delta t} = \sum'_s \langle |a_{ejs}(t)|^2 \rangle_{\Delta t} \quad (2.13)$$

taken after the conclusion of the pulse. Equations (2.11) and (2.13) can be rewritten in terms of the asymptotic reduced one-electron density operator

$$\rho = \text{Tr}_I[|\Psi(t)\rangle\langle\Psi(t)|], \quad (2.14)$$

where the trace  $\text{Tr}_I$  extends over the Hilbert space of the ionic  $N - 1$  electron system. The time-integral photoemission probability Eq. (2.13) reads

$$\langle P_{\epsilon j} \rangle_{\Delta t} = \text{Tr}_e(|\epsilon j\rangle\langle\epsilon j|\rho), \quad (2.15)$$

where the trace  $\text{Tr}_e$  extends now over the unresolved degrees of freedom of the emitted electron (e.g., spin) and includes the time average over  $\Delta t$ . In angular-differential photoemission spectroscopy, the index  $j$  refers to the emission direction  $\hat{k}$ . Expansion of Eq. (2.15) in terms of partial-wave amplitudes  $\ell$  yields

$$\begin{aligned} \langle P_{\epsilon k} \rangle_{\Delta t} &= \sum_{\substack{\ell m \\ \ell' m'}} Y_{\ell}^m(\Omega) Y_{\ell'}^{m'*}(\Omega) \sum_s \langle a_{\ell m s}(t) a_{\ell' m' s}^*(t) \rangle_{\Delta t} \\ &= \sum_{\substack{\ell m \\ \ell' m'}} Y_{\ell}^m(\Omega) Y_{\ell'}^{m'*}(\Omega) \langle \epsilon \ell m | \rho | \epsilon \ell' m' \rangle_{\Delta t} \end{aligned} \quad (2.16)$$

with the solid angle  $\Omega = (\theta, \varphi)$ . Coherences between different partial waves ( $\ell, \ell'$ ) at the same energy  $\epsilon$  are expressed in terms of off-diagonal elements of the reduced density matrix  $\langle \epsilon \ell m | \rho | \epsilon \ell' m' \rangle$ . In turn, the angle-integrated spectrum depends only on the incoherent sum over partial waves

$$\begin{aligned} \langle P_{\epsilon} \rangle_{\Delta t} &= \int d\Omega \langle P_{\epsilon k} \rangle_{\Delta t} = \sum_{\ell m} \sum_s \langle |a_{\ell m s}(t)|^2 \rangle_{\Delta t} \\ &= \sum_{\ell m} \langle \epsilon \ell m | \rho | \epsilon \ell m \rangle_{\Delta t}. \end{aligned} \quad (2.17)$$

In general, energy-resolved photoemission spectra thus provide access only to the time-averaged square modulus of the transition amplitude [Eq. (2.17)]. In the special case of coherent excitation of degenerate subspaces to fixed energy  $\epsilon$ , relative phases between different partial-wave amplitudes  $\sim e^{i(\delta_{\ell} - \delta_{\ell'})}$  can be observed in angular resolved measurements [Eq. (2.16)].

In contrast, time-resolved measurements promise direct access to the time-dependent expectation value of dynamical observables  $O$  associated with the degrees of freedom of the emitted electron observed,

$$\begin{aligned} \langle \Psi(t) | O | \Psi(t) \rangle &= \int d\epsilon \int d\epsilon' \sum_{j, j'} \langle \epsilon j | O | \epsilon' j' \rangle \langle \epsilon' j' | \rho(t) | \epsilon j \rangle \\ &= \text{Tr}_e [O \rho(t)], \end{aligned} \quad (2.18)$$

expressed in terms of the time-dependent reduced density matrix (without averaging over  $\Delta t$ )

$$\langle \epsilon j | \rho(t) | \epsilon' j' \rangle = \sum_s a_{\epsilon j s}(t) a_{\epsilon' j' s}^*(t) e^{i(\epsilon' - \epsilon)t}. \quad (2.19)$$

Coherences between continuum states of different energies  $\epsilon$  present in the wave packet are now in reach and manifest themselves by “quantum beats” with frequencies  $|\epsilon' - \epsilon|$  (Yudin *et al.*, 2005; Hu and Collins, 2006; Yudin, Bandrauk, and Corkum, 2006; Morishita, Watanabe, and

Lin, 2007; Kazansky, Kabachnik, and Sazhina, 2008; Argenti and Lindroth, 2010; Mauritsson *et al.*, 2010; Feist *et al.*, 2011; Pabst *et al.*, 2011; Tzallas *et al.*, 2011; Bian and Bandrauk, 2012; Argenti *et al.*, 2013; Klünder *et al.*, 2013; Wirth, Santra, and Goulielmakis, 2013; Carpeggiani *et al.*, 2014; Chini *et al.*, 2014; Ott *et al.*, 2014). Comparison between Eqs. (2.16) and (2.18) indicates that the interrogation of the photoemission process at any time  $t$  promises to uncover dynamical information not accessible in time-integral measurements. A proposal for such a direct measurement of the time-resolved ionization probability near autoionizing resonances in helium employing attosecond pulses has recently been discussed (Argenti *et al.*, 2013).

In current realizations of attosecond chronoscopy, the operator facilitating the *in situ* interrogation during the photoemission is another pulse described by the interaction operator  $V$  [Eqs. (2.2) and (2.3)] displaced in time relative to the ionizing attosecond pulse by a variable delay time  $\tau$ . Ideally, the probing pulse would be another attosecond XUV pulse of comparable duration. While considerable progress has been made toward developing attosecond XUV sources of sufficient intensity and timing control (Chang and Corkum, 2010; Gilbertson, Wu *et al.*, 2010; Takahashi *et al.*, 2010; Lan, Takahashi, and Midorikawa, 2011; Tzallas *et al.*, 2011), such XUV-pump–XUV-probe settings have not yet been implemented for attosecond chronoscopy. Instead, IR laser pulses for which exquisite phase and thus subcycle timing control has been achieved [see, e.g., Hentschel *et al.* (2001), Baltuska *et al.* (2003), and Chang (2011) and references therein] are used to interrogate the time evolution. While the pulse duration of a typical few-cycle pulse is  $\tau_{\text{IR}} \approx 5$  fs (the period  $T_{\text{IR}}$  of an optical cycle for 800 nm radiation is  $T_{\text{IR}} = 2.7$  fs), its oscillating field, controlled to within a small fraction of 1 rad, offers a convenient route to attosecond time resolution. The three different approaches utilized so far, linear momentum attosecond streaking with linearly polarized IR fields (Drescher *et al.*, 2001; Hentschel *et al.*, 2001; Kienberger *et al.*, 2004; Sansone *et al.*, 2006; Cavalieri *et al.*, 2007; Schultze *et al.*, 2010; Sabbar *et al.*, 2015), angular streaking (attoclock) (Eckle, Pfeiffer *et al.*, 2008; Eckle, Smolarski *et al.*, 2008; Pfeiffer *et al.*, 2011, 2013; Pfeiffer, Cirelli *et al.*, 2011) with circularly polarized IR fields, and the interferometric RABBIT technique (Paul *et al.*, 2001; Toma and Muller, 2002; Mauritsson, Gaarde, and Schafer, 2005; Swoboda *et al.*, 2010; Klünder *et al.*, 2011; Guénot *et al.*, 2012, 2014; Palatchi *et al.*, 2014), have in common that the IR field probes the evolution during the emission, as implied by Eq. (2.18), without, however, necessarily performing a projective measurement which would lead to the “collapse of the wave packet,” i.e., to the reduction of the density operator. Instead, the probe pulse maps the time-dependent excited state  $|\Psi(t)\rangle$  onto the asymptotic scattering state  $|\Phi\rangle$ , such that chronoscopic information can eventually be retrieved from spectral information [Eqs. (2.16) and (2.17)]. The key point is that the timing information sought can be extracted from the asymptotic  $S$ -matrix element [analogous to Eq. (2.6)],

$$|\Psi(t \rightarrow \infty)\rangle = S_{\text{XUV+IR}} |\Phi_i\rangle, \quad (2.20)$$

that includes the influence of both the exciting XUV-pump field and the probing IR field. Details of this mapping differ for the different approaches and are far from fully understood. We will analyze this mapping in detail for the example of attosecond streaking which operates, in certain limiting cases, like a classical clock.

## B. Time-delay operator

Unambiguously recovering timing information from the asymptotic time-independent scattering state Eq. (2.20) touches upon the lively debated question whether and to which extent time or time delay are well-defined quantum observables at all. It was realized in the early days of quantum theory by Pauli (1926, 1933) that association of time  $t$  with a Hilbert operator following standard correspondence identities,

$$\hat{t} = -i \frac{\partial}{\partial E}, \quad (2.21)$$

faces fundamental conceptual difficulties. Since the spectrum of the canonically conjugate operator  $H$  of a quantum system is bounded from below,  $\hat{t}$  cannot be a self-adjoint operator. This argument originally developed in the context of the nonrelativistic Schrödinger equation can be extended into the relativistic domain. Even though the Dirac equation allows for unbounded negative-energy solutions, the finite excitation gap  $[-mc^2, mc^2]$  delimits the continuous spectrum of  $H$  and thus prevents the construction of a self-adjoint operator  $\hat{t}$  (Maquet, Caillat, and Taïeb, 2014; Maquet, 2014). This conceptual difficulty is directly related to the well-recognized fact that the quantum-theoretical foundation of the time-energy uncertainty relation  $\Delta t \Delta E \gtrsim \hbar/2$  is fundamentally different from the uncertainty relation for canonically conjugate variables of generalized positions and momenta  $\Delta x_i \Delta p_i \geq \hbar/2$ . While both relations express the Fourier reciprocity, a self-adjoint operator  $\hat{t}$ , unlike the position operator, does not exist. Therefore, many standard quantum theory textbooks state that  $t$  is a parameter with which no operator is associated (Gottfried, 1966; Cohen-Tannoudji, Diu, and Laloë, 1977). Recent work in mathematical physics clarified the formal properties of time as a Hilbert space operator. The “arrival time” operator [Eq. (2.21)] can be shown to be symmetric rather than self-adjoint. For a recent introduction into the formal aspects of the time operator in quantum physics, see Sassoli de Bianchi (2012).

A different scenario emerges, however, when the domain of the operator is restricted to scattering states. This allows one to construct a self-adjoint operator describing the *time delay*. Based on intuitive physical reasoning, Eisenbud (1948), Wigner (1955), and Smith (1960) argued already in the 1950s that time delays or lifetimes of resonances should be expectation values of a bona-fide observable in quantum scattering, the time-delay operator,

$$\hat{t}_{\text{EWS}} = -i S^\dagger(E) \frac{\partial}{\partial E} S(E), \quad (2.22)$$

where  $S(E)$  is the scattering operator (matrix). Note that the time-delay operator Eq. (2.22) bears no direct relationship to

the arrival time operator [Eq. (2.21)] and to the time-energy uncertainty relation.

A prototypical case is resonant scattering where  $t_{\text{EWS}}$  describes the “sticking time” of the incoming particle due to transient trapping in a quasibound state before leaving the interaction region as an outgoing wave packet. This sticking time amounts to the time delay of the outgoing wave packet relative to that of the incoming wave packet passing by the scattering region in the absence of the interaction potential. Formally, the subtraction of the travel time of the unperturbed wave packet is built into Eq. (2.22) by restricting the application of the differential operator to the energy dependence of the  $S$  matrix only and not to the unperturbed continuum state the  $S$  operator acts on. In a multichannel scattering problem with  $M$  open channels ( $i = 1, \dots, M$ ), the time-delay operator becomes an  $M \times M$  matrix (Smith, 1960),  $\langle \Phi_i | \hat{t}_{\text{EWS}} | \Phi'_i \rangle$ . The eigenstates of the self-adjoint  $\hat{t}_{\text{EWS}}$  matrix describe the scattering eigenchannels. Their eigenvalues correspond to the proper time delays associated with the corresponding scattering channel (Libisch *et al.*, 2008; Rotter, Ambichl, and Libisch, 2011).

The EWS time-delay operator Eq. (2.22) is well defined only for  $S$  matrices describing scattering at short-ranged potentials. In the special case of potential scattering with spherical symmetry, the  $S$  matrix is diagonal in the angular momentum representation  $S_\ell$ ,

$$S_\ell(E) = e^{2i\delta_\ell(E)}. \quad (2.23)$$

The corresponding time delay for a given partial wave  $\ell$  follows from Eqs. (2.22) and (2.23) as the energy variation of the partial-wave scattering phase shift  $\delta_\ell(E)$ ,

$$t_{\text{EWS}}(E, \ell) = 2 \frac{d}{dE} \delta_\ell(E). \quad (2.24)$$

The outgoing wave packet is assumed to reach within a finite propagation time the asymptotic interaction-free region where the channel Hamiltonian  $H_\ell$  [Eq. (2.8)] consists of the kinetic energy operator only. Extension of the time-delay operator to Coulomb scattering requires modifications (Martin, 1981; Bollé, Gesztesy, and Grosse, 1983).

The concept of time delays has found application in many branches of physics, classical as well as quantum, that deal with wave propagation and scattering, ranging from the Goos-Hänchen effect in electromagnetic scattering at dielectric interfaces (Goos and Hänchen, 1947; Chiu and Quinn, 1972) and resonant photon scattering at ultracold atoms (Bourgain *et al.*, 2013) to electron transport through mesoscopic devices (“billiards”) featuring hybrid normal-conducting and superconducting boundaries (Libisch *et al.*, 2008). Closely related to time delay is the concept of dwell time or sojourn time, the time a wave packet remains localized within a finite domain in coordinate space. The relationship between dwell time and time delay as well as applications are discussed in recent reviews (de Carvalho and Nussenzweig, 2002; Kolomeitsev and Voskresensky, 2013). The connections to the controversial subject of “tunneling time,” the time it takes a wave packet to penetrate a barrier, have been the subject of a large number of publications (MacColl, 1932;

Hartman, 1962; Hauge and Støvneng, 1989; Landauer and Martin, 1994; Steinberg, 1995; Olkhovsky, Recami, and Jakiel, 2004; Winful, 2006; Kolomeitsev and Voskresensky, 2013). Attempts to observe tunneling times on the attosecond scale for strong-field ionization of atoms (Eckle, Smolarski *et al.*, 2008; Shafir *et al.*, 2012; Klaiber *et al.*, 2013; McDonald *et al.*, 2013; Pfeiffer *et al.*, 2013; Zhao and Lein, 2013; Orlando *et al.*, 2014) have so far been inconclusive. While outside the main scope of this article on the time-resolved photoelectric effect, we briefly discuss the challenge in extracting such timing information in Sec. IX.

Employing the delay operator [Eqs. (2.22)–(2.24)] to attosecond chronoscopy of photoemission described by first-order perturbation theory (or lowest-order perturbation theory for the case of two-photon double ionization discussed in Sec. VIII) requires several modifications. First, photoemission is a half-scattering process in which a matter wave packet resides in the continuum only in the exit channel while in the entrance channel the wave function  $|\Phi_i\rangle$  represents a bound rather than a continuum state. Second, photoemission leaves a residual charged ionic fragment behind. Consequently, the outgoing electron is subject to the long-range Coulomb interaction for which the intrinsic EWS time delay is, strictly speaking, not well defined (Wigner, 1955; Smith, 1960; Martin, 1981; Bollé, Gesztesy, and Grosse, 1983). We show in the following that, with suitable modifications,  $t_{\text{EWS}}$  can, indeed, be unambiguously determined for Coulombic exit-channel interactions. Third, the time information contained in the scattering operator describing the ionization by the XUV field alone,  $S_{\text{XUV}}$ , has to be disentangled from that describing the simultaneous presence of the probing field,  $S_{\text{XUV-IR}}$ .

For emission of an electron from a one-electron system with energy  $\epsilon$  and in the direction  $\hat{k}$ , the  $S_{\text{XUV}}$  matrix element describing the transition driven by the XUV field in the absence of the probing field follows from Eqs. (2.1) and (2.3) (with  $t \rightarrow \infty$ ) as

$$\langle \epsilon \hat{k} | S_{\text{XUV}} | \Phi_i \rangle = -i \tilde{F}_{\text{XUV}}(\omega = \epsilon - E_i) \langle \epsilon \hat{k} | \hat{r} \hat{e} | \Phi_i \rangle, \quad (2.25)$$

where  $\tilde{F}_{\text{XUV}}(\omega)$  is the Fourier transform of the electric field of the attosecond pulse and  $\hat{e}$  is its polarization vector (in the following we set  $\hat{e} = \hat{z}$ ). Application of Eqs. (2.22) and (2.25) yields the expectation value of the EWS time delay

$$t_{\text{EWS}}(\epsilon, \hat{k}) = \frac{d}{d\epsilon} \arg \langle \epsilon \hat{k} | z | \Phi_i \rangle. \quad (2.26)$$

We assume in the following that the temporal structure of the XUV pulse is Fourier transform limited and chirp free, i.e., its frequency distribution remains constant during the duration of the pulse. Otherwise, pulse-induced contributions to the spectral variation of the photoionization amplitude would give rise to apparent spectral variations similar to Eq. (2.26) masking the EWS delay (Cirelli *et al.*, 2015). Controlling and minimizing the chirp is therefore essential in extracting accurate time delays (Schultze *et al.*, 2010).

In the special case where only a single partial wave in the continuum is accessed in a dipole transition, e.g., in an  $S \rightarrow P$  transition, Eq. (2.26) reduces to

$$t_{\text{EWS}}(\epsilon, \ell) = \frac{d}{d\epsilon} \delta_\ell(\epsilon). \quad (2.27)$$

The missing factor of 2 [compared to Eq. (2.24)] indicates that photoemission is a half-scattering process. Generalization of Eq. (2.22) to a one-electron emission from a many-electron system employing Eq. (2.13) reads

$$\begin{aligned} \langle t_{\text{EWS}}(\epsilon, \hat{k}) \rangle &= \text{Tr}_I \langle \Phi_i | S_{\text{XUV}}^\dagger \left( -i \frac{\partial}{\partial \epsilon} \right) S_{\text{XUV}} | \Phi_i \rangle \\ &= -i \sum'_s \langle \Phi_i | S_{\text{XUV}}^\dagger | \epsilon \hat{k} s \rangle \frac{\partial}{\partial \epsilon} \langle \epsilon \hat{k} s | S_{\text{XUV}} | \Phi_i \rangle \\ &\simeq \frac{\sum'_s \frac{\partial}{\partial \epsilon} \arg \langle \epsilon \hat{k} s | z | \Phi_i \rangle |\langle \epsilon \hat{k} s | z | \Phi_i \rangle|^2}{\sum'_s |\langle \epsilon \hat{k} s | z | \Phi_i \rangle|^2}, \end{aligned} \quad (2.28)$$

where the energy dependence of the modulus of the dipole matrix element has been neglected in the last step.

The time delay extracted from  $S_{\text{XUV}}$ , calculated by first-order perturbation theory, characterizes the linear response of the unperturbed system  $H_0$  and is, thus, independent of the properties of the XUV pulse. It is therefore tempting to inquire into alternative routes to access such time-delay information without performing attosecond time-resolved measurements. Since the time delay is determined by the spectral variation of the partial-wave scattering phase, the energy variation of the scattering probability or cross section for electron scattering [ $\sigma(\epsilon) \sim \langle P_\epsilon \rangle$ , see Eq. (2.17)]

$$\begin{aligned} \frac{d}{d\epsilon} \sigma(\epsilon) &= \frac{d}{d\epsilon} \left( \frac{2\pi}{c} \sum_\ell (2\ell + 1) \sin^2 \delta_\ell(\epsilon) \right) \\ &= \frac{4\pi}{c} \sum_\ell (2\ell + 1) \sin \delta_\ell(\epsilon) \cos \delta_\ell(\epsilon) t_{\text{EWS}}(\epsilon, \ell) - \frac{\sigma(\epsilon)}{\epsilon} \end{aligned} \quad (2.29)$$

depends only on the scattering phases  $\delta_\ell(\epsilon)$  and on  $t_{\text{EWS}}(\epsilon, \ell)$ . Therefore, in principle, the determination of the time delay through time-integral cross-section measurements is possible provided that the energy dependence of individual partial-wave phase shifts can be accurately determined by angular-differential scattering [along the lines of Eq. (2.16)]. In practice, however, the determination of  $t_{\text{EWS}}$  from Eq. (2.29) is a considerable challenge, as the number of partial waves contributing to electron-ion scattering is, in general, large and therefore the extraction of  $t_{\text{EWS}}$  from Eq. (2.29) is hardly feasible. Moreover, averaging over unobserved degrees of freedom [see, for example, Eqs. (2.16) and (2.28)] may invalidate such a direct approach. In special cases, however, partial information on time delay can be inferred and a connection to attosecond chronoscopy established. Heinzmann *et al.* pointed out [for recent reviews, see Heinzmann and Dil (2012) and Heinzmann (2013)] that the dynamical spin polarization  $P_\perp$  perpendicular to the scattering plane defined by an incoming circularly polarized photon and an outgoing electron is a function of the difference between partial waves accessible by photoionization. Emission of spin-polarized photoelectrons originally predicted by Fano (1969) for circularly polarized light

(the so-called Fano effect) was later generalized by Cherepkov (1979) to the case of linearly polarized light in angular resolved photoemission. Ionizing the  $5p$  shell of xenon, a net spin polarization  $P_{\perp}(\theta = 54^{\circ}, \epsilon) \propto \sin[\delta_2(\epsilon) - \delta_0(\epsilon)]$  is observed at the “magic” angle  $\theta = 54.4^{\circ}$  [the zero of the Legendre polynomial  $P_2(\cos\theta)$ ]. Carefully observing the energy variation of the spin polarization

$$\frac{d}{d\epsilon} P_{\perp}(\theta = 54^{\circ}, \epsilon) \propto \cos[\delta_2(\epsilon) - \delta_0(\epsilon)][t_{\text{EWS}}^{\ell=2}(\epsilon) - t_{\text{EWS}}^{\ell=0}(\epsilon)] \quad (2.30)$$

allows one to extract a relative time delay of  $\approx 76$  as between the  $d$  and  $s$  electrons near  $\epsilon = 7$  eV (Heinzmann, 2013). In the present case this experimental observation implies that formation of the outgoing wave packet in the  $d$  partial wave is considerably delayed relative to that in the  $s$  wave. For later reference we note that this value is strongly influenced by the long-range Coulomb interaction.

While for scattering at a potential the reference wave packet corresponds to the incoming wave packet that travels through the scattering region unaffected by any interaction potential, in the half-scattering case of photoemission the reference is the arrival  $t_a$  of the peak of the XUV pulse at the target, for which we frequently use a Gaussian shape

$$F_{\text{XUV}}(t) = F_0 \exp\left(-\frac{(t-t_a)^2}{t_g^2}\right) \cos(\omega_{\text{XUV}}t + \varphi_{\text{XUV}}) \quad (2.31)$$

with  $t_g = \tau_{\text{XUV}}/\sqrt{\ln 4}$ . The time delay  $t_{\text{EWS}}$  is measured relative to  $t_a$  and can be positive or negative. We use in the following the terms “time delay” and “time shift” interchangeably to express the fact that  $t_{\text{EWS}}$  can be both positive and negative. Negative values are constrained by causality (Wigner, 1955), i.e., photoemission cannot occur prior to the arrival of the leading edge of the ionizing pulse.

One key feature of  $t_{\text{EWS}}$ , which we frequently make use of in the following, is that it can be directly extracted from the motion of the outgoing wave packet without any explicit reference to the  $S$  matrix or the spectral variation of scattering phase shifts (de Carvalho and Nussenzeig, 2002). For the outgoing wave packet formed by a coherent superposition of energy eigenstates of the electron centered around a central energy  $\epsilon_0$ , the radial position of its crest  $r_c(t)$  or its first moment  $\langle r \rangle_t$  eventually follows asymptotically ( $t \rightarrow \infty$ ) the motion of a free particle after the wave packet has left the scattering region,

$$r_c(t) = v_g(t - t_{\text{EWS}}), \quad (2.32)$$

$$\langle r \rangle_t = v_g(t - t_{\text{EWS}}), \quad (2.33)$$

however delayed by the time  $t_{\text{EWS}}$  (Brenig and Haag, 1959). In Eqs. (2.32) and (2.33) the group velocity  $v_g$  is denoted by

$$v_g = \left(\frac{\partial \epsilon}{\partial k}\right)_{\epsilon=\epsilon_0}. \quad (2.34)$$

A prerequisite for Eqs. (2.32) and (2.33) is that the interaction potential is short ranged such that the wave packet behaves like that of a free particle at large distances. The extension to

Coulomb interactions is discussed in Sec. III. The equivalence of the time delay extracted from the displacement of  $\langle r \rangle_t$  to the one extracted from the  $S$  matrix plays a key role for photoemission from complex systems where the dynamics is, in general, no longer fully coherent due to averaging over unresolved degrees of freedom [see Eq. (2.28)]. As decoherence eventually converts the quantum wave packet into a classical probability distribution of emitted electrons, a delay of the first moment  $\langle r \rangle_t$  of this distribution relative to the reference pulse can still provide timing information. Equation (2.33) is therefore well suited to explore the quantum-to-classical correspondence and for application to condensed matter where photoelectrons may undergo multiple dephasing collisions prior to exiting the solid surface (see Sec. VII).

### C. Photoionization from a model atom

We illustrate the temporal evolution of photoionization and the time delay in photoemission relative to an attosecond XUV pulse for a one-electron model atom that is designed to resemble the ion  $\text{He}^+(1s)$  at small distances which has identical binding energy  $E_i = \epsilon_{1s}$  but features only short-ranged interactions, thereby avoiding the complications caused by the Coulomb field. Such a model could, for example, mimic photodetachment from negative ions. For simplicity we use the term ionization also for this process. Figure 1 illustrates the photoionization by an attosecond XUV pulse (pulse duration  $\tau_{\text{XUV}} = 200$  as, energy  $\omega = 80$  eV, intensity  $I_{\text{XUV}} = 10^{13}$  W/cm<sup>2</sup>) of an electron initially bound in an  $s$ -like ground state of the Hamiltonian

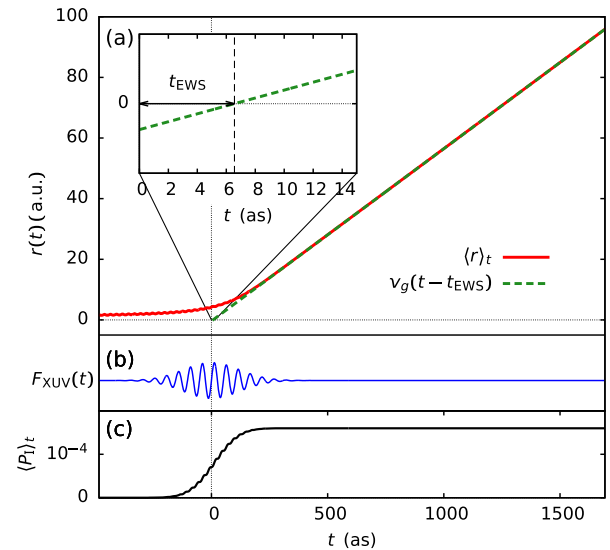


FIG. 1 (color online). Photoionization of an initial  $1s$  electron in a Yukawa potential [Eq. (2.36)] with  $Z = 3.8166$  and  $a = 0.5$ , which results in a binding energy of  $-2$  a.u.: (a) Extraction of  $t_{\text{EWS}}$  from the linear extrapolation of the time dependence of  $\langle r \rangle_t$  [Eq. (2.33)]. The intercept with the  $t$  axis (inset) gives  $t_{\text{EWS}}$  in excellent agreement with the direct calculation from the  $S$  matrix [Eq. (2.27)]. (b) The temporal profile of the XUV pulse. (c) The time dependence of the ionization probability  $\langle \psi(t) | P_1 | \psi(t) \rangle$  [from Eqs. (2.18) and (2.37)].

$$H_0 = H_e = \frac{p^2}{2} + V_Y(r) \quad (2.35)$$

with a Yukawa-type interaction potential

$$V_Y(r) = -\frac{Z}{r} \exp\left(-\frac{r}{a}\right), \quad (2.36)$$

and the screening length  $a$ . For later comparison with photoionization of  $\text{He}^+$  we choose the charge parameter  $Z$  for given screening length  $a$  such that the binding energy of the ionized electron always coincides with that of the  $\text{He}^+(1s)$  ion ( $E_i = -2$  a.u.). Here and in the following, the peak of the XUV-pulse envelope is chosen to arrive at  $t_a = 0$ , defining the reference time for the time delay. The radial expectation value of the wave packet  $\langle r \rangle$  [Fig. 1(a)] is at  $t = 0$  already considerably larger compared to the ground-state expectation value  $\langle r \rangle_{t \rightarrow -\infty} = 0.25$  reflecting the onset of emission for  $t < 0$  initiated by the leading edge of the pulse [Fig. 1(b)].

For positive  $t$  the radial expectation value rapidly approaches the linear distance versus time relation [Eq. (2.33)] after the conclusion of the XUV pulse (FWHM) at  $t \approx 4$  a.u. ( $\sim 100$  as). Tracing back the linear time dependence of  $\langle r \rangle_t$  to small times allows one to determine  $t_{\text{EWS}}$  from the intercept with the  $t$  axis [Fig. 1(a), inset] as  $t_{\text{EWS}} = 6.6$  as. Note that the backward extrapolation to  $\langle r \rangle = 0$  underlying the determination of  $t_{\text{EWS}}$  according to Eqs. (2.32) and (2.33) serves to extract information on the asymptotic rather than the local properties of the outgoing wave packet. The idea underlying the backward extrapolation can be most easily visualized by considering classical trajectories along one Cartesian coordinate. An outgoing electron along, e.g., the positive  $x$  axis, starts, *on average*, from  $x = 0$  since an initial state of well-defined parity has equal probability being at  $\pm x_{\text{initial}}$ . For a radially symmetric initial state this holds true for every direction. The value extracted by Eq. (2.33) agrees with the one extracted from the  $p$  wave ( $\ell = 1$ ) phase shift  $\delta_{\ell=1}$  at  $E = \omega + \epsilon_i$  [Eq. (2.27)] to within 0.1 as, illustrating the equivalence of Eqs. (2.27) and (2.33) for photodetachment with subattosecond precision (Pazourek, Nagele, and Burgdörfer, 2013; Su *et al.*, 2013b; Nagele *et al.*, 2014).

Alternatively, the timing of the photoionization process can also be monitored by inspecting the time-dependent norm of the ionized portion of the electronic wave packet in the continuum (Kheifets and Ivanov, 2010; Sukiasyan, Ishikawa, and Ivanov, 2012) given by the expectation value [Eq. (2.18)]  $\langle P_I \rangle_t = \langle \Psi(t) | P_I | \Psi(t) \rangle$  with

$$P_I = 1 - \sum_i^{(\text{bound})} |i\rangle \langle i|. \quad (2.37)$$

Even though the expectation value  $\langle P_I \rangle_t$  determined from the numerical solution of the time-dependent Schrödinger equation (TDSE) solution [Fig. 1(c)] appears to be shifted with respect to the ionizing XUV pulse, its functional form strictly follows the prediction by first-order perturbation theory Eq. (2.1). In this sense the response of the electronic

wave function to the ionizing field is instantaneous. Consequently,  $\langle P_I \rangle_t$  depends on the temporal shape of the XUV field and the absolute magnitude of the dipole matrix element but not on its phase. While  $\langle P_I \rangle_t$  can be easily extracted from simulations, it does not, however, correspond to an experimental observable as it is not accessible through the asymptotic final state. This is underscored by the fact that the value of  $\langle P_I \rangle_t$  is not unique but depends on the choice of the projection  $\{|i\rangle \langle i|\}$  in Eq. (2.37). The field-free bound states  $\{|i\rangle\}$  chosen in the present example [Fig. 1(c)] are of no specific physical significance in the presence of the XUV field  $F_{\text{XUV}}(t)$ . An alternative choice would be the projection onto the adiabatic bound-state spectrum  $\{|i\rangle_{F_{\text{XUV}}(t)}\}$ . Moreover,  $\langle P_I \rangle_t$  can be shown to be strongly dependent on the choice of the gauge [Eqs. (2.2) and (2.3)] even within an exact solution of the TDSE contradicting the notion of a physical observable. Both the overall shape of the turn-on curve of  $\langle P_I \rangle_t$  and the amplitude and phase of the superimposed small oscillations [Fig. 1(c)] vary with gauge. Only after the conclusion of the pulse does the bound-state projection become unique which is, however, well past the ionization times to be extracted. It is, therefore, difficult to identify a meaningful ionization time from calculated  $\langle P_I \rangle_t$  since it carries no direct information on the scattering phases.

The example of the model atom with short-ranged interactions [Eqs. (2.35) and (2.36)] illustrates that the group delay  $t_{\text{EWS}}$ , i.e., the delayed formation of an outgoing wave packet propagating with group velocity  $v_g$  toward the detector, provides temporal information encoded in the asymptotic wave packet but is unrelated to the time-dependent norm of the continuum portion of the wave function.

### III. COULOMB SCATTERING AND COULOMB TIME DELAY

Since in photoionization the exit-channel interaction between the outgoing electron and the residual complex is Coulombic, suitable generalizations of the time-delay operator [Eq. (2.26)] are required to account for the infinite range of the potential. The receding wave packet remains asymptotically Coulomb distorted and never converges to a free wave packet. Since this Coulomb distortion is universal, i.e., independent of any system-specific short-ranged interactions, a general formulation of the modification can be given (Martin, 1981). A convenient starting point is the asymptotic expansion of the Coulomb wave  $\Phi_{\vec{k}}^{\text{C}}(Z, \vec{r})$  in the field of the ionic charge  $Z$  with wave vector  $\vec{k}$  and energy  $\epsilon = k^2/2$ ,

$$\Phi_{\vec{k}}^{\text{C}}(Z, \vec{r}) = \sum_{\ell} (2\ell + 1) i^{\ell} e^{i\sigma_{\ell}^{\text{C}}(\epsilon)} F_{\ell}(Z, k, r) kr P_{\ell}(\cos \theta). \quad (3.1)$$

The asymptotic limit  $r \rightarrow \infty$  of the amplitude of the partial wave  $\ell$  is given by

$$F_\ell(Z, k, r) \xrightarrow{r \rightarrow \infty} \sin\left(kr - \frac{\ell\pi}{2} + \frac{Z}{k} \ln 2kr + \sigma_\ell^C(\epsilon)\right) \quad (3.2)$$

with the  $r$ -independent Coulomb phase shift

$$\begin{aligned} \sigma_\ell^C(\epsilon) &= \arg \Gamma\left(1 + \ell - i\frac{Z}{k}\right) \\ &= \text{Im}\left[\ln \Gamma\left(1 + \ell - i\frac{Z}{k}\right)\right]. \end{aligned} \quad (3.3)$$

$\sigma_\ell^C(\epsilon)$  can be taken as the Coulomb analog of the short-ranged phase shift  $\delta_\ell(\epsilon)$ . Correspondingly, the on-shell Coulomb partial-wave  $S$  matrix is given by

$$S_\ell^C(\epsilon) = \frac{\Gamma(1 + \ell - iZ/k)}{\Gamma(1 + \ell + iZ/k)}. \quad (3.4)$$

In analogy to Eq. (2.27), we define a Coulomb time delay for half scattering (Martin, 1981) through

$$t_{\text{EWS}}^C(\epsilon, \ell) = \frac{d}{d\epsilon} \sigma_\ell^C(\epsilon). \quad (3.5)$$

We refer to this  $r$ -independent delay in the following as the Coulomb-EWS delay. However, the long-range Coulomb distortion gives rise to the additional  $r$ -dependent logarithmic phase ( $\sim \ln 2kr$ ) in Eq. (3.2) relative to which the Coulomb phase shift is now defined. Since both phase contributions depend on the same Sommerfeld parameter  $\eta = Z/k$ , a clear-cut separation and interpretation is not straightforward. As first pointed out by Clark (1979) in a little known paper it is convenient to include both phase contributions into the definition of the Coulomb time delay

$$t_{\text{Coul}}(\epsilon, \ell, r) = \frac{\partial}{\partial \epsilon} \left( \frac{Z}{k} \ln(2kr) + \sigma_\ell^C(\epsilon) \right) \quad (3.6)$$

$$= \Delta t_{\text{Coul}}(\epsilon, r) + t_{\text{EWS}}^C(\epsilon, \ell) \quad (3.7)$$

containing, in addition to  $t_{\text{EWS}}^C$ , a contribution due to the logarithmic distortion of the wave front

$$\Delta t_{\text{Coul}}(\epsilon, r) = \frac{Z}{(2\epsilon)^{3/2}} [1 - \ln(2\sqrt{2\epsilon}r)]. \quad (3.8)$$

We refer to  $\Delta t_{\text{Coul}}$  [Eq. (3.8)] as the Coulomb correction to the EWS time delay  $t_{\text{EWS}}^C$  [Eq. (3.5)]. The Coulomb time shift  $t_{\text{Coul}}$  [Eq. (3.7)] has only recently been investigated (Zhang and Thumm, 2010, 2011c; Ivanov and Smirnova, 2011; Nagele *et al.*, 2011; Dahlström, L'Huillier, and Maquet, 2012; Dahlström *et al.*, 2013; Pazourek, Nagele, and Burgdörfer, 2013; Serov, Derbov, and Sergeeva, 2013; Su *et al.*, 2013b, 2013c) in the context of attosecond time-resolved photoemission. It gives the time delay relative to a free wave packet, however, with the drawback that its value depends on the radial coordinate and diverges as  $r \rightarrow \infty$ .

The significance of  $t_{\text{Coul}}$  can be illustrated with the help of a simulation for the photoionization of  $\text{He}^+(1s)$  performing the same calculation as for short-ranged potentials (see Sec. II.C)

with identical pulse parameters, however, for diverging screening lengths  $a \rightarrow \infty$  [Eq. (2.36)], i.e.,  $V_Y \rightarrow V_C$  in Eq. (2.35). The time evolution of the first moment of the outgoing wave packet [Fig. 2(a)] appears to closely resemble that in a short-ranged potential for short times [Fig. 1(a)]. For large times, the growth of  $\langle r \rangle_t$  slows down with  $t$  and bends toward the  $t$  axis [schematically shown in Fig. 2(a), inset]. The intercept with the  $t$  axis from the linear extrapolation [Eq. (2.33)]  $t - \langle r \rangle_t/k$  does not converge to a well-defined limit but becomes dependent on the time when the temporal extrapolation is performed. This intercept follows, however, with remarkable accuracy [Fig. 2(c)], the implicit relation

$$t_{\text{Coul}}(\epsilon, \ell, \langle r \rangle_t) = t - \frac{\langle r \rangle_t}{k}, \quad (3.9)$$

which can be further simplified to the explicit relation

$$t - \frac{\langle r \rangle_t}{k} = t_{\text{EWS}}^C(\epsilon, \ell) + \frac{Z}{(2\epsilon)^{3/2}} [1 - \ln(2k^2t)], \quad (3.10)$$

where the locally varying delay time  $\Delta t_{\text{Coul}}$  [Eq. (3.8)] is evaluated at  $r = kt$  for the radial motion of a free particle. The error introduced by the latter approximation is within the graphical accuracy of Fig. 2(c). The Coulomb delay time  $t_{\text{Coul}}$  [Eq. (3.7)] is therefore the analog to the time shift associated with the first moment of the wave packet [Eq. (2.33)] while the Coulomb-EWS time  $t_{\text{EWS}}^C$  is the analog to the time delay determined by the spectral variation of the phase shift

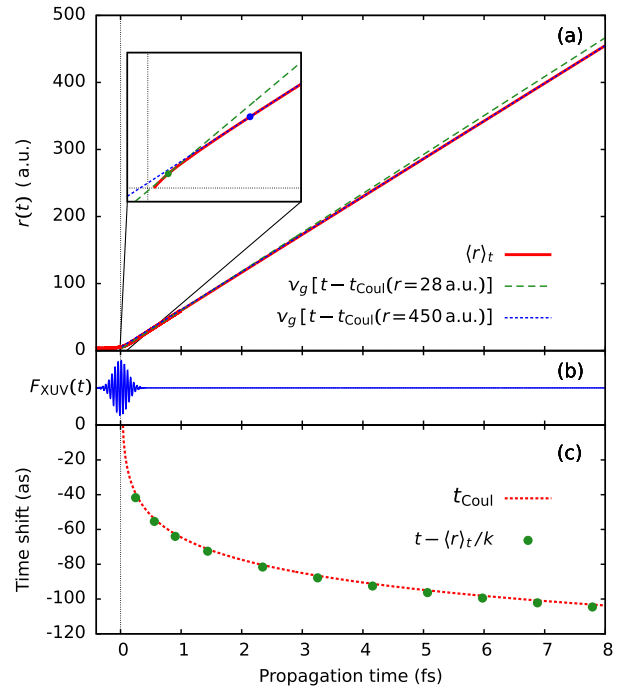


FIG. 2 (color online). As in Fig. 1 but for  $\text{He}^+(1s)$  with Coulomb interaction. (a)  $\langle r \rangle_t$  vs time, the inset schematically indicates the change in the intercept depending on the distance (or propagation time) at which the linear slope is determined [Eq. (3.9)] due to the sublinear growth of  $\langle r \rangle_t$ . (b) Temporal profile of the XUV pulse. (c) Comparison between the intercept determined from (a) and the analytic prediction of  $t_{\text{Coul}}$  [Eq. (3.7)].

[Eq. (2.27)]. Unlike for short-ranged potentials, these two quantities do not coincide. The difference between the two is precisely given by the additional time shift  $\Delta t_{\text{Coul}}$  [Eq. (3.8)] induced by the logarithmic distortion of the wave packet.  $\Delta t_{\text{Coul}}$  is universal as it depends only on the energy  $\epsilon = k^2/2$  of the electron and the strength of the Coulomb field  $Z$ , but is independent of the partial wave  $\ell$  or the initial state to be photoionized. It accounts for the “slowing down” of the outgoing electron by the attractive Coulomb field resulting in an apparent negative time shift. Note that the Coulomb-EWS delay is subject to the Wigner causality constraint (Wigner, 1955), i.e.,  $t_{\text{EWS}}^{\text{C}} \geq -\tau_{\text{XUV}}$ , while  $t_{\text{Coul}}$  is not. In principle,  $t_{\text{Coul}}$  can take on arbitrarily large negative values due to the logarithmic divergence of the Coulomb corrected time shift  $\Delta t_{\text{Coul}}$ .

The exit-channel Coulomb interaction is not only the cause of the complications in terms of the modification of the EWS time delay [Eq. (3.7)] but also provides unprecedented opportunities to explore in detail the quantum-classical correspondence for the time delay as an observable. As is well known for Coulomb scattering (Landau and Lifshitz, 1958; McDowell and Coleman, 1970), the close quantum-classical correspondence follows from the fact that the de Broglie wavelength of the scattered particle  $\lambda_{\text{dB}} = 2\pi/\sqrt{2\epsilon}$  is negligibly small compared to the infinite range ( $a \rightarrow \infty$ ) of the Coulomb potential for all energies  $\epsilon$ . This allows one to directly and unambiguously relate the expectation value of the quantum observable time delay to travel times on classical trajectories for all energies of the photoionized electron.

Following Clark (1979), we calculate the classical Coulomb time shift  $t_{\text{Coul}}^{\text{cl}}$  of an electron in the Coulomb field relative to that of a free electron (Pazourek, Nagele, and Burgdörfer, 2013). Solving the equation of motion for a hyperbolic Kepler trajectory of fixed classical angular momentum  $L$  we find for  $r \rightarrow \infty$

$$\begin{aligned} t_{\text{Coul}}^{\text{cl}}(\epsilon, L, r = kt) &= t(r) - \frac{r}{k} \\ &\approx \frac{Z}{(2\epsilon)^{3/2}} \left[ 1 - \ln \left( \frac{4\epsilon t}{\sqrt{\eta^2 + L^2}} \right) \right]. \end{aligned} \quad (3.11)$$

Decomposing Eq. (3.11) into those contributions that are  $r$  (or  $t$ ) dependent and those that are  $r$  independent leads to

$$t_{\text{Coul}}^{\text{cl}}(\epsilon, L, r = kt) = \frac{Z}{(2\epsilon)^{3/2}} \ln \left( \sqrt{\eta^2 + L^2} \right) + \Delta t_{\text{Coul}}(\epsilon, r = kt), \quad (3.12)$$

where the  $r$ - (or time-) dependent  $\Delta t_{\text{Coul}}$  agrees precisely with the Coulomb correction of the quantum wave packet [Eqs. (3.8) and (3.10)]. Comparing Eq. (3.12) with Eq. (3.7) suggests to relate the classical  $r$ -independent first term to the quantum mechanical Coulomb-EWS time Eq. (3.5). To this end, we investigate the semiclassical limit of the quantum EWS delay [Eq. (3.5)] expressed in terms of the digamma function  $\Psi(x)$ :

$$t_{\text{EWS}}^{\text{C}}(\epsilon, \ell) = \frac{Z}{(2\epsilon)^{3/2}} \text{Re}[\Psi(1 + \ell - i\eta)]. \quad (3.13)$$

For large arguments  $|x|$  of  $\Psi(x)$ , reached for either large  $\ell$  or large Coulomb-Sommerfeld parameter  $\eta$ , we obtain

$$\begin{aligned} t_{\text{EWS}}^{\text{C}}(\epsilon, \ell) &\stackrel{|x| \gg 1}{\approx} \frac{Z}{(2\epsilon)^{3/2}} \ln \left( \sqrt{(1 + \ell)^2 + \eta^2} \right) \\ &\approx \frac{Z}{(2\epsilon)^{3/2}} \ln \left( \sqrt{L^2 + \eta^2} \right) = t_{\text{EWS}}^{\text{C,cl}}(\epsilon, L), \end{aligned} \quad (3.14)$$

in complete agreement with the first term in Eq. (3.12). Consequently, we can identify

$$t_{\text{EWS}}^{\text{C,cl}}(\epsilon, L) = \frac{Z}{(2\epsilon)^{3/2}} \ln \left( \sqrt{\eta^2 + L^2} \right) \quad (3.15)$$

as the classical Coulomb-EWS time. In Eq. (3.15) the relation between the angular momentum  $L$  and the  $\ell$  quantum number is established through the semiclassical Langer connection (Langer, 1937; Burgdörfer *et al.*, 1995)  $L \approx \ell + 1/2$ . The convergence of the quantum Coulomb-EWS time [Eq. (3.13)] to its (semi)classical counterpart [Eq. (3.15)] is remarkably fast. Even for modest values of  $|(1 + \ell) - i\eta| \gtrsim 1$  the agreement is excellent [Fig. 3(a)].

The Coulomb-EWS time delay, both classically [Eq. (3.15)] and quantum mechanically [Eq. (3.13)], features a nonseparable coupling between contributions due to the Coulomb potential and the centrifugal potential

$$V(\ell, r) = \frac{\ell(\ell + 1)}{2r^2}. \quad (3.16)$$

This differs from short-ranged potentials for which the asymptotic  $r^{-2}$  tail gives rise to an energy-independent scattering phase  $-\ell\pi/2$ , and, hence, no contribution to the time delay. At fixed energy, the relative delay between partial waves  $\ell$  in the Coulomb field

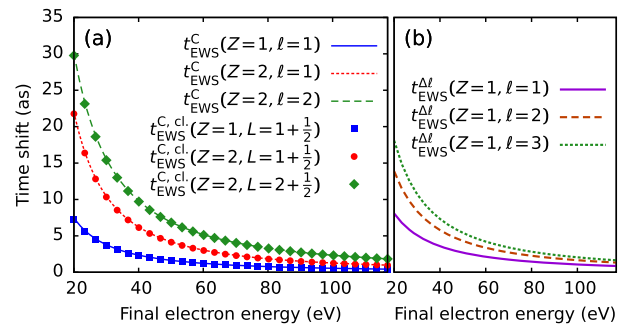


FIG. 3 (color online). Coulomb-EWS times for photoionization from H ( $Z = 1$ ) or  $\text{He}^+$  ( $Z = 2$ ) as a function of the final electron energy  $\epsilon$ . (a) Comparison of the quantum EWS time delay Eq. (3.5) with the classical analog Eq. (3.15) (using the semiclassical mapping of the angular momentum quantum number  $\ell$  to the classical angular momentum  $L = \ell + 1/2$ ). (b) Relative EWS delay  $t_{\text{EWS}}^{\Delta\text{C}}(\epsilon, \ell)$  between partial waves  $\ell$  and  $\ell = 0$  [Eq. (3.17)] as a function of  $\epsilon$ .

$$\begin{aligned} t_{\text{EWS}}^{\Delta\ell}(\epsilon, \ell) &= t_{\text{EWS}}^{\text{C}}(\epsilon, \ell) - t_{\text{EWS}}^{\text{C}}(\epsilon, 0) \\ &= \sum_{j=1}^{\ell} \frac{1}{\sqrt{2\epsilon}} \frac{Zj}{2\epsilon Zj^2 + Z^2} \end{aligned} \quad (3.17)$$

monotonically increases with  $\ell$  and scales as  $\sim \epsilon^{-3/2}$  [Fig. 3(b)]. Remarkably, this relative delay has been first observed in time-integral but angle- and spin-resolved photoemission (Heinzmann and Dil, 2012; Heinzmann, 2013).

The close correspondence between the quantum and classical time shifts for Coulomb-interacting particles has several important consequences. The quantum EWS time delay expressed in terms of the energy derivative of a (quantum) scattering phase [Eqs. (2.27) and (3.5)] can be unambiguously identified with a bona-fide classical delay time on a trajectory measured by a classical clock. Moreover, for time-resolved photoionization, contributions due to long-range Coulomb interactions in the exit channel can be accounted for both classically and quantum mechanically to a high degree of accuracy, thereby allowing one to clearly disentangle intrinsic short-ranged delay times in complex systems from Coulomb-induced time shifts. In this context, it is convenient to exploit the close quantum-classical correspondence one more time to spatially disentangle the two contributions to the Coulomb time delay [Eq. (3.7)], the Coulomb-EWS delay  $t_{\text{EWS}}^{\text{C}}$ , and the time shift correction  $\Delta t_{\text{Coul}}$ , from each other. To this end, we employ the properties of the  $S$  matrix for a Coulomb potential with a cutoff at a finite radius  $r = R_{\text{cut}}$  (Taylor, 1974) and decompose the Coulomb potential as

$$\begin{aligned} V_{\text{C}}(r) &= -\frac{Z}{r} [\theta(R_{\text{cut}} - r) + \theta(r - R_{\text{cut}})] \\ &= V_{\text{short}}(r) + V_{\text{asym}}(r) \end{aligned} \quad (3.18)$$

into a short-ranged potential

$$V_{\text{short}}(r) = -\frac{Z}{r} \theta(R_{\text{cut}} - r) \quad (3.19)$$

and an asymptotic tail

$$V_{\text{asym}}(r) = -\frac{Z}{r} \theta(r - R_{\text{cut}}). \quad (3.20)$$

For the short-ranged part, standard scattering theory applies and yields for the  $S$  matrix in the partial-wave basis

$$S_{\ell}^{\text{short}}(\epsilon) = e^{2i\delta_{\ell}^{\text{short}}(\epsilon)} \quad (3.21)$$

with

$$\delta_{\ell}^{\text{short}}(\epsilon) \simeq \sigma_{\ell}^{\text{C}}(\epsilon) + \frac{Z}{k} \ln(2kR_{\text{cut}}) \quad (3.22)$$

up to corrections to order  $Z(2kR_{\text{cut}})^{-1}$  (Taylor, 1974). For large  $R_{\text{cut}} \rightarrow \infty$ , the Coulomb phase shift is recovered while for any finite  $R_{\text{cut}}$ , the logarithmically divergent phase is now unambiguously associated with the potential  $V_{\text{asym}}$ . The EWS delay for the short-ranged part follows from Eq. (3.22) as

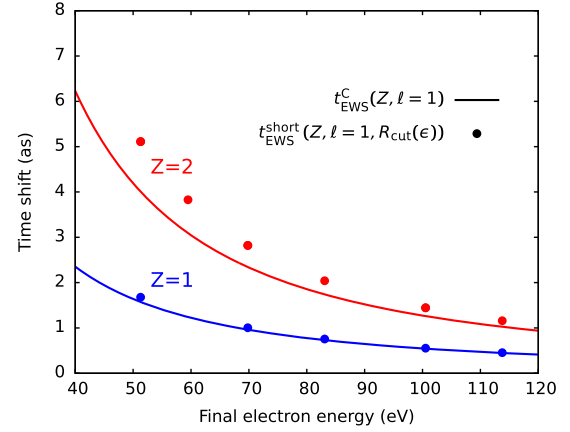


FIG. 4 (color online). Comparison between the Coulomb-EWS delay  $t_{\text{EWS}}^{\text{C}}(\epsilon)$  [Eq. (3.5)] and the delay due to the short-ranged cutoff potential [Eq. (3.19)],  $t_{\text{EWS}}^{\text{short}}(\epsilon, \ell)$  [Eq. (3.23)], for a cutoff  $R_{\text{cut}}(\epsilon)$  given by Eq. (3.24).

$$t_{\text{EWS}}^{\text{short}}(\epsilon) = t_{\text{EWS}}^{\text{C}} + \frac{Z}{(2\epsilon)^{3/2}} [1 - \ln(2\sqrt{2\epsilon}R_{\text{cut}})]. \quad (3.23)$$

If one now chooses the cutoff radius  $R_{\text{cut}}$  such that  $\ln(2\sqrt{2\epsilon}R_{\text{cut}}) = 1$ , the second term in Eq. (3.23) vanishes and the proper EWS delay of the short-ranged potential  $t_{\text{EWS}}^{\text{short}}$  coincides with the Coulomb-EWS delay  $t_{\text{EWS}}^{\text{C}}$ . In turn, the Coulomb correction  $\Delta t_{\text{Coul}}$  is now the time shift exclusively acquired by the motion in the asymptotic potential Eq. (3.20). For applications to photoionization, the cutoff parameter can be chosen for a given central frequency  $\omega_{\text{XUV}}$  to be energy dependent

$$R_{\text{cut}} = \frac{e}{2\sqrt{2}(\omega_{\text{XUV}} + \epsilon_i)}. \quad (3.24)$$

A numerical test (Fig. 4) shows that  $t_{\text{EWS}}^{\text{short}}(\epsilon) = t_{\text{EWS}}^{\text{C}}(\epsilon)$  is fulfilled to a very good degree of approximation. Taking into account this close quantum-classical correspondence, one can, to a good degree of approximation, attribute  $t_{\text{EWS}}^{\text{C}}$  to the delay acquired by the electron on the inner part of the classical trajectory ( $r \lesssim R_{\text{cut}}$ ), while  $\Delta t_{\text{Coul}}$  is the time shift along the outer part of the Kepler hyperbola. Alternative decompositions have been explored in the recent literature (Ivanov and Smirnova, 2011; Nagele *et al.*, 2011, 2014; Dahlström, L'Huillier, and Maquet, 2012; Pazourek, Feist *et al.*, 2012; Dahlström *et al.*, 2013; Pazourek, Nagele, and Burgdörfer, 2013; Su, Ni, Becker, and Jaroń-Becker, 2014).

## IV. ATTOSECOND STREAKING OF PHOTOEMISSION

### A. Streaking principle

Attosecond streaking (Constant *et al.*, 1997; Itatani *et al.*, 2002; Kitzler *et al.*, 2002; Kienberger *et al.*, 2004; Yakovlev, Bammer, and Scrinzi, 2005) has developed into one of the most important and versatile tools of attosecond science. It is a pump-probe technique in which the attosecond XUV pulse (with, typically,  $\tau_{\text{XUV}} = 100$  to 500 as) serves as a pump creating the photoelectron wave packet while the

carrier-envelope phase (CEP) controlled moderately strong (with intensities of the order  $I_{\text{IR}} \approx 10^{11}$  W/cm<sup>2</sup>) linearly polarized few-cycle IR pulse streaks, i.e., probes, the wave packet. In analogy to conventional streaking (Murnane, Kapteyn, and Falcone, 1990; Shepherd *et al.*, 1995; Maksimchuk *et al.*, 1996) that maps time onto distance, attosecond streaking maps time information onto energy thereby allowing one to extract time information from the time-integral photoelectron spectrum with attosecond precision (Drescher *et al.*, 2001, 2002; Hentschel *et al.*, 2001; Goulielmakis *et al.*, 2004; Kienberger *et al.*, 2004; Mairesse and Quéré, 2005; Quéré, Mairesse, and Itatani, 2005; Cavalieri *et al.*, 2007; Gagnon, Goulielmakis, and Yakovlev, 2008; Schultze *et al.*, 2010; Yakovlev *et al.*, 2010). We illustrate the opportunities and challenges in extracting attosecond timing information from spectral information for the example of attosecond streaking by linearly polarized light. Many of the results as well as difficulties apply to alternative protocols as well. The latter include the interferometric RABBIT technique (Véniard, Taïeb, and Maquet, 1996; Paul *et al.*, 2001; Toma and Müller, 2002; Klünder *et al.*, 2011; Guénot *et al.*, 2012, 2014; Palatchi *et al.*, 2014) for ionization by attosecond pulse trains (APT) and angular attosecond streaking by circularly polarized IR pulses (Eckle, Pfeiffer *et al.*, 2008; Eckle, Smolarski *et al.*, 2008; Pfeiffer *et al.*, 2011, 2013; Pfeiffer, Cirelli *et al.*, 2011).

The point of departure for attosecond streaking is that the momentum of the emitted electron receives in the presence of a strong IR field a ponderomotive shift

$$\vec{p}_f(\tau) = \vec{p}_0 - \vec{A}_{\text{IR}}(\tau), \quad (4.1)$$

given by the value of the (for simplicity rescaled) vector potential  $A_{\text{IR}} = \vec{A}_{\text{IR}}(\tau)/c$  at the instant of the arrival in the continuum  $\tau$ , from which time on the liberated electron is accelerated by the electric field. In Eq. (4.1),  $\vec{p}_0$  is the asymptotic momentum associated with the energy of the photoelectron  $E_0 = p_0^2/2$  ( $E_0 = \omega_{\text{XUV}} + \epsilon_i$ ) in the absence of the streaking field. Following Eq. (4.1) the momentum  $\vec{p}_f(\tau)$  and the energy  $E_f(\tau) = \vec{p}_f^2(\tau)/2$  in the presence of the IR field become functions of  $\tau$  via  $\vec{A}_{\text{IR}}$ . Since the temporal distribution of a CEP controlled IR laser field  $\vec{F}_{\text{IR}}(\tau)$  and the associated vector potential  $\vec{A}_{\text{IR}}(\tau)$ ,

$$\vec{A}_{\text{IR}}(\tau) = \int_{\tau}^{\infty} \vec{F}_{\text{IR}}(t) dt, \quad (4.2)$$

can be well controlled with subcycle precision, Eq. (4.1) amounts to a mapping of the time  $\tau$  onto the modulation of the linear momentum  $\vec{p}_f(\tau)$  or the energy  $E_f(\tau)$  of the photoelectron. If ionization were truly instantaneous,  $\tau$  would be the delay of the IR pulse relative to the peak of the XUV pulse (at  $t_a = 0$ ).

One implicit assumption underlying Eq. (4.1) is that the emitted electron attains instantaneously the asymptotic momentum  $\vec{p}_0$  on a time scale resolvable by attosecond streaking. Another assumption is that the wave packet propagation in the continuum is dominated by the electromagnetic vector potential rather than by the interaction with

the remaining ionic fragment in the exit channel. We also require that the kinetic energy of the emitted electron is high enough so that it is not driven back to the residual complex by the IR field [see Xu *et al.* (2011) and Hou *et al.* (2012) for a discussion of attosecond streaking in the low-energy region]. This particular variant of a “strong-field” approximation requires, in fact, a much weaker laser intensity than typically invoked in the strong-field approximation to ionization [see Joachain, Kylstra, and Potvliege (2012) and references therein]. The validity of these assumptions will be explored in more detail later.

A typical streaking spectrogram [Fig. 5(b)] generated by an attosecond XUV pulse and a few-cycle IR pulse time delayed relative to another [Fig. 5(a)] yields a momentum distribution  $\vec{p}_f$  along the polarization axis of the  $\vec{A}_{\text{IR}}$  field or, equivalently, the differential energy distribution in the forward ( $\theta = 0^\circ$ ) or backward direction ( $\theta = 180^\circ$ ) modulated by the temporal distribution of the  $A_{\text{IR}}$  field. Identification of the time information encoded in such a streaking trace is key to observe attosecond-time-resolved processes.

The interrogation by the streaking field can be viewed as a measurement by a clock. For long-lived excitations of continuum states, e.g., resonances in the continuum (Drescher *et al.*, 2002; Wickenhauser *et al.*, 2005, 2006; Ott *et al.*, 2013) or long XUV pulses  $\tau_{\text{XUV}} \gtrsim T_{\text{IR}}$  ( $T_{\text{IR}}$  is the cycle period of the IR field), the streaking information appears in the spectral sidebands separated by multiples of the photon

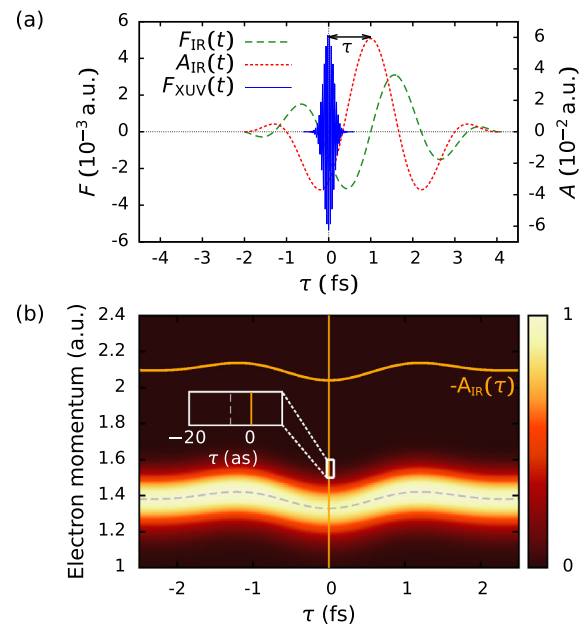


FIG. 5 (color online). Simulation of attosecond streaking: (a) Typical temporal profile of streaking fields. IR laser field with  $\lambda = 800$  nm, a sine-squared envelope and total duration of 6 fs, and an intensity of  $I_{\text{IR}} = 4 \times 10^{11}$  W/cm<sup>2</sup>. The XUV pulse has a Gaussian envelope, a FWHM duration of 200 as, and an intensity of  $I_{\text{XUV}} = 10^{13}$  W/cm<sup>2</sup>. (b) Streaking spectrogram for ionization of a model atom with Yukawa-like short-ranged exit-channel interaction [Eq. (2.36)]. For reference the vector potential  $A_{\text{IR}}(\tau)$  is also shown (solid line). Comparison with the shift of the spectrogram (dashed line) yields the streaking time shift (see the inset).

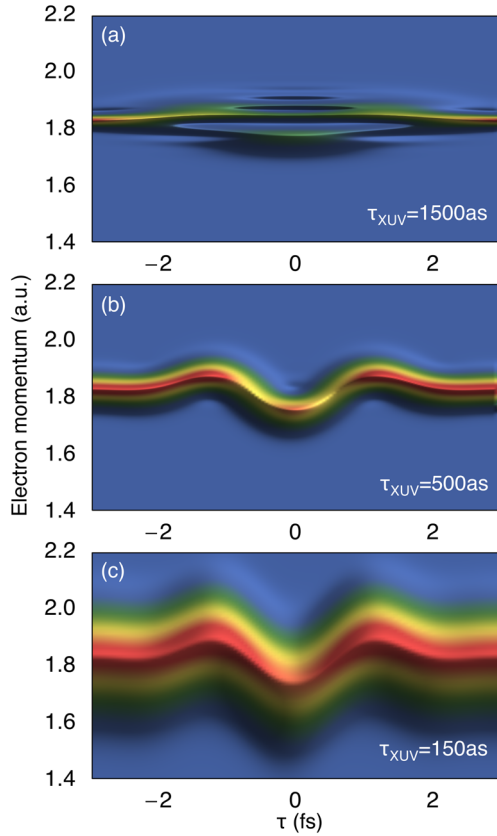


FIG. 6 (color online). Simulation of streaking spectrograms for ionization from the Yukawa ground state for different XUV-pulse durations  $\tau_{\text{XUV}}$ ,  $\hbar\omega = 100$  eV, and  $I_{\text{XUV}} = 10^{13}$  W/cm<sup>2</sup>. The IR field had a total duration of 6 fs with a sine-squared envelope  $\lambda = 800$  nm and  $I_{\text{IR}} = 10^{12}$  W/cm<sup>2</sup>. The duration of one optical cycle is 2668 as. The spectra are taken in the forward direction ( $p = p_z$ ) with an opening angle of  $10^\circ$ .

energy  $\omega_{\text{IR}}$  [Fig. 6(a)]. The pioneering proof of principle experiment (Drescher *et al.*, 2002) measuring the lifetime of 8 fs of an Auger resonance in krypton pertained to this regime. This limit of quantized probe-field interaction is referred to in the following as a quantum clock. The notion of a quantum clock was originally introduced by Salecker and Wigner (1958) treating the system to be interrogated and the measuring device, the “clock,” as a coupled system following the rules of quantum dynamics. By contrast, a classical clock refers to (not necessarily macroscopic) decoherent environmental degrees of freedom described by classical dynamics.

Translating this concept to the present scenario where the system to be clocked is an XUV-pulse excited (many) electron system and the interaction with the IR-probe pulse represents the clock, we refer to measurement protocols that exploit the quantized interaction with the IR field, in particular, interferometric processes, as quantum clocks while those invoking only classical electron-IR field interactions as classical clocks. The recovery of timing information from the quantized spectral sidebands can therefore be viewed as a realization of a quantum clock. This limit also applies to the RABBIT interferometry for APTs (Paul *et al.*, 2001) extending over many femtoseconds and optical cycles. In the opposite limit of short-lived excitations (Drescher and Krausz, 2005;

Wickenhauser *et al.*, 2005, 2006) or single attosecond pulses with  $\tau_{\text{XUV}} \ll T$  (Goulielmakis *et al.*, 2004, 2007, 2008; Sansone *et al.*, 2006; Gilbertson, Khan *et al.*, 2010; Zhao *et al.*, 2012), attosecond streaking [Eqs. (4.1) and (4.2)] approaches the limit of a measurement by a classical clock. Figure 6 illustrates the transition between the two regimes. The hallmark for the approach of the classical limit is the gradual disappearance of the interference modulations, visible in Fig. 6(a), until only the classical oscillations of the ponderomotive shift survive [Fig. 6(c)]. We primarily focus on the latter regime as it facilitates the intuitive, classical interpretation of time and time delay extracted from quantum dynamics and illustrates quantum-classical correspondence. However, as the interrogating field is moderately strong, the presence of the IR field may distort the timing information to be extracted. Since for easily resolvable energy shifts IR fields with intensities of the order of  $I_{\text{IR}} \approx 10^{11}$  to  $10^{12}$  W/cm<sup>2</sup> are needed, such distortion effects generally cannot be neglected. The task is, thus, to disentangle probe-field-induced modifications of the elements of the  $S$  matrix,  $S_{\text{XUV-IR}}$  [Eq. (2.20)], from properties of the original  $S$  matrix ( $S_{\text{XUV}}$ ) for photoemission [Eq. (2.6)].

## B. Attosecond streaking for short-ranged potentials

The analysis of the time extracted by attosecond streaking becomes particularly simple when only short-ranged potentials govern the motion of the electronic wave packet in the exit channel. We expose the model atom with a Yukawa-type screened potential [Eqs. (2.35) and (2.36)] to both an XUV pulse and an IR streaking pulse shifted relative to each other by the delay  $\tau$ . A fit of the first moment  $\langle p_{f,z} \rangle$  or, equivalently, the peak of the momentum distribution to the temporal distribution of the  $A_{\text{IR}}$  field [Eq. (4.1)], also shown in Fig. 5(b), reveals a miniscule but unambiguously determined streaking time shift  $t_{\text{S}}$

$$\vec{p}_f(\tau) = \vec{p}_0 - \vec{A}_{\text{IR}}(\tau + t_{\text{S}}) \quad (4.3)$$

relative to the XUV-pump IR-probe delay  $\tau$ . Remarkably, this streaking time agrees with subattosecond precision [Fig. 7(a)] with the EWS time delay for this model system (see Sec. II) over a wide range of energies and different screening lengths provided the latter are small compared to the de Broglie wavelength  $\lambda_{\text{dB}}$  of the outgoing electron 1 a.u.,  $a \lesssim \lambda_{\text{dB}}$  (Nagele *et al.*, 2011, 2014). In the case of short-ranged potentials we can unambiguously identify from the numerical simulations

$$t_{\text{S}} = t_{\text{EWS}}, \quad (4.4)$$

and, hence,

$$\vec{p}_f(\tau) = \vec{p}_0 - \vec{A}_{\text{IR}}(\tau + t_{\text{S}}) = \vec{p}_0 - \vec{A}_{\text{IR}}(\tau + t_{\text{EWS}}). \quad (4.5)$$

It is thus the group delay of the outgoing wave packet that attosecond streaking measures. This result is expected to hold for other short-ranged potentials of comparable range as well (Zhang and Thumm, 2011c; Su *et al.*, 2013c). One important

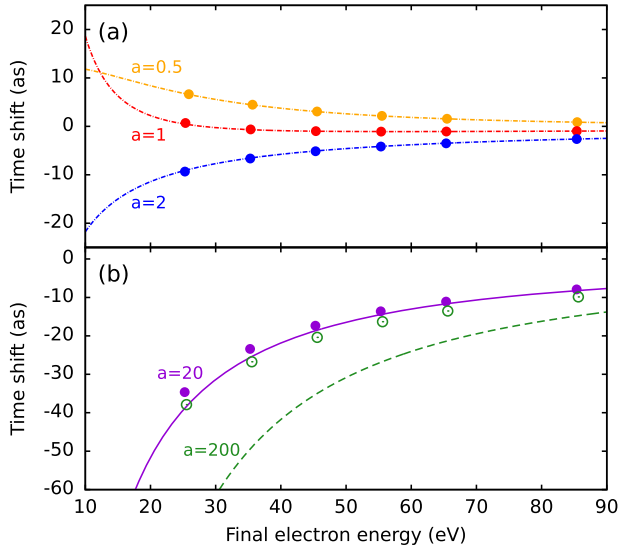


FIG. 7 (color online). Streaking time shifts  $t_S$  (dots) extracted from quantum mechanical simulations and  $t_{EWS}$  (lines) determined from the spectral variation of the scattering phase for the short-ranged Yukawa potential  $V_Y$  [Eq. (2.36)]. (a) Small screening length ( $a \lesssim \lambda_{dB}$ ):  $a = 0.5, 1, 2$ ; (b) large screening length ( $a \gg \lambda_{dB}$ ):  $a = 20$  (solid dots and line),  $a = 200$  (open dots and dashed line). The streaking IR laser field has a wavelength of 800 nm, a total duration of 6 fs, and an intensity of  $10^{12}$  W/cm $^2$ .

caveat is highlighted in Fig. 7(b). For large screening lengths  $a \gg \lambda_{dB}$ , i.e., when the potential increasingly resembles a Coulomb potential, the correspondence between  $t_S$  and  $t_{EWS}$  starts to break down (Nagele *et al.*, 2014). This difficulty points to the modifications required for attosecond streaking with long-range Coulomb interactions in the exit channel.

### C. Streaking in the presence of a Coulomb field

In photoionization of an initially charge-neutral system (atom, molecule, or solid surface), the exit-channel interactions of the outgoing electron with the residual ionic system inevitably feature a Coulombic long-range tail in addition to channel-specific short-ranged interactions. Understanding the extraction of timing information by attosecond streaking in a pure Coulomb field is therefore of central importance.

The full numerical solution of the 3D-TDSE for the streaking of the prototypical case, ionization of hydrogen H(1s), by an attosecond XUV pulse (Fig. 8) clearly shows that the time shift  $t_S$  extracted from the streaking diagram strongly differs from the Coulomb-EWS delay (Nagele *et al.*, 2011). The difference to the EWS delay

$$t_{CLC}(Z = 1, E, \omega_{IR}) = t_S[H(1s)] - t_{EWS}^C(E, \ell = 1) \quad (4.6)$$

is often referred to as the Coulomb-laser coupling (CLC) time shift (Smirnova, Spanner, and Ivanov, 2006; Smirnova *et al.*, 2007; Zhang and Thumm, 2010). The origin of the CLC contribution lies in the additional logarithmic phase distortion [Eqs. (3.6)–(3.8)] present for Coulomb interactions in the exit channel. The interaction of the outgoing electron with the IR field maps a finite portion of the Coulomb correction  $\Delta t_{Coul}$

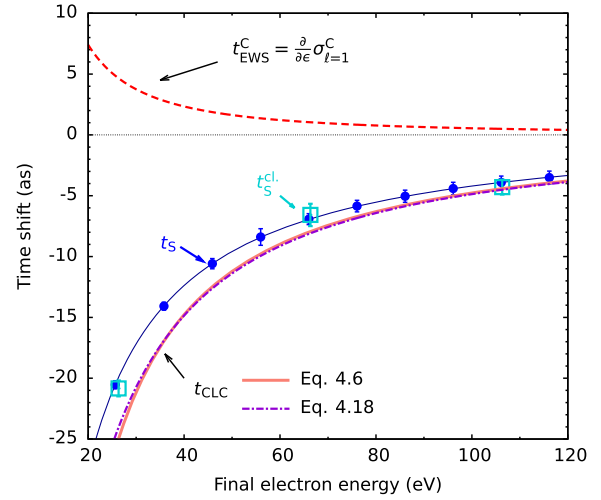


FIG. 8 (color online). Comparison between the streaking time shift  $t_S$  and the Coulomb-EWS time delay  $t_{EWS}^C$  for photoionization of hydrogen as a function of the final kinetic energy  $\epsilon$  of the outgoing electron ( $\epsilon = \omega + \epsilon_i$ ). Also shown is the classical streaking time shift  $t_S^{cl}$  calculated with the CTMC method (open squares). Classical and quantum  $t_S$  agree with each other to within the graphical resolution when the mapping between classical and quantum angular momentum  $L = \ell + 1/2$  is used. The analytic approximation  $\Delta \overline{t_{Coul}}$  [Eq. (4.18)] coincides with the numerical quantum result for  $t_{CLC}$  [Eq. (4.6)] to within a fraction of an attosecond.

[Eq. (3.8)] directly onto the observed streaking time shift. Remarkably, a simulation based on the classical trajectory Monte Carlo (CTMC) method (Abrines and Percival, 1966; Dimitriou *et al.*, 2004) yields  $t_S$  in close agreement with the TDSE result (Nagele *et al.*, 2011; Su *et al.*, 2013a). Within a CTMC treatment an average over the microcanonical ensemble of starting positions  $\vec{r}$  representing the initial state is taken and, therefore, the results are independent of a particular choice of initial conditions. This differs from a semiclassical model by Ivanov and Smirnova (2011), where  $r_0$  is introduced as an adjustable matching parameter. This approximate model treats the Coulomb interaction as a perturbative correction to the IR-field interaction and has been shown to result in deviations from the exact classical (CTMC) or quantum (TDSE) solution for moderate streaking fields (Su *et al.*, 2013a). This error can be partially compensated by adjusting  $r_0$ .

The close quantum-classical correspondence for the Coulomb time delay [Eqs. (3.12) and (3.14)] allows for a simple and intuitive trajectory-based description of  $t_{CLC}$ . The classical asymptotic momentum in the presence of the streaking field  $\vec{p}_f(\tau)$  as a function of the delay  $\tau$  between the ionizing XUV field peak and the peak in the envelope of the streaking field for a trajectory taking off near the nucleus  $\vec{r}_i(\tau) \simeq 0$  is given by

$$\vec{p}_f(\tau) = \vec{p}_i(\tau) + \int_{\tau}^{\infty} \vec{a}_{C+IR}[\vec{r}(t)] dt, \quad (4.7)$$

where  $\vec{a}_{C+IR}[\vec{r}(t)]$  denotes the acceleration along the trajectory  $\vec{r}(t)$  in the combined Coulomb and IR fields. If only the Coulomb field were present, Eq. (4.7) reduces to

$$\vec{p}_f(\tau) = \vec{p}_i(\tau) + \int_{\tau}^{\infty} a_C[\vec{r}(t)]dt = \vec{p}_0, \quad (4.8)$$

with  $\vec{p}_0$  the asymptotic momentum of the photoionized electron with  $p_0 = \sqrt{2(\omega_{\text{XUV}} + \epsilon_i)}$ . Conversely, if only the IR field were present, we recover the standard streaking expression [Eq. (4.1)]

$$\begin{aligned} \vec{p}_f(\tau) &= \vec{p}_i(\tau) + \int_{\tau}^{\infty} a_{\text{IR}}[\vec{r}(t)]dt \\ &= \vec{p}_i(\tau) - \int_{\tau}^{\infty} \vec{F}_{\text{IR}}(t)dt = \vec{p}_0(\tau) - \vec{A}_{\text{IR}}(\tau). \end{aligned} \quad (4.9)$$

In Eq. (4.9)  $\vec{p}_i(\tau)$  is replaced by  $\vec{p}_0(\tau)$  since in the absence of a long-ranged exit-channel potential the local momentum coincides with the asymptotic momentum. Note that the trajectories along which Eqs. (4.7) to (4.9) are integrated will be different for each of the three cases for identical initial conditions. Inserting Eqs. (4.8) and (4.9) into Eq. (4.7) yields the Coulomb-modified streaking equation

$$\begin{aligned} \vec{p}_f(\tau) &= \vec{p}_0 - \vec{A}_{\text{IR}}(\tau) \\ &+ \int_{\tau}^{\infty} \{a_{\text{C+IR}}[\vec{r}(t)] - a_C[\vec{r}(t)] - a_{\text{IR}}[\vec{r}(t)]\}dt. \end{aligned} \quad (4.10)$$

The integral in Eq. (4.10) can now be easily estimated exploiting the spatial decomposition of the Coulomb potential into a short-ranged potential and an asymptotic tail [Eq. (3.18)]. For the short-ranged part we find to leading order in the IR-field induced variations of the trajectory

$$\begin{aligned} \int_{\tau}^{t(R_{\text{cut}})} \{a_{\text{C+IR}}[\vec{r}(t)] - a_C[\vec{r}(t)] - a_{\text{IR}}[\vec{r}(t)]\}dt \\ = c_{\text{short}}(\epsilon, Z, L)F_{\text{IR}}(\tau). \end{aligned} \quad (4.11)$$

Analogously,

$$\begin{aligned} \int_{t(R_{\text{cut}})}^{\infty} \{a_{\text{C+IR}}[\vec{r}(t)] - a_C[\vec{r}(t)] - a_{\text{IR}}[\vec{r}(t)]\}dt \\ = c_{\text{asym}}(\epsilon, Z, \omega_{\text{IR}})F_{\text{IR}}(\tau). \end{aligned} \quad (4.12)$$

Explicit expressions for  $c_{\text{short}}$  and  $c_{\text{asym}}$  will be given below. Combining Eqs. (4.11) and (4.12) with Eq. (4.10) yields the Coulomb-streaking equation

$$\vec{p}_f(\tau) = \vec{p}_0 - \vec{A}_{\text{IR}}(\tau + t_{\text{EWS}}^{\text{C,cl}} + t_{\text{CLC}}), \quad (4.13)$$

with

$$t_{\text{EWS}}^{\text{C,cl}} = \frac{1}{\omega_{\text{IR}}} \tan^{-1} [\omega_{\text{IR}} c_{\text{short}}(\epsilon, Z, L)] \quad (4.14)$$

and

$$t_{\text{CLC}} = \frac{1}{\omega_{\text{IR}}} \tan^{-1} [\omega_{\text{IR}} c_{\text{asym}}(\epsilon, Z, \omega_{\text{IR}})]. \quad (4.15)$$

Equation (4.14) is an immediate consequence of the streaking principle for short-ranged potentials  $t_S = t_{\text{EWS}}$

[Eq. (4.5)]. The amplitude  $c_{\text{short}}$  can be determined by inserting Eq. (3.14) into Eq. (4.14),

$$c_{\text{short}}(\epsilon, Z, L) = \frac{1}{\omega_{\text{IR}}} \tan \left( \frac{\omega_{\text{IR}} Z}{(2\epsilon)^{3/2}} \ln(\sqrt{\eta^2 + L^2}) \right). \quad (4.16)$$

Analogously, the explicit determination of  $t_{\text{CLC}}$  makes use of the fact that the asymptotic tail of the Coulomb potential gives rise to the logarithmic phase shift and, thus, to the Coulomb correction to the time shift [Eqs. (3.8) and (3.10)]  $\Delta t_{\text{Coul}}(\epsilon, r = kt)$ . An ensemble of classical trajectories samples the temporal average over this correction to the time delay

$$\overline{\Delta t_{\text{Coul}}} = \frac{1}{\Delta T} \int_{t(R_{\text{cut}})}^{t(R_{\text{cut}}) + \Delta T} dt \Delta t_{\text{Coul}}(\epsilon, r = kt) \quad (4.17)$$

over a finite time interval  $\Delta T$ . Since this phase shift is sampled in the streaking field over only a finite time interval, a well-defined finite contribution to the streaking time shift emerges (Pazourek, Nagele, and Burgdörfer, 2013; Su *et al.*, 2013a; Su, Ni, Becker, and Jaroń-Becker, 2014). For interference modulations to disappear and the classical limit of streaking to hold, the XUV-pulse duration should satisfy  $\tau_{\text{XUV}} \lesssim T_{\text{IR}}/4$  [see Fig. 6]. Even slow photoelectrons will escape the Coulomb field during a fraction of an optical cycle of the IR field. Setting  $t(R_{\text{cut}}) = 0$  and  $\Delta T = T_{\text{IR}}/4$ , Eq. (4.17) yields

$$\begin{aligned} t_{\text{CLC}}(Z, \epsilon, \omega_{\text{IR}}) &= \overline{\Delta t_{\text{Coul}}}(\Delta T = T_{\text{IR}}/4) \\ &= \frac{Z}{(2\epsilon)^{3/2}} [2 - \ln(\epsilon T_{\text{IR}})]. \end{aligned} \quad (4.18)$$

For a wide range of electron energies, nuclear charges, and IR frequencies, this simple analytic estimate agrees remarkably well with the  $t_{\text{CLC}}$  from the numerically exact quantum as well as CTMC simulations with errors typically less than 1 as (Fig. 8).  $t_{\text{CLC}}$  [Eq. (4.18)] depends on  $Z$ , on  $\epsilon$ , and on the streaking-field period  $T_{\text{IR}}$  (or, equivalently, its frequency  $\omega_{\text{IR}} = 2\pi/T_{\text{IR}}$ ). It is, however, independent of the IR-field strength. In practice, the IR intensity should be weak enough in order to prevent field ionization and depletion of the system to be ionized but it should be strong enough to cause easily detectable energy modulations of the emitted electron (typical values are  $10^{10} \leq I_{\text{IR}} \leq 10^{12}$  W/cm<sup>2</sup>). The remarkable and, at first glance, counterintuitive independence of  $I_{\text{IR}}$  is an immediate consequence of the fact that Coulomb-laser coupling results in a momentum shift proportional to the field  $\vec{F}_{\text{IR}}$  [Eq. (4.12)] being  $\pi/2$  phase shifted relative to the  $\vec{A}_{\text{IR}}$  field since  $\vec{F}_{\text{IR}} = -(\partial/\partial t)\vec{A}_{\text{IR}}$ . Consequently, the amplitude of a contribution  $\sim \vec{F}_{\text{IR}}$  to the unperturbed streaking shift  $\sim \vec{A}_{\text{IR}}$  [Eq. (4.9)] yields a phase shift, or time shift, that is independent of the modulus of  $A_{\text{IR}}$ . The  $t_{\text{CLC}}$  time shift is also largely independent of the duration and shape of the IR streaking pulse. Combining Eqs. (4.15) and (4.18) yields the following approximate expression for  $c_{\text{asym}}$ :

$$c_{\text{asym}}(\epsilon, Z, \omega_{\text{IR}}) \simeq \frac{1}{\omega_{\text{IR}}} \tan \left( \frac{\omega_{\text{IR}} Z}{(2\epsilon)^{3/2}} [2 - \ln(\epsilon T_{\text{IR}})] \right). \quad (4.19)$$

Within the classical analysis, the strict additivity of the contributions to the streaking time

$$t_S = t_{\text{EWS}}^{\text{C}}(\epsilon, \ell, Z) + t_{\text{CLC}}(\epsilon, Z, \omega_{\text{IR}}) \quad (4.20)$$

also observed in the quantum simulations is an immediate consequence of the spatial separation of the short-ranged and long-ranged potential contributions along the trajectories [Eq. (3.18)]. One important consequence of Eq. (4.20) is that the EWS delay for photoionization in the presence of long-range Coulomb interactions becomes accessible by attosecond streaking since the time shift  $t_{\text{CLC}}$  can be independently determined either by a numerical streaking simulation for a Coulomb potential or approximately by Eq. (4.18).

It is of conceptual interest to compare the time information extracted by streaking for Coulomb-final-state interactions [Eq. (4.20)] with that extracted by the interferometric method of RABBIT (Paul *et al.*, 2001; Toma and Muller, 2002; Mauritsson, Gaarde, and Schafer, 2005; Klünder *et al.*, 2011; Dahlström, L’Huillier, and Maquet, 2012; Guénot *et al.*, 2012). The time shift observed by RABBIT  $t_{\text{R}}$  can also be written as a sum of an intrinsic atomic delay and an IR field-induced shift, referred to in this context as continuum-continuum coupling (Klünder *et al.*, 2011; Dahlström, L’Huillier, and Maquet, 2012; Dahlström *et al.*, 2013),

$$t_{\text{R}} = t_{\text{EWS}}^{\text{C}} + \tau_{\text{cc}}. \quad (4.21)$$

A quantitative comparison (Fig. 9) between  $t_S$  [Eq. (4.20)] and  $t_{\text{R}}$  [Eq. (4.21)] for photoemission of  $\text{He}^+(1s)$  yields excellent

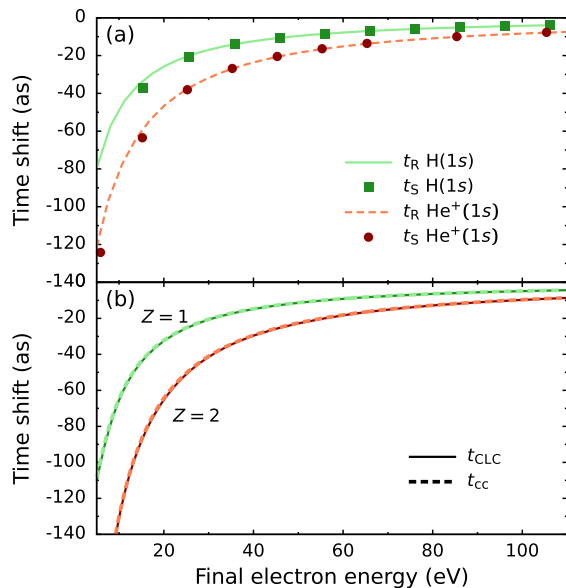


FIG. 9 (color online). Comparison between simulations of streaking and RABBIT: (a) Comparison between the streaking times  $t_S$  and RABBIT time shifts  $t_{\text{R}}$ . For streaking single attosecond pulses with  $\tau_{\text{XUV}} = 200$  as and variable  $\omega_{\text{XUV}}$  are used; for RABBIT APTs built of harmonics from  $q = 9$  to  $q = 81$  of the fundamental  $\omega_{\text{IR}}$  ( $\lambda = 800$  nm) are employed. (b) Comparison between the analytic approximation to  $t_{\text{CLC}}$  [Eq. (4.18)] and  $\tau_{\text{cc}}$  [Eq. (100)] from Dahlström, L’Huillier, and Maquet, 2012].

agreement over a wide range of energies. Small deviations appear at low kinetic energies. Since RABBIT employs APTs rather than single attosecond pulses, the frequency range explored in Fig. 9 is covered by a broad range of harmonics in the APT ranging from  $q = 9$  to  $q = 81$  of the fundamental  $\omega_{\text{IR}}$  with  $\lambda = 800$  nm. This agreement is quite remarkable for several reasons: RABBIT employs long pulses for which the quantum path interferences control the interaction of the interrogating pulse with the system while attosecond streaking acts as a classical clock. Moreover, RABBIT relies on lowest-order perturbation theory for a combined  $\omega_{\text{XUV}} + \omega_{\text{IR}}$  two-photon absorption process while streaking involves moderately strong fields. The energy modulations correspond to an exchange of several  $\omega_{\text{IR}}$  photons (e.g.,  $\sim 4$  photons in the example of Fig. 6 with  $I_{\text{IR}} = 10^{12}$  W/cm<sup>2</sup>). Nevertheless, the time shifts introduced by the probing field  $t_{\text{CLC}}$  and  $\tau_{\text{cc}}$  are in excellent agreement with each other [Fig. 9(b)]. One key in understanding this remarkable agreement is the intensity independence of  $t_{\text{CLC}}$  [Eq. (4.18)] indicating that the Coulomb-laser coupling contribution to the time shift is present in both the single-photon and multiphoton regimes. This underlines the fact that  $t_{\text{EWS}}$  can be unambiguously extracted by conceptually entirely different methods provided that the additional contributions  $t_{\text{CLC}}$  or, equivalently,  $\tau_{\text{cc}}$  are accounted for.

#### D. Dipole-laser coupling

As indicated by the interplay between the Coulomb potential and the centrifugal potential [Eq. (3.16)] for the Coulomb-EWS delay  $t_{\text{EWS}}^{\text{C}}$  [Eqs. (3.13) and (3.17)], interactions decaying asymptotically as  $V \sim r^{-2}$  provide an interesting intermediate case at the borderline between short- and long-ranged interactions. Another important example is permanent dipole interactions also decaying as  $V_d \sim r^{-2}$ . Their influence on streaking was first discussed by Baggese and Madsen (2010a, 2010b). Permanent dipole interactions are present for molecules, while quasipermanent dipoles (on the time scale of the laser pulse duration) appear for systems with near-degenerate manifolds of states with opposite parity. A particularly simple case is photoionization of degenerate hydrogenic manifolds where dipolar interactions are present in the entrance channel and Coulomb interactions in the exit channel. We consider the substate dependence of the time shift in photoionization of the  $n = 2$  manifold of  $\text{He}^+(n = 2)$ . Unlike the states of well-defined parity  $\text{He}^+(n\ell m)$ , the two parabolic states  $\text{He}^+(n = 2, k = \pm 1)$  feature a permanent electric dipole moment of  $d_{k=\pm 1} = \pm 3n/2Z$  (or, more precisely, a quasipermanent dipole moment oscillating on a  $\sim 100$  ps time scale when relativistic and quantum-electrodynamical corrections are included). The effect of the initial-state polarization on the photoionization transition matrix element is fully contained in the Coulomb-EWS time [Fig. 10(a)]. However, in the presence of the IR streaking field, its interaction with the initial-state dipole prior to photoionization leads to a time-dependent initial-state energy shift

$$\Delta E(\tau) = -\vec{d} \cdot \vec{F}_{\text{IR}}(\tau) \quad (4.22)$$

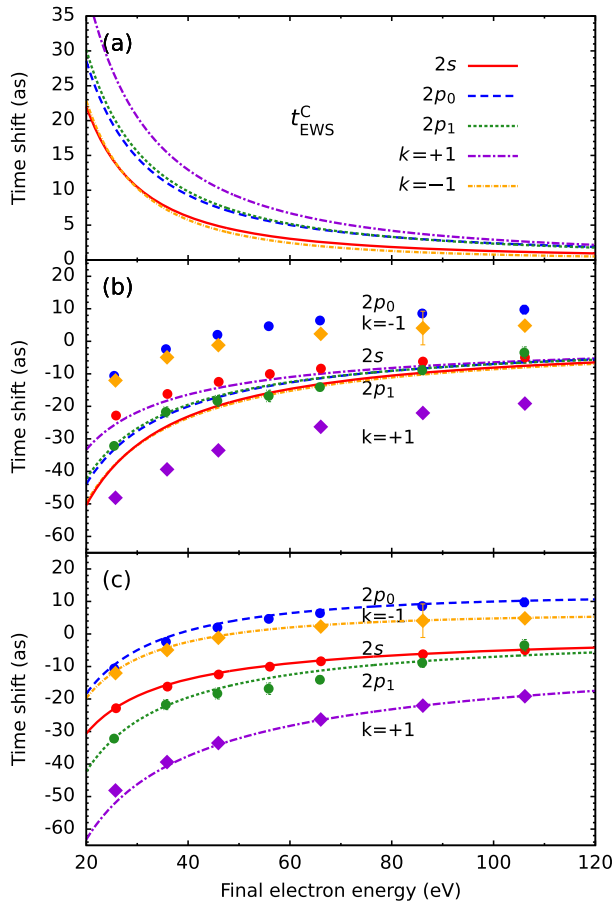


FIG. 10 (color online). Photoionization from different initial states of the  $\text{He}^+(n=2)$  shell as a function of the final kinetic energy  $\epsilon = \omega_{\text{XUV}} + \epsilon_{1s}$  emitted in the forward direction ( $\theta = 0^\circ$ ): (a) Coulomb-EWS times. (b) Corresponding streaking time shifts  $t_S$  for the full quantum simulation (dots) compared with the analytic prediction [Eq. (4.20)] without corrections for initial-state polarization. (c) Same as (b) but compared with the prediction including the dipole-laser coupling [Eq. (4.28)].

and, in turn, to a phase shift

$$\Phi(t) = -\vec{d} \int_{-\infty}^t \vec{F}_{\text{IR}}(t') dt' = \vec{d} \cdot \vec{A}_{\text{IR}}(t). \quad (4.23)$$

This additional phase and energy shift is inherited by the continuum final state giving rise to an additional streaking-measurement related time shift referred to as a dipole-laser coupling (dLC) time shift  $t_{\text{dLC}}$ . Indeed, the streaking time  $t_S$  for the  $\text{He}^+(n=2)$  initial states significantly differs from that predicted by Eq. (4.20) [Fig. 10(b) (Nagele *et al.*, 2011)]. This dLC contribution can be easily accounted for by including the IR field-induced energy shift of the initial state. Equation (4.22) results in an additional modulation of the final-state energy

$$E_f(\tau) = \frac{p_f^2(\tau)}{2} = E_0 - \vec{p}_0 \cdot \vec{A}(\tau) - \vec{d} \cdot \vec{F}_{\text{IR}}(\tau), \quad (4.24)$$

where terms to second order in the streaking field have been neglected. In direct analogy with Eqs. (4.10)–(4.15) the dipole

contribution  $\sim F_{\text{IR}}(\tau)$  being  $\pi/2$  out of phase with the streaking momentum  $\sim A_{\text{IR}}(\tau)$  gives rise to an additional phase shift (Baggesen and Madsen, 2010b) of the streaking momentum for emission along the laser polarization axis,

$$\alpha_{\text{dLC}} A_{\text{IR}}(\tau + t_{\text{dLC}}^{(i)}) = A_{\text{IR}}(\tau) + d_k F_{\text{IR}}(\tau)/p_0, \quad (4.25)$$

with the dLC time shift

$$t_{\text{dLC}}^{(i)} = \frac{1}{\omega_{\text{IR}}} \tan^{-1} \left( -\frac{d_k \omega_{\text{IR}}}{p_0} \right) \quad (4.26)$$

and a renormalization of the amplitude of the streaking momentum

$$\alpha_{\text{dLC}} = \left[ 1 + \left( \frac{d_k \omega_{\text{IR}}}{p_0} \right)^2 \right]^{1/2}. \quad (4.27)$$

Thus, for photoionization of atomic or molecular initial states ( $i$ ) with a permanent electric dipole, the relation between the observable streaking time shift  $t_S$  and the intrinsic EWS time delay  $t_{\text{EWS}}$  [Eq. (4.20)] is modified to

$$t_S = t_{\text{EWS}} + t_{\text{CLC}} + t_{\text{dLC}}^{(i)}. \quad (4.28)$$

Equation (4.28) can account for the time shifts observed for the degenerate hydrogenic manifolds with (sub-)attosecond precision [Fig. 10(c)]. Remarkably, the influence of the dipole-laser coupling is not restricted to initial states with a permanent dipole moment. The strong polarizability of (near) degenerate manifolds also influences substates with well-defined parity for which dipole effects were expected to be absent (Baggesen and Madsen, 2010b; Zhang and Thumm, 2010). Since the states  $2s$  and  $2p_0$  are highly polarizable, they are subject to dLC as well. Expanding  $|2s\rangle$  and  $|2p_0\rangle$  in terms of two parabolic states

$$|n=2, \ell=0 (\ell=1)\rangle = \frac{1}{\sqrt{2}} (|k=1\rangle_{(-)}^+ |k=-1\rangle), \quad (4.29)$$

the effective induced dipole moment follows as

$$\langle d_{\text{eff}}^\ell \rangle = \frac{1}{2|c_\ell|^2} \sum_k d_k |c_k|^2, \quad (4.30)$$

where  $|c_k^2|$  and  $|c_\ell|^2$  are the square moduli of the dipole transition matrix elements [Eq. (2.25)] from the initial state  $k$  or  $\ell$  to the continuum with final momentum along the polarization axis. Using this effective dipole moment in  $t_{\text{dLC}}^{(i)}$ , Eq. (4.26) leads to a drastic change of the predicted time shift [cf. Figs. 10(b) and 10(c)] and to near-perfect agreement with the quantum simulation (Pazourek, Nagele *et al.*, 2012).

## V. TIME-RESOLVED PHOTOIONIZATION OF MANY-ELECTRON ATOMS

Since for hydrogenic atoms and ions or, more generally, for single-active-electron (SAE) models the attosecond streaking

of photoionization can be numerically simulated with (sub-) attosecond precision by solving the Schrödinger equation in its full dimensionality, the extraction of timing information for photoionization now appears well understood. The situation is strikingly different for many-electron atoms. First experiments were performed for rare gas atoms (Schultze *et al.*, 2010; Klünder *et al.*, 2011; Guénot *et al.*, 2012), the results of which have led to a flurry of theoretical investigations (Kheifets and Ivanov, 2010; Schultze *et al.*, 2010; Zhang and Thumm, 2010; Bagesen and Madsen, 2011; Ivanov and Smirnova, 2011; Komninos, Mercouris, and Nicolaides, 2011; Moore *et al.*, 2011; Nagele *et al.*, 2011, 2012, 2014; Dahlström, Carette, and Lindroth, 2012; Dahlström, L’Huillier, and Maquet, 2012; Pazourek, Feist *et al.*, 2012; Pazourek, Nagele *et al.*, 2012; Śpiewanowski and Madsen, 2012; Carette *et al.*, 2013; Dahlström *et al.*, 2013; Dixit, Chakraborty, and Madjet, 2013; Kheifets, 2013; Pazourek, Nagele, and Burgdörfer, 2013; Feist *et al.*, 2014; Saha *et al.*, 2014; Wätzel *et al.*, 2015). Yet satisfactory agreement between theory and experiment is still lacking and many open questions remain.

In the pioneering attosecond streaking experiment (Schultze *et al.*, 2010), the relative delay between photoionization of the neon  $2s$  and  $2p$  electrons  $\Delta t_S(2p - 2s) = t_S(2p) - t_S(2s)$  was found to be  $\Delta t_S(2p - 2s) \approx 21 \pm 5$  as (Fig. 11). The positive sign of the delay implies that the formation of the emitted  $2s$  electron wave packet precedes that of the  $2p$  electron. Obviously, this timing information is unrelated to the arrival time difference at any macroscopic detector as the  $2p$  photoelectron has a considerably higher kinetic energy than the  $2s$  electron and will be arriving first. Accompanying first theoretical investigations (Mercouris, Komninos, and Nicolaides, 2010; Schultze *et al.*, 2010; Yakovlev *et al.*, 2010) confirmed the sign of this delay but found values considerably lower by a factor of 2 to 3. This discrepancy raised conceptual questions as

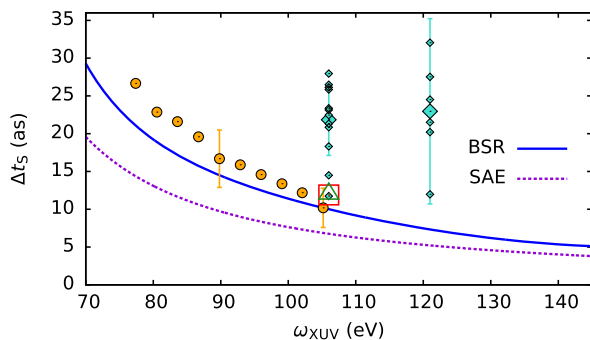


FIG. 11 (color online). Relative streaking time shift  $\Delta t_S = t_S(2p) - t_S(2s)$  between neon  $2p$  and  $2s$  subshells as a function of photon energy  $\omega_{XUV}$ . Comparison between experimental data by Schultze *et al.* (2010), diamonds (both mean value and standard deviation as well as the individual data points as small dots on or near the error bars are shown), and several calculations. Solid line:  $B$ -spline  $R$ -matrix (BSR) method (Feist *et al.*, 2014); solid circles: time-dependent  $R$ -matrix theory (Moore *et al.*, 2011); open square: random phase approximation with exchange (RPAE) (Kheifets, 2013); and open triangle: many-body perturbation theory (MBPT) (Dahlström, Carette, and Lindroth, 2012). For comparison, the SAE mean-field results (dotted line) are also shown (Nagele *et al.*, 2012).

to the influence of many-electron and correlation effects on the intrinsic time delay and on streaking measurement related time shifts. Improvements have been sought along two lines. Within time-independent approximations more accurate calculations of the EWS delay have been performed (Kheifets and Ivanov, 2010; Dahlström, Carette, and Lindroth, 2012; Kheifets, 2013) while the influence of the IR field on the extracted time shift is either neglected or treated only in lowest-order perturbation theory. Within the time-dependent  $R$ -matrix theory (RMT) (Moore *et al.*, 2011), on the other hand, the interaction of the IR field with the fragments of the photoionization process are included to all orders; however, the degree to which correlation effects can be accounted for within a fairly limited basis size remains unclear. A recent calculation (Feist *et al.*, 2014) combines from separate calculations accurate values for  $t_{EWS}$ , obtained using the  $B$ -spline  $R$ -matrix (BSR) method (Zatsarinny, 2006; Zatsarinny and Froese Fischer, 2009), with the nonperturbative evaluation of  $t_{CLC}$  [see Eqs. (4.6), (4.18), and (4.20)]. All up-to-date available calculations that approximately account for electron correlation effects and include the IR-field-induced time shift agree reasonably well with each other (Fig. 11). For comparison, also a TDSE simulation in the SAE approximation (Nagele *et al.*, 2012) for a Ne model potential where the electronic interactions are taken into account only at a mean-field level is shown. Inclusion of correlation effects beyond the mean-field level, indeed, increase the relative EWS delay by  $\sim 4$  as near  $\omega_{XUV} \approx 100$  eV. However, all state-of-the-art calculations for  $\Delta t_S$ , so far, lie far off the experimental values by Schultze *et al.* (2010) and are outside 1 standard deviation of all measured data points (Fig. 11). Adding to the puzzle is the observation that all contributions to photoionization time delays are predicted to decrease with increasing energy while no clear trend is recognizable in the experimental data.

The influence of unresolved shake-up channels was recently identified as one possible source of the discrepancy (Feist *et al.*, 2014). Because the spectral width of the attosecond XUV pulse  $\Delta\omega_{XUV} \sim 2\pi/\tau_{XUV}$  is larger than the spectral separation between the shakeup lines (“correlation satellites”) and the main line, the streaking trace of the  $2s$  main line could be contaminated by spectrally unresolved shakeup channels. Such a contribution might significantly affect the experiment. Indeed, in the experimental data [Fig. 2 of Schultze *et al.* (2010)] a shoulder, most likely due to shakeup, is visible. All previous theoretical treatments have addressed only the  $2s$  and  $2p$  main lines. The potentially strong influence of shakeup channels could result from the prevalence of near-degenerate states in excited-state manifolds of the residual ion. Consequently, the ionic shakeup final state can be strongly polarized by the probing IR pulse (Bagesen and Madsen, 2010b; Pazourek, Feist *et al.*, 2012). Unlike for the ground state discussed earlier an additional time shift due to dipole-laser coupling  $t_{dLC}$  [Eqs. (4.26) and (4.28)] may contribute. Currently available estimates yield, indeed, a correction for the  $2s$  time shift by  $\sim 2$  to 3 as, however, increasing rather than decreasing the discrepancy to the experiment. Future experimental and theoretical studies, in particular, exploring the energy and angular dependence, appear necessary to unravel this puzzle.

Time-resolved photoionization of argon by attosecond XUV pulses is of conceptual interest as it offers the opportunity to explore the influence of so-called Cooper minima

(Cooper, 1962) on the temporal evolution of the outgoing wave packet. Cooper minima result from zeros in the photoionization dipole matrix element [Eq. (2.25)] as a function of the kinetic energy of the outgoing electron. The change of sign of the dipole matrix element near the zero at  $\epsilon = \epsilon_0$  amounts to a phase jump by  $\pm\pi$  over a narrow range of energies (Schoun *et al.*, 2014) and, consequently, to large EWS time shifts [Eq. (2.27)]. These can have either positive or negative sign, depending on whether the phase jump is positive ( $+\pi$ ) or negative ( $-\pi$ ). Photoionization of the Ar  $3p$  electron with one radial node features a Cooper minimum at a photon energy  $\omega_{\text{XUV}} \approx 45$  eV already at the Hartree-Fock (HF) level (Amusia, 1990; Starace, 2006) while strong  $3s - 3p$  intershell correlations are responsible for a deep Cooper minimum in the Ar  $3s$  photoionization cross section near 42 eV (Dahlström, Carette, and Lindroth, 2012; Carette *et al.*, 2013; Dixit, Chakraborty, and Madjet, 2013; Kheifets, 2013; Dahlström and Lindroth, 2014; Saha *et al.*, 2014). These photon energies are within reach of attosecond XUV pulses and have been investigated by combining an APT with an IR field. Time resolution was achieved by RABBIT interferometry (Klünder *et al.*, 2011; Guénot *et al.*, 2012). The harmonic orders 22 to 26 of the Ti:sapphire laser lie in the vicinity of the Cooper minimum of Ar( $3s$ ). Remarkably, both the discrepancies between different calculations and between experimental and theoretical data are large even when the large experimental uncertainty of  $\pm 50$  as is taken into account (note the expanded time scale in Fig. 12 compared to Fig. 11). The origin of these discrepancies is not yet well understood.

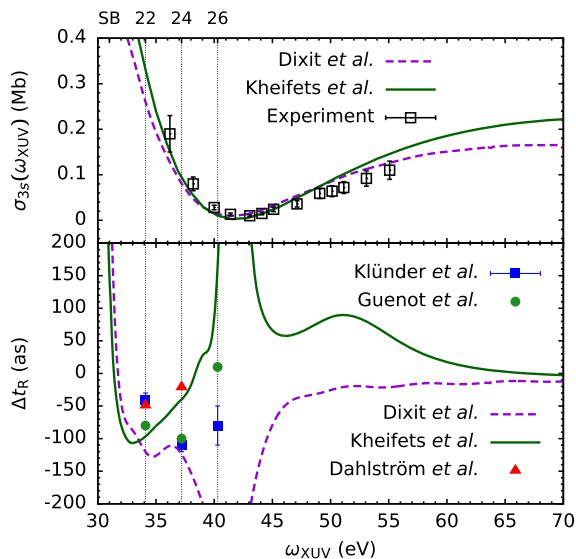


FIG. 12 (color online). (a) Cooper minimum in the Ar( $3s$ ) photoionization: cross section. From Möbus *et al.*, 1993, Dixit, Chakraborty, and Madjet, 2013, and Kheifets, 2013]. (b) Comparison between experiment (Klünder *et al.*, 2011; Guénot *et al.*, 2012) and calculations using RPAE (Kheifets, 2013), time-dependent local density approximation (TDLDA) (Dixit, Chakraborty, and Madjet, 2013), and RPAE (Dahlström and Lindroth, 2014) for the relative RABBIT time delay  $\Delta t_R = t_R(3s) - t_R(3p)$ . For the calculations by Kheifets *et al.* and Dixit *et al.* we added the continuum-continuum coupling according to Eq. (4.21).

They could possibly be connected with the presence of the deep Cooper minimum itself. Since the  $3s$  cross section almost vanishes, small admixtures from otherwise subdominant channels may significantly contribute and amplify discrepancies. For example, one assumption underlying the RABBIT chronoscopy is that only two-photon processes coupling adjacent odd harmonics  $(2n - 1)\omega_{\text{IR}}$  and  $(2n + 1)\omega_{\text{IR}}$  contribute by adding or subtracting one IR photon. Near a Cooper minimum, however, nonperturbative corrections beyond two-photon processes may become more important.

Recently, several measurements of the *relative* time delays between rare gas atoms became available. Guénot *et al.* (2014) reported on relative delays for argon, neon, and helium for photon energies between 31 and 37 eV employing RABBIT with an active stabilization of the interferometer. Sabbar *et al.* (2015) performed streaking measurements of the relative delay between argon and neon in a photon energy region between 28 and 38 eV by using a gas mixture. RABBIT measurements for helium, neon, argon, and krypton over a wider range of energies were also reported by Palatchi *et al.* (2014). Measurements of the relative delays have the potential of higher accuracy as several error sources related to the absolute phase determination drop out. Still, large uncertainties and significant discrepancies between different measurements and between experiment and theory remain.

Photoionization of helium is, presently, the only multi-electron system for which a full *ab initio* quantum simulation of time-resolved photoemission in a streaking setting has become available (Pazourek, Feist *et al.*, 2012). Rigorous tests of the validity of SAE or mean-field approximations are possible for this system. Single photoionization of He( $1s^2$ ) described by an SAE approximation assumes the residual ion to be in the state He $^+(1s)$ . Inclusion of electron-electron interactions alters this picture: The “quasisudden” appearance of the Coulomb hole leads either to a relaxation of the orbital of the second electron to the true ground state of the ion He $^+(1s)$ , sometimes referred to as a “shakedown,” or to a “shakeup” to excited states He $^+(n\ell m)$  or even a “shakeoff” to the continuum. This electronic rearrangement of the residual ionic complex constitutes the prototypical multielectron response to photoionization of a many-electron system and can be studied in detail in He [see, e.g., Sukiasyan, Ishikawa, and Ivanov (2012) for a recent example].

The streaking spectrogram for an XUV pulse with  $\tau_{\text{XUV}} = 200$  as allows one to spectrally resolve the main line [He $^+(1s)$ ] from the shakeup channels [He $^+(n\ell m)$ ,  $n \geq 2$ ]. In general, high-lying shakeup channels are separated from each other by small energies within the spectral line width  $\Delta\omega_{\text{XUV}} \sim 2\pi/\tau_{\text{XUV}}$  and cannot be resolved (see Fig. 13). For the main line, the simulated streaking time shift  $t_S$  (evaluated in the direction of the laser polarization axis) is reproduced by Eq. (4.20) with attosecond accuracy with  $t_{\text{EWS}}$  given by the exact dipole transition matrix element and  $t_{\text{CLC}}$  by Eq. (4.18); see Fig. 14(a). Note that the initial-state polarizability of the helium ground state can be safely neglected as confirmed by the agreement for the main line and, thus,  $t_{\text{dLC}}^{(i)} = 0$  [see Eq. (4.28)]. Moreover, a SAE simulation employing a HF model potential that reproduces the first ionization potential gives nearly identical results for  $t_{\text{EWS}}$  and, in turn, for  $t_S$ .

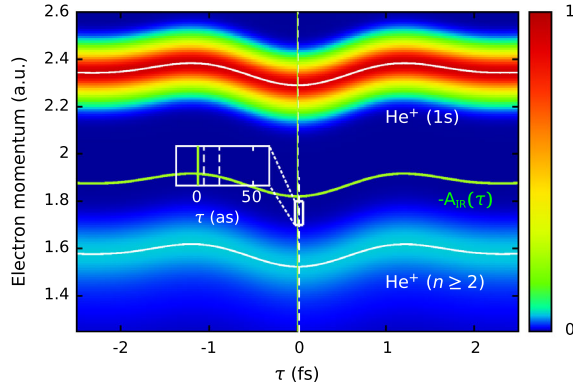


FIG. 13 (color online). Numerically simulated streaking spectrogram for helium and emission into a forward cone (opening angle  $10^\circ$ ) around the polarization axis. XUV pulse with  $\langle \omega_{\text{XUV}} \rangle = 100$  eV,  $\tau_{\text{XUV}} = 200$  as,  $I_{\text{XUV}} = 10^{12}$  W/cm $^2$ , streaking field with  $I_{\text{IR}} = 4 \times 10^{11}$  W/cm $^2$ , and  $\lambda = 800$  nm. Top: Main line  $\text{He}^+(1s)$ , bottom: shakeup satellite (predominantly) to  $\text{He}^+(n = 2)$ .

Therefore, correlation effects do not play a significant role for the direct (main-line) photoionization with  $\text{He}^+(1s)$  as final state.

An entirely different picture emerges for ionization accompanied by shakeup. These correlation-satellite lines represent the prototypical case of photoionization strongly driven by electron-electron interactions of two equivalent electrons (Åberg, 1967; Svensson *et al.*, 1988; Amusia, 1990; Dalgarno and Sadehghpour, 1992; Samson and Stolte, 2002). We restrict in the following the analysis to the dominant shakeup to  $n = 2$ . The spectrogram (Fig. 13) reflects the weakness of the shakeup channel ( $< 5\%$  of the main channel) and indicates the experimental challenge to perform a chronoscopic measurement with attosecond precision. Higher lying channels  $n \geq 3$  are even weaker. Unlike for the ground state  $\text{He}^+(1s)$ , for all substates  $\text{He}^+(n = 2, \ell m)$  Eqs. (4.20) and (4.28) completely fail to reproduce the streaking time shift determined by the *ab initio* simulations [Fig. 14(b)]. In this case, it is the high polarizability of the degenerate hydrogenic  $\text{He}^+(n = 2)$  manifold of the *residual* ion that causes the discrepancy between the extracted streaking time and the prediction Eq. (4.28). The starting point for unraveling these polarization effects is the observation that the two parabolic final states  $\text{He}^+(n = 2, k \pm 1)$  possess a large permanent dipole moment. The long-range interaction between the ionized electron and the residual ion in the exit channel contains now both a Coulombic and a dipolar interaction  $V_d = -\vec{d} \cdot \vec{r} / r^3$ . Their direct contributions to  $t_{\text{EWS}}$  in the absence of a streaking field is fully included in the exact calculation of the dipole transition matrix for single ionization of He employing exterior complex scaling (McCurdy, Baertschy, and Rescigno, 2004; Palacios, Rescigno, and McCurdy, 2008, 2009; Liertzer *et al.*, 2012). In the presence of a streaking field, however, the long-range portions give additional contributions. While the Coulomb contribution is contained in  $t_{\text{CLC}}$  [Eq. (4.18)] the additional streaking-field induced dipolar interaction between the bound and ionized electrons is not. This true field-induced

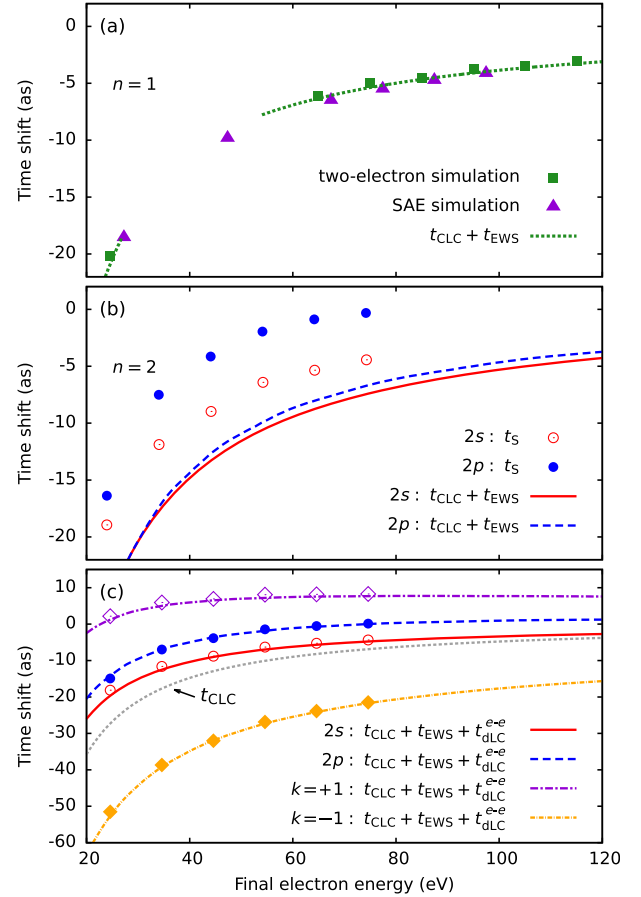


FIG. 14 (color online). *Ab initio* simulation of streaking of photoionization of helium (laser parameters as in Fig. 13). (a) Main line [final state  $\text{He}^+(1s)$ ]. Also shown are the results for the SAE simulation and the predictions Eqs. (4.20) and (4.28). (b) Shakeup to  $n = 2$  final state  $\text{He}^+(n = 2, \ell, m)$ , symbols: *ab initio* simulation, lines: prediction Eqs. (4.20) and (4.28). (c) Same as (b) but with the inclusion of  $t_{\text{dLC}}^{e-e}$  [Eq. (5.1)].

electron-electron interaction effect can be viewed as a dipole-laser coupling, in analogy to Eq. (4.26), however, as a final-state rather than initial-state interaction effect. The analytic derivation for the associated time shift  $t_{\text{dLC}}^{(f)} = t_{\text{dLC}}^{e-e}$  can be directly taken over from that for  $t_{\text{dLC}}^{(i)}$  [Eq. (4.26)], apart from the change of sign relative to the corresponding expression for the initial-state perturbation of the one-electron problem. Accordingly, we have now

$$t_{\text{dLC}}^{(f)} = t_{\text{dLC}}^{e-e} = \frac{1}{\omega_{\text{IR}}} \tan^{-1} \left( \frac{d_k \omega_{\text{IR}}}{p_0} \right), \quad (5.1)$$

and Eq. (4.28) becomes

$$t_{\text{S}} = t_{\text{EWS}} + t_{\text{CLC}} + t_{\text{dLC}}^{(i)} + t_{\text{dLC}}^{(f)}. \quad (5.2)$$

This additional time shift  $t_{\text{dLC}}^{(f)}$  is a true electron-electron interaction contribution absent on the SAE or mean-field level. The physical picture underlying the IR field-induced dipole shift to streaking is illustrated in Fig. 15. The energy modulation of the parabolic states  $k = 1$  and  $k = -1$  are out of

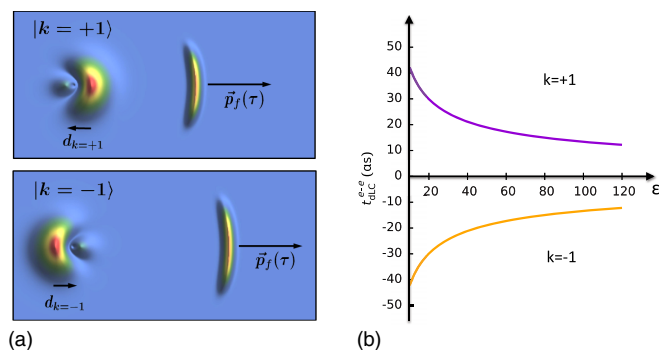


FIG. 15 (color online). Streaking of helium with the remaining ion left in a Stark state: (a) Two-electron dipole-laser interaction in the exit channel; shown is the electron density  $\rho$  of the two-electron state. (b) Resulting dipole-laser induced time shift  $t_{dLC}^{e-e}$  as a function of the final electron energy.

phase by  $\pi$  relative to each other. Adding this additional contribution to the total time shift [Eq. (5.2)] leads to near-perfect agreement for all  $n = 2$  shakeup substates [Fig. 14(c)] confirming, once more, the additivity rule for laser-modified long-range interactions. As in the one-electron case, not only ionic final states with a permanent dipole moment  $|n, k, m\rangle$  but also highly polarizable states in degenerate manifolds with zero static dipole moment  $|n, \ell, m\rangle$  suffer a dipole-laser induced time shift [see Eq. (4.30)]. Conceptually, Eqs. (5.1) and (5.2) reflect the entanglement in the exit channel. As a result, the streaking time shift of the observed ionized electron depends on the dipole moment of the substate of the residual ion. In turn, the final quantum state  $|n, \ell, m\rangle$  or  $|k, n, m\rangle$  becomes accessible in a nondestructive measurement, i.e., without directly observing it.

## VI. TIME-RESOLVED PHOTOIONIZATION OF MOLECULES

Time-resolved photoionization of more complex systems with internal geometric structure promises novel insight into the formation of an outgoing wave packet emerging from the complex. The time encoded in the wave packet of the receding electron carries information on the initial localization within the molecule as well as on the near field of neighboring atomic constituents. The simplest prototypical case is the photoionization of a diatomic molecule (Fernández *et al.*, 2007; Hu, Collins, and Schneider, 2009; Guan, Bartschat, and Schneider, 2011; Bian and Bandrauk, 2012; Ivanov, Kheifets, and Serov, 2012; Serov, Derbov, and Sergeeva, 2013; Carpegiani *et al.*, 2014; Chacon, Lein, and Ruiz, 2014; Ning *et al.*, 2014). Among the fundamental questions to be addressed are the following: Does it take longer for the electron to escape from the multicenter molecular core than from the one-center atomic core? Does the emission time-delay dependence on the relative orientation of the emission direction and molecular axis carry information on the geometric arrangement of the atomic constituents, and, most importantly, are those effects observable in an attosecond streaking setting?

For the simplest and most fundamental one-electron molecule  $H_2^+$ , the validity of the additivity of intrinsic EWS delay and streaking-field-induced time shifts [Eq. (4.28)] for

molecules can be rigorously tested by an *ab initio* solution of the time-dependent Schrödinger equation in the presence of the attosecond XUV and the IR fields. The evolution of the electronic wave packet is calculated for a fixed internuclear distance  $R$  and orientation  $\hat{R}$  relative to the polarization of the laser field. The approximation of frozen nuclei is well justified for attosecond-scale ionization processes. After the conclusion of the pulse, the emerging wave packet is projected onto the molecular scattering states  $\Phi_f^-$  with incoming wave boundary conditions [for details see Hou *et al.* (2012)]. The EWS time delay can be separately determined from the dipole matrix element [cf. Eq. (2.26)]

$$t_{EWS}(\epsilon, R, \theta_e, \theta_x) = \frac{\partial}{\partial \epsilon} \arg [\langle \Psi_f^- (\epsilon, R, \theta_e) | \vec{d} \cdot \hat{e} | \phi_0 \rangle] \quad (6.1)$$

for a vertical Franck-Condon-like electronic transition between Born-Oppenheimer potential surfaces. The dipole matrix element and the EWS time delay depend on the angles of the XUV polarization ( $\theta_x$ ) and the electron emission ( $\theta_e$ ) relative to the orientation of the internuclear axis  $\hat{R}$ . For small internuclear distances  $R = 0.1$  the EWS delay and the resulting streaking delay are indistinguishable on the attosecond scale from those of the united atom limit  $He^+$  [Fig. 16(a)]. At larger internuclear separations [ $R = 2$ , Fig. 16(b)], signatures of the molecular structure become prominently visible. The Coulomb-laser coupling time shift for the  $H_2^+$  molecule is equivalent to the pure Coulombic  $He^+$  case and the additivity of the EWS delay  $t_{EWS}$  and CLC time shift  $t_{CLC}$  [Eq. (4.20)] is satisfied with attosecond precision also for molecules. Note that, in general, the influence of the additional dipole-laser coupling term  $t_{dLC}$  [Eq. (4.28)] is expected to be larger for molecules than for atoms for two reasons: polar molecules possess permanent dipole moments and nonpolar molecules feature larger dipole polarizabilities.

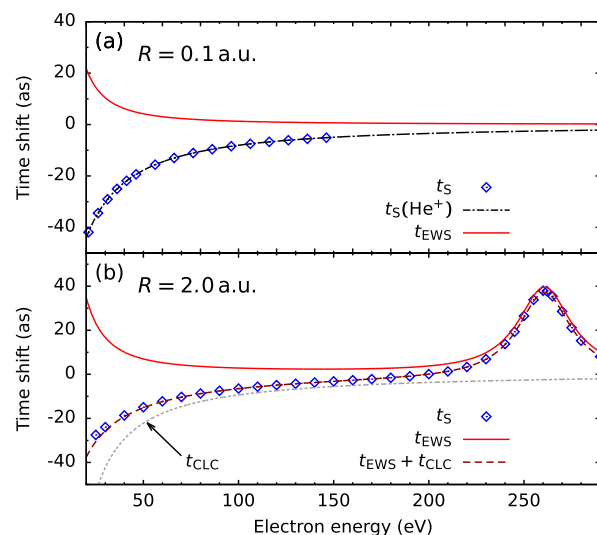


FIG. 16 (color online). EWS (solid lines) and calculated streaking time shifts  $t_S$  (symbols) from  $H_2^+$  at different fixed internuclear distances (Ning *et al.*, 2014). (a)  $R = 0.1$ ; also shown is  $t_S$  for the atomic  $R = 0$  limit,  $He^+$ . (b)  $R = 2$ ; also shown are  $t_{CLC}$  and  $t_{EWS} + t_{CLC}$  [Eq. (4.20)].

The molecular origin of the dramatic enhancement of the time delay near  $E = 260$  eV in Fig. 16(b) can be traced to the two-center or Cohen-Fano interference effect (Cohen and Fano, 1966). Destructive interference between emission from the two centers occurs when the electron momentum  $\vec{p}$  and the internuclear distance vector  $\vec{R}$  satisfy

$$\vec{p} \cdot \vec{R} = pR \cos \theta_e = (2n + 1)\pi. \quad (6.2)$$

Such two-center interference effects could be unambiguously identified in the high-harmonic spectra (Lein *et al.*, 2002; Vozzi *et al.*, 2005, 2006) and contribute to the contrast in holographic imaging of molecular wave functions (Itatani *et al.*, 2004). The estimate [Eq. (6.2)] for the location of the interference minimum is expected to be valid at high electron energies when the outgoing waves can be approximated by plane waves. Indeed, the lines in the  $\cos \theta_e - E$  plane for which the destructive interference  $\sqrt{2ER} \cos \theta_e / 2 = (n + 1/2)\pi$  condition is satisfied approximate the minima in the differential cross section and, in turn, the extrema in  $t_{\text{EWS}}$  quite well (Fig. 17). Note that the destructive interference can give rise to either an enhanced time delay or a time advance. The pronounced peak in the EWS time delay, more precisely in magnitude  $|t_{\text{EWS}}|$ , near the point of destructive Cohen-Fano interferences can be viewed as a molecular analog of the enhancement of  $t_{\text{EWS}}$  near a Cooper minimum (see Sec. V). Indeed, the suppression of the dipole transition by the two-center interference can be in some cases directly associated with zero (or a Cooper minimum) in a single spheroidal partial-wave amplitude of the Coulomb two-center

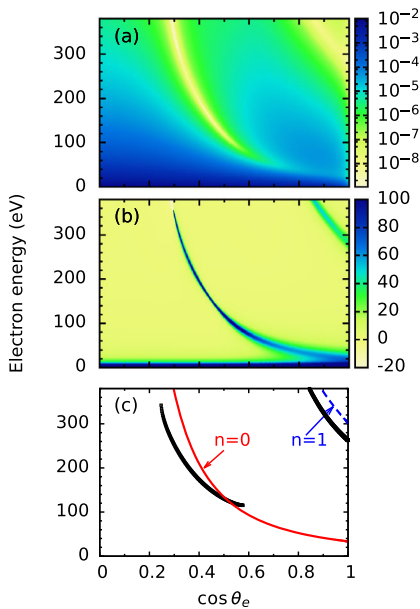


FIG. 17 (color online). Simulations of (a) differential photoemission cross section and (b) EWS time delay in the electron energy ( $\epsilon$ ) and electron emission angle ( $\cos \theta_e$ ) plane for  $\text{H}_2^+$  ( $R = 2$ ) ionized by a 600 as XUV pulse polarized perpendicular to the internuclear axis ( $\theta_x = 90^\circ$ ). (c) Comparison between the location of the cross-section minima and the interference minima predicted by Eq. (6.2).

problem (Ivanov, Kheifets, and Serov, 2012; Serov, Derbov, and Sergeeva, 2013). This structural similarity implies, however, that the experimental observation may face a similar challenge as peaks in the EWS time shift are associated with (near) zero emission probability. The first realistic simulations of an attosecond streaking setting (Ning *et al.*, 2014) indicate that averaging over the radial distribution  $W(R)$  of the molecule to be photoionized

$$\langle t_s \rangle_R = \frac{\int dR t_s(R) W(R) \sigma(R)}{\int dR W(R) \sigma(R)} \quad (6.3)$$

will strongly suppress the interference enhancement of  $t_s$  and  $t_{\text{EWS}}$ . For a vibrational ground-state distribution of  $\text{H}_2^+$   $W_0(R)$  the contribution from  $R$  far away from the interference condition carries a much larger cross section and will overshadow the interference minimum at the equilibrium distance  $R = R_0 = 2$  a.u. thereby rendering the enhancement of  $\langle t_s \rangle_R$  barely visible (Fig. 18). However, since photoionization of  $\text{H}_2^+$  initiates the Coulomb explosion of the ionic fragments (Frasinski *et al.*, 1987; Vager, Naaman, and Kanter, 1989; Chelkowski *et al.*, 1995; Stapelfeldt, Constant, and Corkum, 1995; Staudte *et al.*, 2007), energy-resolved detection of one outgoing proton coincident with the electron allows one to experimentally postselect a narrow  $R$  distribution  $W_\Delta(R)$  within the ground-state vibrational distribution. This additional “knob” allows one to enhance the interference contrast in the time shifts by reducing the vibrational averaging. Coincident detection of a proton near the Coulomb explosion energy corresponding to the equilibrium distance  $E_{\text{kin}} = 1/(2R_0)$  with an energy resolution (FWHM) of 0.5 eV selects a narrow radial distribution  $W_\Delta(R)$  centered at  $R_0$  with a width of  $\Delta R = 0.15$  a.u. The reduced vibrational average [Eq. (6.3)] now yields clearly visible peaks in the EWS and streaking time shifts of the order of 10 as (Fig. 18) as signatures of the destructive interference. The EWS time shift

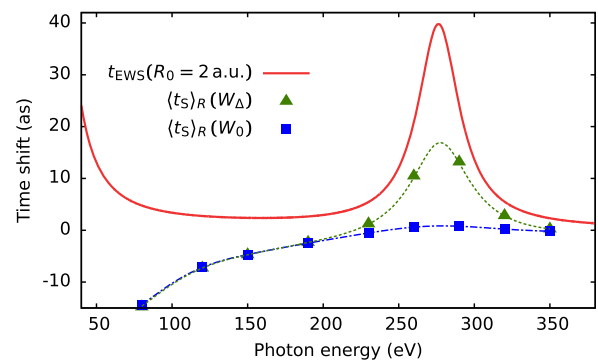


FIG. 18 (color online). Effect of averaging over the distribution  $W(R)$  on the observed streaking shift  $(t_s)_R$ . The EWS delay at the interference minimum  $R_0 = 2$  a.u. (solid line) is compared with the observable streaking delay when averaged over the vibrational ground-state distribution  $W_0$  (squares) or a narrow distribution  $W_\Delta$  (triangles) postselected by Coulomb explosion of the molecular fragments (dashed lines to guide the eye). The XUV-pulse duration in the streaking simulations is  $\tau_{\text{XUV}} = 600$  as (FWHM) and the intensity of the probing 800 nm field is  $I_{\text{IR}} = 10^8$  W/cm<sup>2</sup>. From Ning *et al.*, 2014.

near Cohen-Fano interference minima is found to be not only sensitively dependent on the internuclear distance  $R$  but also on the alignment angle of the molecular axis relative to the ionizing XUV pulse and the IR streaking field (Ning *et al.*, 2014). For its observation, control over the molecular alignment is important. Postselecting the subensemble of molecules with a given orientation of the molecular axis by detecting the Coulomb-exploding fragments provides some level of control. Impulsive or adiabatic laser alignment of the molecules enhances the control and is expected to improve the contrast. The two-center interferences in the molecular high-harmonic generation have been observed employing impulsive alignment, i.e., the revivals of impulsively excited rotational wave packets (Vozi *et al.*, 2005, 2006).

A more complex and challenging case for the interplay between the electronic dynamics and the local geometric and chemical environment is endohedral  $C_{60}$  molecules in which a guest atom with a well-defined core-level emission line resides at the center of the  $C_{60}$  cage, referred to in the following as  $A@C_{60}$  [Fig. 19(a)] (Connerade, Dolmatov, and Manson, 2000; Dolmatov *et al.*, 2004). Timing of the photoelectron emission from the central atom offers now to probe a multitude of environment-specific contributions to the time shift. For outershell electron emission, e.g., the  $3p$  electron of argon, hybridization with the valence electrons of the  $C_{60}$  shell strongly modifies the EWS time delay relative to that of the free atom (Dixit, Chakraborty, and Madjet, 2013). This time shift reflects the initial-state modification of the photoionization matrix element [see Eq. (2.26)]. By contrast, for deeper core levels the initial-state distortion is of minor importance. However, the continuum final state is modified by confinement resonances. Detailed spectroscopic information on confinement resonances for  $Xe@C_{60}$  have recently become available (Dolmatov and Manson, 2008; Kilcoyne *et al.*, 2010). The wavelength of the outgoing electron  $\lambda_D$  may match the resonance condition in terms of the radius of the fullerene shell  $R_0$ ,

$$\lambda_D = \frac{2R_0}{n} \quad (n = 1, 2, \dots), \quad (6.4)$$

giving rise to a modulation of the photoionization cross section (Rüdel *et al.*, 2002) as well as of the EWS time delay

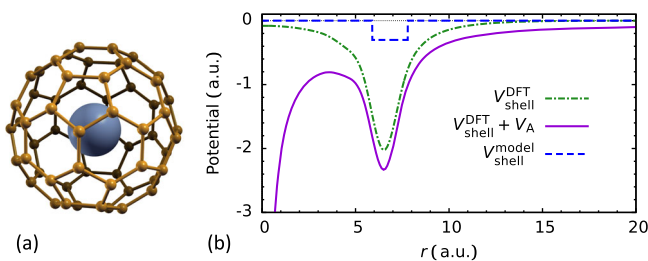


FIG. 19 (color online). Photoionization of an endohedral complex: (a) Endohedral complex  $A@C_{60}$ , schematically. (b) Radial exit-channel potentials experienced by the outgoing photoelectron: (dash-dotted) angular-averaged DFT potential  $V_{\text{shell}}^{\text{DFT}}(r)$ , (dashed) model potential [Eq. (6.5)] with  $V_0 = 0.302$  a.u.,  $\Delta = 1.9$  a.u.,  $R_0 = 5.89$  a.u., (solid)  $V_{\text{shell}}^{\text{DFT}}(r) + V_A(r)$  with the atomic potential for  $\text{He}^+$  for emission of the  $1s$  electron.

(Nagele *et al.*, 2011, 2014; Dixit, Chakraborty, and Madjet, 2013; Pazourek, Nagele, and Burgdörfer, 2013; Deshmukh *et al.*, 2014). These modulations bear close resemblance to the extended x-ray absorption fine structure (EXAFS) (Sayers, Stern, and Lytle, 1971; Stern and Heald, 1983; Ito *et al.*, 2004) by the local crystallographic environment near an absorption site in condensed matter.

The point of departure for a simplified model for timing of photoemission is an effective static potential for the core electron bound to the center atom  $V_A(r)$  with a long-range Coulomb tail. As the outgoing electron traverses the cage, it experiences a short-ranged potential created by the shell of  $C_{60}$  atoms. A simple model potential for the shell is

$$V_{\text{shell}}(r) = \begin{cases} -V_0 & \text{for } R_0 \leq r \leq R_0 + \Delta, \\ 0 & \text{otherwise,} \end{cases} \quad (6.5)$$

with  $R_0$  the inner radius of the  $C_{60}$  shell,  $\Delta$  its width, and  $V_0$  the mean potential on a one-electron level. Typical parameters used are (Dolmatov and Manson, 2008; Dolmatov, King, and Oglesby, 2012)  $V_0 = 0.3$  to  $0.42$ ,  $R_0 = 5.9$  to  $6.0$ , and  $\Delta = 1.25$  to  $1.9$ . A more realistic potential  $V_{\text{shell}}^{\text{DFT}}(r)$  can be determined from density functional theory (DFT) applied to the  $C_{60}$  molecule. After angular averaging, the radial potential  $V_{\text{shell}}^{\text{DFT}}(r)$  differs from Eq. (6.5) by an increased depth and smoothed “edges” of the shell (Wais, 2014; Nagele *et al.*, 2015) [Fig. 19(b)]. Consequently, the amplitude of the oscillation in the photoionization cross section as well as the EWS time shift  $t_{\text{EWS}}(A@C_{60})$  is drastically reduced (Fig. 20). Moreover, the EWS time shift becomes increasingly negative reflecting a time advance caused by the acceleration of the outgoing electron while traversing the strongly attractive potential  $V_{\text{shell}}^{\text{DFT}}(r)$  of the  $C_{60}$  shell.

Such a static potential description cannot fully account for the dynamical response of the many-body system during the photoionization process. The cage will act as a finite-size bath with which the photoelectron interacts. The nonadiabatic

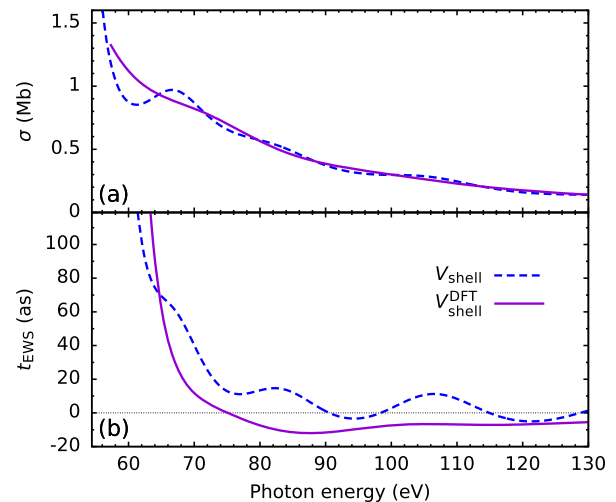


FIG. 20 (color online). Photoionization of the  $1s$  electron of  $\text{He}^+@C_{60}$ , comparison between the model potential  $V_{\text{shell}}(r)$  [Eq. (6.5)] (dashed line) and the DFT potential  $V_{\text{shell}}^{\text{DFT}}(r)$  (solid line): (a) cross section  $\sigma$  and (b) EWS time  $t_{\text{EWS}}$ .

response of the  $C_{60}$  electrons to the quasisudden appearance of a Coulomb hole at the center (Cederbaum and Zobeley, 1999; Breidbach and Cederbaum, 2005) can be viewed as the many-electron generalization of the formation of shakeup or correlation satellites accompanying the photoionization of helium (see Sec. V). Alternatively, it can be viewed as a prototypical case of inelastic scattering of the outgoing photoelectron resulting in collective plasmon as well as particle-hole excitation in the  $C_{60}$  shell. We return to these alternative points of view when discussing time-resolved photoemission from solid surfaces. Both approaches equally predict that electron emission either accompanied by a shakeup excitation of  $C_{60}$  or undergoing an inelastic scattering event in the exit channel is energetically well separated from the “direct” photoelectron emission without concomitant excitation of the residual complex. Therefore, time-resolved photoemission observed by attosecond streaking allows one to disentangle time shifts in photoionization with and without additional energy exchange with the environment (or bath). Even in the absence of simultaneous excitations, the collective response of the valence electrons of the fullerene has a profound effect on attosecond streaking itself. The 240 quasifree valence electrons in the  $C_{60}$  shell feature a high dipole polarizability resulting in an effective screening of the streaking field inside the fullerene and an enhanced streaking near field outside the “polar caps” of the  $C_{60}$  (Fig. 21) (Nagele *et al.*, 2014, 2015). The field distribution calculated from a simple hollow-sphere model for  $C_{60}$  with the same polarizability ( $\alpha \approx 560$  a.u.) as experimentally measured for  $C_{60}$  (Jensen and Van Duijnen, 2005) agrees quite well with a

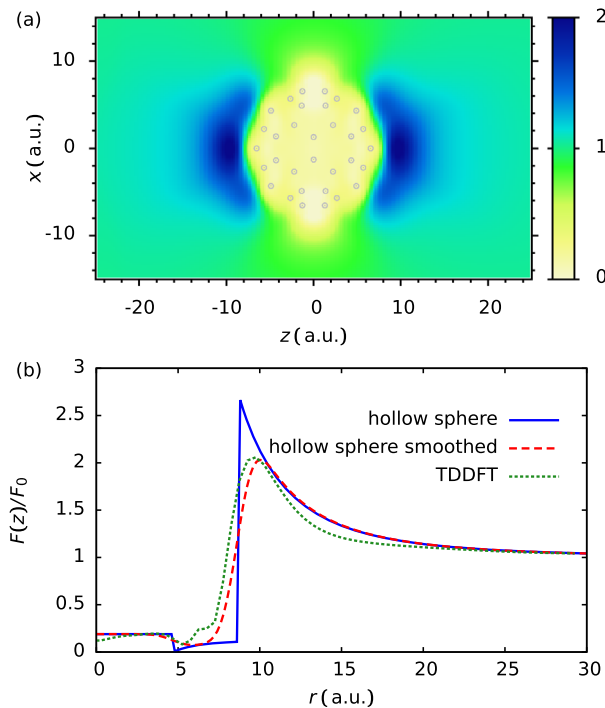


FIG. 21 (color online). Field distribution of the streaking field near  $C_{60}$  (Wachter, 2014; Wais, 2014): (a) Local distribution in the  $x$ - $z$  plane. The positions of the C atoms are indicated by the gray circles. (b) Normalized field distribution along the polar ( $z$ ) axis  $F(z)/F_0$  with  $F_0$  the amplitude of the streaking field.

time-dependent density functional theory (TDDFT) calculation on the adiabatic local density approximation (ALDA) level (Yabana and Bertsch, 1993; Wachter *et al.*, 2014).

The modification of the streaking field due to the dipole response alters the readout of timing information twofold: the photoelectron departing from the central atom is effectively subject to the streaking field only after passing through the  $C_{60}$  shell. Arrival in the streaking field is thus delayed relative to the free atom by the travel time to the surface of the shell. Moreover, while the transport delay time  $t_T \approx (r_0 + \Delta)/v$  is accumulated, the time shift by Coulomb-laser coupling is suppressed for distances from the Coulomb center  $r \leq r_0$ . Both contributions combined lead to an additional time shift  $t_{\text{scr}}$  which depends on the degree of screening by the  $C_{60}$  cage. After leaving the shell, the photoelectron experiences the residual Coulomb-laser coupling and, more importantly, the strong dipole-laser coupling in the locally enhanced dipole-enhanced streaking field. Accordingly, the observed streaking time  $t_S$  for core-level photoemission from a central atom of an endohedral  $C_{60}$  is given by

$$t_S = t_{\text{EWS}}(A@C_{60}) + t_{\text{CLC}} + t_{\text{scr}}(C_{60}) + t_{\text{dLC}}(C_{60}), \quad (6.6)$$

where  $t_{\text{dLC}}(C_{60})$  is the dipole-laser coupling due to the local near field of the polarized fullerene. Remarkably, the large time advance due to the (negative)  $t_{\text{dLC}}$  (Fig. 22) is partially, but not completely, canceled by the (positive) transport delay  $t_T$  which is the dominant contribution to the screening delay  $t_{\text{scr}}(C_{60})$ . The full TDSE simulations for  $t_S$  agree remarkably well with a classical simulation in which  $t_T$ ,  $t_{\text{scr}}(C_{60})$ ,  $t_{\text{CLC}}$ , and  $t_{\text{dLC}}(C_{60})$  can be separately calculated (Wais, 2014). Despite the presence of these large modifications, the modulation of the EWS time delay due to confinement resonances is still visible in the resulting  $t_S$ .

Experimental investigations of streaking of such nanoplasmonic systems promise novel insights into the interplay between chemical environment and the nanoplasmonic response on time-resolved photoemission.

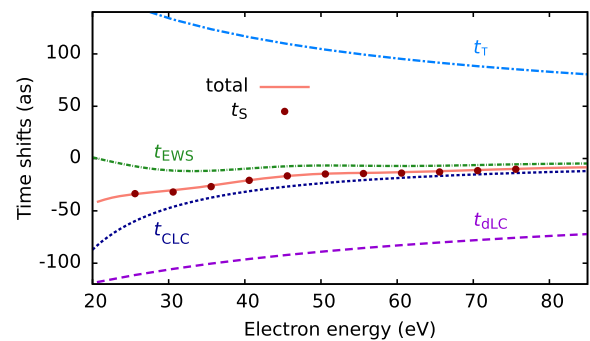


FIG. 22 (color online). Comparison between the streaking time  $t_S$  from the full TDSE solution for  $\text{He}^+(1s)@C_{60}$  photoionization along the laser polarization ( $\theta = 0^\circ$ ) (dots) with the quantum mechanical EWS delay and results from a classical simulation in which the transport time  $t_T$ , the enhanced dipole-laser coupling  $t_{\text{dLC}}(C_{60})$ , and the Coulomb-laser coupling  $t_{\text{CLC}}$  are determined separately.

## VII. TIME-RESOLVED PHOTOEMISSION FROM SURFACES

Time-resolved photoemission from solid surfaces (Föhlisch *et al.*, 2005; Cavalieri *et al.*, 2007) offers a new perspective on electronic dynamics of condensed matter combining attosecond time resolution with angstrom spatial resolution. Since typical inelastic mean free paths (MFP)  $\lambda_i$  for  $\sim 100$  eV electrons are of the order of  $\lambda_i \sim 5$  Å, typical flight times  $\lambda_i/v_g$  ( $v_g$  is the group velocity of the emitted electron) are of the order of  $\sim 100$  as. Time-resolved photoemission thus probes not only the electronic structure in the topmost layers but also allows one to probe the electronic response and electron transport on its natural time scale. Extracting and interpreting the time information for such a complex many-body system remains, however, a challenge.

The pioneering attosecond streaking experiment by Cavalieri *et al.* (2007) employing XUV pulses with energies  $\langle \omega_{\text{XUV}} \rangle = 91$  eV and a linewidth of  $\Delta \omega_{\text{XUV}} = 6$  eV revealed a time delay for the emission of  $4f$  core levels relative to conduction band (CB) electrons from the W(110) surface of  $\Delta t_S(4f - \text{CB}) \approx 110 \pm 70$  as. This finding stimulated a large number of theoretical studies (Kazansky and Echenique, 2009; Lemell *et al.*, 2009; Zhang and Thumm, 2009, 2010, 2011a, 2011b, 2011c; Krasovskii *et al.*, 2010; Krasovskii, 2011; Borisov *et al.*, 2013). Additional measurements at somewhat higher XUV energies  $\langle \omega_{\text{XUV}} \rangle = 106$  and 120 eV yielded considerably smaller time delays of  $\Delta t_S(4f - \text{CB}) \approx 30$  as with smaller error bars (Neppl, 2012). The origin of this delay as well as its strong variation with energy has remained a widely open question. An additional piece of the puzzle was provided by measurements of the delay between the  $2p$  core and the conduction band of a magnesium (0001) surface,  $\Delta t_S(2p - \text{CB})$ . For this nearly free electron metal, the delay was found to be near zero to within the experimental uncertainty  $\Delta t_S(2p - \text{CB}) \approx 5 \pm 20$  as (Neppl *et al.*, 2012). This finding contradicts the notion (Kazansky and Echenique, 2009; Zhang and Thumm, 2009, 2011c) that the different degrees of localization of the electronic states of the conduction band and/or core levels would cause large delays but could be simply explained by the equality of mean travel times to the surface of conduction band and core electrons in Mg (Neppl *et al.*, 2012),

$$\frac{\lambda_{\text{CB}}}{v_g(\text{CB})} \approx \frac{\lambda_{2p}}{v_g(2p)}, \quad (7.1)$$

where  $\lambda$  and  $v_g$  denote the inelastic MFP and the group velocity for conduction band and core electrons, respectively. This explanation relies on a classical transport model (Cavalieri *et al.*, 2007; Lemell *et al.*, 2009; Liao and Thumm, 2014) for electron emission from the solid. Calculation and interpretation of the observed time delays raise important conceptual questions about photoionization from such extended many-electron systems (Heinzmann, 2013) for time-integral photoemission.

The starting point of a quantum description of photoemission in lowest-order perturbation theory in the ionizing XUV field is the so-called “one-step” or multiple-scattering model

(Mahan, 1970; Feibelman and Eastman, 1974) which is equivalent to the  $S$ -matrix formulation [discussed in Sec. II and Eq. (2.6)]. Accordingly, the response of the solid to the photoabsorption is represented by a coherent superposition of a set of stationary states of the channel Hamiltonian of the  $(N-1)$ -electron system and a wave packet of Dyson orbitals  $|\Phi_{ej}\rangle$  of the emitted electron emerging from the entangled  $N$ -electron wave packet with components [Eq. (2.6)]

$$|\Phi_{ejs}\rangle \xrightarrow[t \rightarrow \infty]{} \hat{A} (|\Phi_s^{(N-1)}\rangle \otimes |\Phi_{ej}\rangle), \quad (7.2)$$

where  $\hat{A}$  denotes the antisymmetrization operator. The one-electron wave function  $|\Phi_{ej}\rangle$  corresponds to so-called “low-energy electron diffraction” (LEED) scattering states subject to incoming boundary conditions (Feibelman and Eastman, 1974). The formal simplicity of this description within the framework of an  $S$ -matrix (or, equivalently,  $T$ -matrix) theory belies the fact that the set of accessible final states  $|\Phi_s^{(N-1)}\rangle$  is large and includes a plethora of complex dynamical processes. Moreover, in standard photoemission spectroscopy, the degrees of freedom associated with the residual ionic complex remain unobserved and are traced out [Eq. (2.13)]. The one-electron photoelectron spectrum  $P_{ej}$  thus includes a multitude of many-body effects (Echenique *et al.*, 1981; Zhang and Thumm, 2011b) such as core-hole screening (Canright, 1988; Huber *et al.*, 2001) and relaxation, as well as particle-hole, and plasmon excitation. To identify and disentangle those processes, a simplified “three-step model” (or “multistep model”) of photoemission (Feibelman and Eastman, 1974) is frequently employed in which the response of the full many-body state  $|\Psi_s^{(N-1)}\rangle$  is reduced to few active degrees of freedom with which the outgoing photoelectron interacts. Accordingly, the photoemission process by an XUV photon is broken down into a sequence of separate elementary processes (Fig. 23): (1) the primary photoabsorption transferring a localized core electron or valence band electron to a high-lying state in the conduction band, (2) the transport of this Bloch wave packet toward the surface undergoing electron-electron collisions which may lead to additional particle-hole and collective plasmon excitations, and (3) diffraction at the surface potential and eventual transmission into the vacuum leaving the solid with asymptotic momentum  $\vec{k}$ . Underlying such semiclassical multistep models is the implicit assumption of partial loss of coherence due to dephasing in the presence of a large number of traced out environmental degrees of freedom. Such multistep models suggest time ordering of those elementary processes. It is therefore tempting to inquire into the possibility to observe in real time the unfolding of such a multistep scenario by attosecond streaking.

One key feature of attosecond streaking for condensed-matter systems is that the streaking field clocks the time the electron arrives in the IR field. Similar to the case of  $C_{60}$  (see Sec. VI), the crucial input is penetration depth and dielectric screening of the IR field with angstrom accuracy. In the first theoretical models (Cavalieri *et al.*, 2007; Kazansky and Echenique, 2009; Lemell *et al.*, 2009; Zhang and Thumm, 2009) a wide variety of penetration models have been used. For an accurate determination of the spatiotemporal profile of

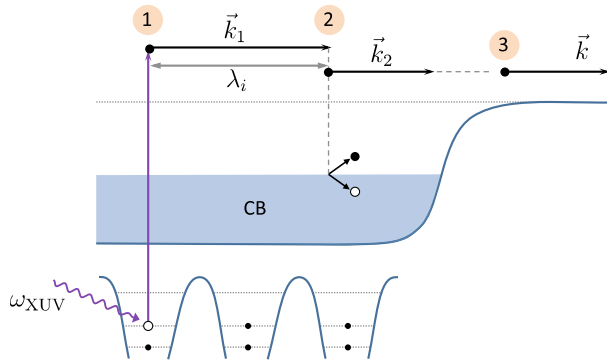


FIG. 23 (color online). Multistep model of photoemission by an XUV pulse from surfaces: 1: primary transition from a core level to a high-lying continuum level assuming the spectator electrons remain frozen, 2: transport of a Bloch wave packet toward the surface accompanied by electron-electron collisions leaving a particle-hole excitation, and 3: ejection of the photoelectron into vacuum with asymptotic momentum  $k$ .

the near-field IR field at the metal-vacuum interface on the angstrom scale, the commonly used Fresnel equations based on macroscopic material properties and perfectly sharp interfaces cannot be applied. A microscopic description for  $F_{\text{IR}}(z, t)$  is provided by TDDFT (Runge and Gross, 1984; Liebsch, 1997; Wachter *et al.*, 2012). The streaking field with the polarization oriented along the surface normal  $\hat{z}$  induces a polarization charge layer at the metal surface which shields the interior of the solid against the external electric field. Screening at metallic surfaces becomes effective near the so-called image plane  $z_{\text{im}}$  typically located outside the topmost atomic layer at  $z_{\text{atom}} = 0$  (Fig. 24). A further characteristic distance for the electronic response is the so-called “jellium” edge at  $z_0 = z_{\text{atom}} + d/2$  ( $d$  is the layer spacing for a given crystallographic direction). In general, the location

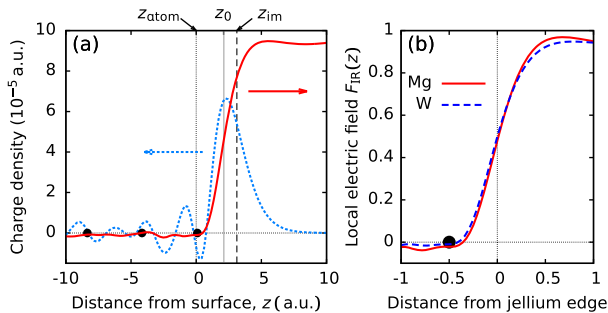


FIG. 24 (color online). TDDFT analysis of the atomic-scale dipole screening of the streaking field normal to the surface plane. (a) Snapshot of the streaked field  $F_{\text{IR}}(z)$  and of the charge density near a W(110) surface taken at the maximum of the streaking field with intensity  $2 \times 10^{11}$  W/cm<sup>2</sup> and duration 4 fs (FWHM of intensity, cosine-pulse shape). The jellium edge is half a lattice spacing  $z_0$  outside of the first layer,  $z_{\text{im}}$  marks the (dynamical) image plane (dashed vertical line; centroid of the induced density) located even farther out from the first layer. (b) Snapshot of the local electric field calculated from time-dependent density functional theory simulations for different surfaces, W(110) (dashed) and Mg(0001) (solid), plotted relative to the jellium edge. The local field distribution is virtually unaffected by the surface composition.

and width of the dynamic screening charge layer are expected to depend on the strength, direction, and frequency of the applied field as well as on the lattice structure of the target. Remarkably, the local screening of the streaking field at IR frequencies  $\omega = \omega_{\text{IR}}$  as predicted by TDDFT (Neppel *et al.*, 2015) is almost identical for pure W, pure Mg, and W/Mg heterostructures with varying numbers of Mg adlayers when plotted relative to the position of the jellium edge. The key observation is that the laser field is already fully screened at the position of the atoms of the topmost layer. Thus, the primary XUV photoabsorption and the formation of the Bloch wave packet takes place fully screened from the streaking field in close analogy to the core-level emission of an endohedral C<sub>60</sub> molecule (Sec. VI). Only upon crossing the metal-vacuum interface is the photoelectron exposed to the streaking field. Its turn-on is localized to within the width of the dynamical screening charge distribution, typically  $\lesssim 1$  Å (Fig. 24) and, thus, fairly abrupt (Neppel *et al.*, 2015).

We illustrate the potential of time-resolved photoemission for providing novel conceptual insights with the help of one example. For XUV energies, photoelectron spectra  $P(\epsilon)$  map out the density of states (DOS) of the electronic band structure. The spectral width of attosecond XUV pulses  $\Delta\omega_{\text{XUV}}$  can be comparable to the width of the conduction band. Time-resolved photoemission is, thus, characterized by a significant spectral broadening of the photoelectron spectrum  $P(\epsilon = \omega_{\text{XUV}} - \epsilon_i)$ . If now the spectral width is still smaller than the spacing to so-called satellite peaks at lower energies, e.g.,  $P(\epsilon - \omega_{p,s})$ , the plasmon-loss peaks displaced by  $\omega_p$  ( $\omega_s$ ), the energy of the bulk (or surface) plasmon excitation, relative timing information on the emission of the main line, and the satellite lines become accessible. One of the still widely open issues is to what extent these satellite features are intrinsic or extrinsic (Aryasetiawan, Hedin, and Karlsson, 1996; Guzzo *et al.*, 2014). The notion of plasmon excitation, intrinsically linked to the photoemission, can be viewed as the direct condensed-matter analog to the atomic shakeup correlation satellites (Sec. V). Extrinsic plasmon generation, on the other hand, is thought to proceed by secondary inelastic electron scattering of the outgoing photoelectron subsequent to the primary photoexcitation and is often treated as a background contribution to the spectrum. Clearly, within a one-step description such a distinction is anything but clear-cut: these processes simply represent different coherent superpositions of the ionic final states of the  $(N-1)$ -electron system,  $|\Psi^{(N-1)}\rangle = \sum a_s^{(N-1)} |\Phi_s^{(N-1)}\rangle$ . By contrast, within the multistep model intrinsic plasmon excitation is linked to the vertical transition to the continuum (step 1 in the multistep model, Fig. 23) while extrinsic plasmon excitation results from inelastic scattering (step 2, Fig. 23). Such a semiclassical model suggests that extrinsic and intrinsic plasmon satellites should feature a distinct time ordering. A classical transport simulation (Lemell *et al.*, 2009; Lemell, Tókési, and Burgdörfer, 2012) within which ingredients of the multistep model are naturally incorporated suggests that such delays are, indeed, on the attosecond scale and, thus, accessible by attosecond streaking.

We consider the photoemission from the Mg conduction band following the absorption of an XUV photon with

$\langle\omega_{\text{XUV}}\rangle = 130$  eV. The direct conduction band spectrum  $P(\epsilon)$  extends in the range  $120 \leq \epsilon \leq 126$  eV broadened by the Fourier width of the attosecond pulse  $\tau_{\text{XUV}} = 450$  as,  $\Delta\omega_{\text{XUV}} = 4$  eV. The plasmon satellite line associated with the excitation of a single bulk plasmon is displaced by 10.5 eV and thus well separated from both the direct conduction band spectrum and the Mg(2*p*) core level near  $\epsilon = 80$  eV. The extraction of time delays from a classical transport simulation (Lemell *et al.*, 2009) employs the correspondence to temporal shifts of the first moment of the “wave packet” [Eq. (2.33)] represented here by classical phase space distribution. Plasmon excitation along classical trajectories is treated in terms of a stochastic force whose strength and temporal structure are determined by the optical limit of the energy loss function  $\text{Im}[-1/\epsilon(\omega)]$  (Palik, 1998). The observed streaking time delay between the plasmon satellite line relative to the direct conduction band line (Fig. 25),  $\Delta t_{\text{S}} = 55$  as, is consistent with the additional travel time through the excess escape depth  $\Delta x_i = \lambda_i/2$  resulting from the convolution of two escape-probability distributions (Lemell *et al.*, 2015) with equal escape depth of  $\lambda_i \approx 5$  Å near  $\epsilon = 120$  eV (Tanuma, Powell, and Penn, 2011). This prediction for the streaking time delay applies to the limit of a purely extrinsic plasmon excitation during transport. Predictions of the time delay for the opposite limit of a purely intrinsic, shakeup-like plasmon excitation for Mg are not yet available. Extrapolating its order of magnitude from the EWS time delay calculated for atomic many-electron systems (see Sec. V) we expect such a delay to be much smaller and of the order of  $\sim 10$  as. The first experimental streaking data indicate a significant time delay of the plasmon satellite line compared to the main line allowing the relative ratio of intrinsic to extrinsic plasmon generation  $\approx 0.1$  to be extracted with unprecedented accuracy (Lemell *et al.*, 2015). Thus, attosecond streaking holds the promise to disentangle extrinsic from intrinsic plasmon satellites in photoemission spectra and, on a more fundamental level, to scrutinize the validity of such a multistep description of photoemission from condensed matter. Furthermore, attosecond chronoscopy also offers opportunities to probe the many-electron response in photoemission

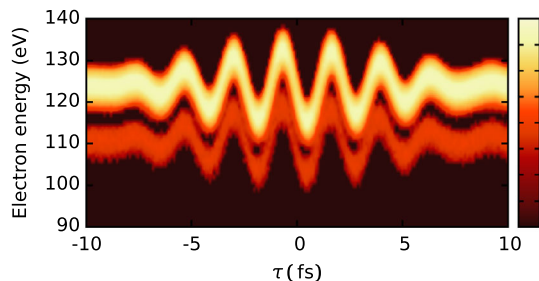


FIG. 25 (color online). Simulation of a streaking spectrogram for photoemission of Mg(0001) following photoabsorption by an XUV photon with  $\langle\omega_{\text{XUV}}\rangle = 130$  eV and  $\Delta\omega_{\text{XUV}} = 3$  eV, streaked by an IR field ( $\lambda_{\text{IR}} = 800$  nm,  $I_{\text{IR}} = 4 \times 10^{11}$  W/cm<sup>2</sup>). The plasmon correlation satellite (pl) of the CB line is well separated from the main CB line with a relative streaking delay  $\Delta t_{\text{S}} = t_{\text{S}}(\text{pl} + \text{CB}) - t_{\text{S}}(\text{CB}) = 55$  as [for details see Lemell *et al.* (2015)].

from strongly correlated systems (Lee, 2012, 2013) in unprecedented detail.

## VIII. TIME ORDERING IN TWO-PHOTON DOUBLE IONIZATION

The idea of probing the time ordering within a sequence of elementary processes of a many-body system by time-resolved photoemission suggested above for photoemission from solid surfaces can be put to a rigorous test in multiphoton ionization of atoms. Going beyond the elementary photoelectric effect in this section, we consider now ionization by the absorption of two XUV photons rather than one. We are thus exploring time information characterizing the *nonlinear* atomic response. Still, such processes remain in the regime of lowest-order perturbation theory and represent weak field-atom interactions.

A prototypical case is the two-photon double ionization (TPDI) of helium. A strongly simplified picture (Fig. 26) suggests that the helium atom absorbs two photons each of which ejects one electron. In the energy domain and for long XUV pulses, it has become customary to distinguish the so-called sequential (S) regime for  $\hbar\omega_{\text{XUV}} > I_2 = 54.4$  eV from the nonsequential (NS) regime for  $(I_1 + I_2)/2 = 39.5 \leq \hbar\omega_{\text{XUV}} \leq 54.4$  eV, where  $I_1$  and  $I_2$  are the first and second ionization potentials of helium, respectively. Sequential means in this context that the two ionization events are independent of each other, i.e., correlations between the two ionized electrons in the exit channel can be neglected and no energy sharing is required to reach the asymptotic final state. Equivalently, the intermediate state in this two-step process is a (quasi)stationary on-shell state of the singly charged helium [ $\text{He}^+(n\ell m)$ ]. The borderline between the sequential and the nonsequential regime is given by the binding energy  $I_2$  of the most deeply bound electron of the system  $\text{He}^+(1s)$ . For photon energies above  $I_2$  each electron can be ejected by one photon independent of the proximity to and energy sharing with the other electron. Signatures of the sequential and nonsequential character in the energy dependence of the double ionization rate and in the energy sharing and angular correlations of the emitted electrons have been the focus of a large number of theoretical [see, e.g., Laulan and Bachau (2003), Ishikawa and Midorikawa (2005), Horner *et al.* (2007), Nikolopoulos and Lambropoulos (2007),

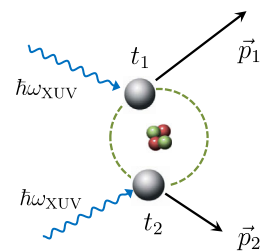


FIG. 26 (color online). Two-photon double ionization of helium, schematically. Two photons from a moderately strong XUV pulse ( $I_{\text{XUV}} \sim 10^{15}$  W/cm<sup>2</sup>) with duration  $\tau_{\text{XUV}} \lesssim 1$  fs are absorbed and eject two electrons with momenta  $\vec{p}_i$  ( $i = 1, 2$ ). Time-resolved photoemission allows one to interrogate the timing  $t_{1,2}$  of the two absorption (ejection) events.

Feist *et al.* (2008), Feist, Pazourek *et al.* (2009), Palacios, Rescigno, and McCurdy (2009), Fomouo *et al.* (2010), Nepstad, Birkeland, and Førre (2010), and Pazourek *et al.* (2011) and references therein] and experimental (Nabekawa *et al.*, 2005; Sorokin *et al.*, 2007; Antoine *et al.*, 2008; Rudenko *et al.*, 2008; Kurka *et al.*, 2010) studies. However, the direct observation of the timing of the ionization steps implied by the notion of (non)sequentiality has not yet been achieved.

For ultrashort pulses with  $\tau_{\text{XUV}}$  in the few-hundred attosecond regime and spectral width of  $\Delta\omega_{\text{XUV}} \sim 2\pi/\tau_{\text{XUV}}$  of several eV the distinction between sequential and nonsequential ionization becomes blurred. The TPDI is now influenced by strong spatiotemporal correlation of the two-electron wave packet irrespective of whether the mean frequency  $\langle\omega_{\text{XUV}}\rangle$  of the pulse is below or above the threshold. Real-time observation of TPDI monitored by streaking allows one to inquire into the sequentiality of the emission process and into the time interval between the two emission events. Moreover, time-resolved TPDI opens up the opportunity to explore the time ordering underlying time-dependent quantum dynamics as an accessible physical observable.

To lowest nonvanishing order perturbation theory, TPDI is given by the second-order transition matrix element [cf. Eq. (2.1)]:

$$a_{i \rightarrow f}^{(2)} = - \int_{-\infty}^{\infty} dt_1 \int_{-\infty}^{t_1} dt_2 \langle \psi_f | V_I(t_1) V_I(t_2) | \psi_i \rangle \quad (8.1)$$

between the initial state  $|\psi_i\rangle$ , taken in the following to be the fully correlated He ground state, and the final state  $|\Psi_f\rangle = |\Psi(\vec{p}_1, \vec{p}_2)\rangle$  of two continuum electrons with asymptotic momenta  $\vec{p}_1$  and  $\vec{p}_2$  and energy  $E_{\text{tot}} = \sum_i p_i^2/2$ . The perturbation operator [see Eq. (2.3)] is given in the interaction representation and in length gauge by

$$V_I(t) = e^{iH_0 t} \sum_{i=1}^2 \vec{r}_i \cdot \vec{F}_{\text{XUV}}(t) e^{-iH_0 t}, \quad (8.2)$$

where  $\vec{F}_{\text{XUV}}(t) = F_0 \exp(-\ln 4t^2/\tau_{\text{XUV}}^2) \cos(\omega_{\text{XUV}} t) \hat{z}$  is the linearly polarized attosecond XUV pulse. Second-order perturbation theory [Eq. (8.1)] has explicitly built in time ordering  $t_1 > t_2$ . The formation of the intermediate wave packet  $\sim V_I(t_2) |\Psi_i\rangle$  by the single action of the perturbation on the initial state causing the ejection of the first electron precedes that of the ejection of the second electron  $\sim V_I(t_1) V_I(t_2) |\psi_i\rangle$  forming a two-electron wave packet which contains a component that eventually converges toward TPDI as  $t \rightarrow \infty$ . The following question is then posed: Is such a temporal sequence of events as implied by time-ordered perturbation theory physically observable even though Eq. (8.1) represents a coherent superposition of all event sequences without an intervening projective measurement of the intermediate state?

A fully nonperturbative treatment of this process by solving the two-electron Schrödinger equation in the presence of both the ionizing XUV and the streaking IR field in its full dimensionality has become available (Pazourek, Nagele, and Burgdörfer, 2015). Second-order perturbation theory is,

however, a useful guide for analyzing and interpreting the numerical results.

We consider TPDI by an ultrashort XUV pulse with  $\tau_{\text{XUV}} = 500$  as and mean photon energy  $\langle\omega_{\text{XUV}}\rangle = 100$  eV. For a long pulse, this energy would be clearly in the spectroscopically independent “sequential” regime. For an ultrashort pulse, such a designation is anything but clear-cut. After  $\sim \tau_{\text{XUV}}/2$  even a “fast” electron has reached a distance of only  $\approx 20$  a.u. from the core when the second electron is about to take off. Thus, electron-electron interactions in the exit channel cannot be neglected. The joint energy distribution for double ionization (DI)  $P(E_1, E_2)$  features two distinct peaks [Fig. 27(a)] near the energies  $E_{1,2} = \langle\omega_{\text{XUV}}\rangle - I_{1,2}$  for uncorrelated ionization the widths of which are governed by the Fourier width of the pulse but are also influenced by correlation effects as first discussed by Ishikawa and Midorikawa (2005). We note that at low energies ( $E_{1,2} \leq 20$  eV) the joint energy distribution displays the contribution from one-photon double ionization (OPDI) for photon energies above the double ionization threshold  $\langle\omega_{\text{XUV}}\rangle \gtrsim 80$  eV. The OPDI and TPDI spectra are energetically well separated from each other and can independently be analyzed without the risk of contamination. We concentrate in the following on the information contained in the TPDI signal. We note, however, that time-resolved OPDI has also been recently investigated. Emmanouilidou, Staudte, and Corkum (2010), Price, Staudte, and Emmanouilidou (2011), and Price *et al.* (2012) proposed a classical two-electron streaking model and first timing measurements employing the RABBIT technique have been reported for the OPDI of xenon (Månsson *et al.*, 2014). The TPDI streaking spectrogram [Fig. 27(b)] provides a clear example for the simultaneous observation for the “absolute” time shift of each electron relative to the time zero, the time of the peak of the ionizing field  $F_{\text{XUV}}(t)$ ,  $t_a = 0$  [Eq. (2.31)], as well as the relative emission time delay  $\Delta t_{\text{S}}^{\text{DI}}$  between the two electrons. The interelectronic delay is in this case so large (of the order of

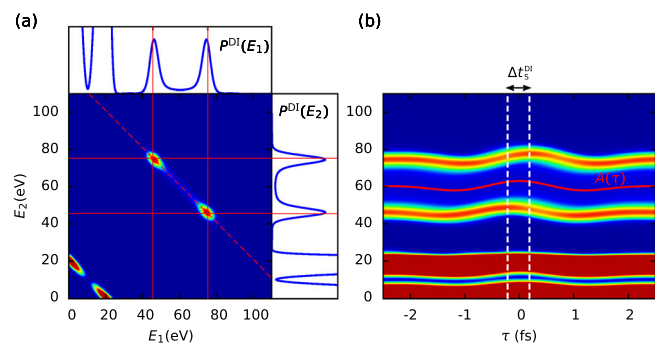


FIG. 27 (color online). Simulation of two-photon double ionization of helium: (a) Joint two-electron energy distribution  $P^{\text{DI}}(E_1, E_2)$  for TPDI with  $\langle\omega_{\text{XUV}}\rangle = 100$  eV and a pulse duration  $\tau_{\text{XUV}}$  of 500 as, emission back to back along the polarization direction ( $\theta_1 = 0^\circ$ ,  $\theta_2 = 180^\circ$ ). The panels above and on the right show the singly differential energy distribution  $P^{\text{DI}}(\epsilon)$  after tracing out the energy of the second electron. (b) Streaking spectrogram from the integrated spectra  $P^{\text{DI}}(\epsilon)$  in (a) at different delay times  $\tau$  between the ionizing XUV pulse and the probing IR field ( $\lambda_{\text{IR}} = 800$  nm,  $I_{\text{IR}} = 4 \times 10^{11}$  W/cm<sup>2</sup>, sine-squared envelope with a total duration of 6 fs).

$\sim 100$  as) that it becomes directly visible in the spectrogram without the need for a sophisticated retrieval algorithm. Extraction of the relevant dynamical timing information of the two-electron wave packet is more challenging than for single electron emission in view of the multidimensional nature of the final state. Moreover, properties of the atomic response and of the ionizing pulse become intertwined due to the nonlinearity of the two-photon process. In analogy to the photoelectric effect [Eq. (2.1)], EWS-type delays can be determined for TPDI. However, their extraction in terms of a spectral derivative of the argument of a transition matrix element Eq. (2.26) is not directly applicable. Moreover, their physical significance remains to be explored.

The EWS delay for the electron 1 with energy  $E_1$ , a fixed energy of the second electron and fixed emission angles  $\theta_1$  and  $\theta_2$  can be extracted numerically from

$$t_{\text{EWS},1}^{\text{DI}}(E_1|E_2, \theta_1, \theta_2) = \frac{\partial}{\partial E_1} [\arg a^{\text{DI}}(E_1, E_2, \theta_1, \theta_2, t_f) + E_1 t_f]_{E_1=E_1}, \quad (8.3)$$

where  $a^{\text{DI}}$  is the double ionization amplitude calculated by solving the TDSE for TPDI by the XUV pulse in the absence of the probing IR field. In Eq. (8.3) the propagation phase of a free reference electron  $-E_1 t_f$  at the same energy is subtracted. Equation (8.3) describes the one-electron group delay relative to the arrival time of the XUV field ( $t_a = 0$ ). From these absolute one-electron delays  $t_{\text{EWS},j}^{\text{DI}}$  ( $i = 1, 2$ ) collective two-electron time delays can be deduced: the relative emission delay

$$\Delta t_{\text{EWS}}^{\text{DI}}(\Delta E) = t_{\text{EWS},1}^{\text{DI}}(E_1|E_2, \theta_1, \theta_2) - t_{\text{EWS},2}^{\text{DI}}(E_2|E_1, \theta_1, \theta_2) \quad (8.4)$$

and the joint two-electron emission time delay

$$T_{\text{EWS}}^{\text{DI}}(E_{\text{tot}}) = \frac{1}{2}[t_{\text{EWS},1}^{\text{DI}}(E_1|E_2, \theta_1, \theta_2) + t_{\text{EWS},2}^{\text{DI}}(E_2|E_1, \theta_1, \theta_2)], \quad (8.5)$$

which are functions of the energy sharing  $\Delta E = E_1 - E_2$  between the two liberated electrons and their total energy  $E_{\text{tot}} = 2\omega_{\text{XUV}} - I_1 - I_2$ . Delays [Eqs. (8.3)–(8.5)] for this two-photon process are implicitly also functions of the temporal and spectral properties of the ionizing XUV pulse (Pazourek, Nagele, and Burgdörfer, 2015). For example, when the ionizing XUV pulse features a chirp (i.e., a nonlinear phase variation with time) not only the absolute time delays can be modified as is the case in one-electron ionization (see Sec. II.B) but also time ordering of the TPDI itself can be altered (Lee, Pindzola, and Robicheaux, 2009). The simulations presented in the following pertain to a chirp-free XUV pulse.

The relative emission delay  $\Delta t_{\text{EWS}}^{\text{DI}}(\Delta E)$  allows a direct comparison (Fig. 28) with the intuitive “classical” relative delay  $\langle \Delta t \rangle_{\text{uc}}$  predicted for two uncorrelated (uc) and statistically independent emission events each of which with a probability density proportional to the intensity of the XUV pulse  $I(t)$ , Eq. (2.31),

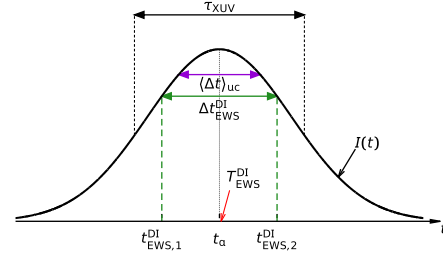


FIG. 28 (color online). Illustration of time observables for two-electron emission in TPDI, schematically. The emission times of the first  $t_{\text{EWS},1}^{\text{DI}}$  and second electron  $t_{\text{EWS},2}^{\text{DI}}$  are measured relative to the arrival time (peak)  $t_a$  of the envelope of the attosecond XUV pulse ( $t_a = 0$  in the following) with temporal FWHM (in intensity)  $\tau_{\text{XUV}}$ . The relative emission delay between the two electrons is given by  $\Delta t_{\text{EWS}}^{\text{DI}} = t_{\text{EWS},1}^{\text{DI}} - t_{\text{EWS},2}^{\text{DI}}$ . Also shown is the estimate of the relative emission delay predicted for stochastic uncorrelated (uc) emission events  $\Delta t_{\text{uc}}$  and the joint emission time of the two-electron wave packet  $T_{\text{EWS}}^{\text{DI}}$ .

$$\langle \Delta t \rangle_{\text{uc}} = \tau_{\text{XUV}} / \sqrt{\pi \ln 4} \approx 0.479 \tau_{\text{XUV}}. \quad (8.6)$$

Such linear scaling with the pulse duration is expected for any *on-shell* two-photon process [see, e.g., Su, Ni, Jaroń-Becker, and Becker (2014) for two-photon single ionization]. The exact emission delay  $t_{\text{EWS}}^{\text{DI}}(\Delta E = I_2 - I_1)$ , evaluated in coplanar geometry ( $\phi_1 = \phi_2 = 0$ ) at the energy difference  $\Delta E = I_2 - I_1$ , corresponding to sequential ionization with the ionic ground state  $\text{He}^+(1s)$  as the on-shell intermediate state and for back-to-back emission ( $\theta_1 = 0^\circ, \theta = 180^\circ$ ), becomes as large as 350 as exceeding the uncorrelated estimate by more than 100 as (Fig. 29). This, at first glance, surprising finding suggests an intuitive interpretation: in order to suppress energy sharing between the electrons in the exit channel and to approach the well-defined energy of the sequential intermediate state as closely as possible consistent with the Heisenberg uncertainty principle, the two emission events have to be temporarily as well separated as possible within the confines of the pulse duration  $\tau_{\text{XUV}}$ . The relative emission delay is, thus, a strongly varying function of the energy sharing. For example, near  $\Delta E = 0$ , where the electrons symmetrically share the energy in the exit channel,  $\Delta t_{\text{EWS}}^{\text{DI}}$  is reduced by 2 orders of magnitude to a few attoseconds. In this limit, the two electrons must take off nearly simultaneously for the electron-electron interaction in the exit channel to be efficient in redistributing the energy delivered by the photons. In this regime, the emission process is strongly nonsequential even though the photon energy  $\langle \omega_{\text{XUV}} \rangle \approx 100$  eV lies in the spectroscopically sequential regime ( $> 54.4$  eV). It should be noted that for the pulse duration of  $\tau_{\text{XUV}} \approx 500$  as the probability for emission  $p^{\text{DI}}(E_1, E_2)$  near equal energy sharing is small [see Fig. 27(a)] since the Fourier width of the pulse  $\Delta \omega_{\text{XUV}}$  is smaller than the required energy sharing  $|I_2 - I_1|$ .

Attosecond streaking allows one to observe this relative emission delay in real time. Extracting  $\Delta t_{\text{EWS}}^{\text{DI}}$  from the streaking spectrogram [Fig. 27(b)] requires a generalization of the mapping [Eqs. (4.3) and (4.28)] between streaking times  $t_s$ , extracted from the fit of the modulation

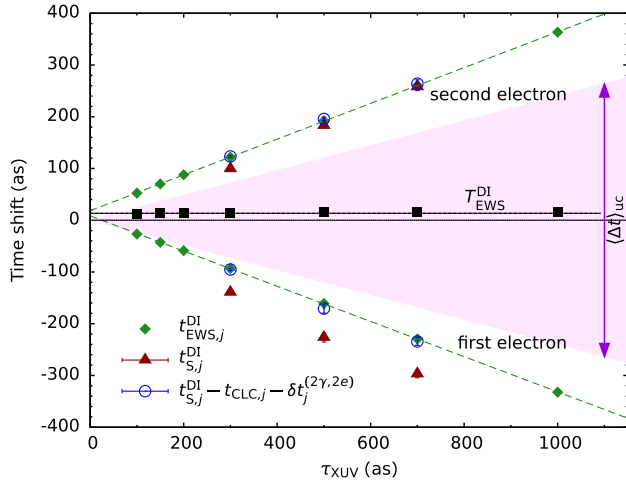


FIG. 29 (color online). TPDI time shifts as a function of the pulse duration  $\tau_{XUV}$  for  $\langle\omega_{XUV}\rangle = 80$  eV and back-to-back emission of the two electrons ( $\theta_1 = 0^\circ$ ,  $\theta_2 = 180^\circ$ ). Streaking time shifts  $t_S^{DI}$  are extracted from a streaking spectrum as in Fig. 27 for  $I_{IR} = 10^{10}$  W/cm $^2$  and  $\lambda_{IR} = 800$  nm. Also shown is the comparison between the intrinsic EWS delays  $t_{EWS,j}^{DI}$  ( $j = 1, 2$ ) and the corresponding streaking delay  $t_{S,j}^{DI}$  corrected for the Coulomb-laser-coupling contribution  $t_{CLC,j}$  and the two-photon correction for the noninteracting reference system [Eq. (8.7)]. The dashed line indicates the approximately linear scaling of  $t_{EWS,j}^{DI}$  with the pulse duration  $\tau_{XUV}$ . The shaded area indicates the uncorrelated mean escape delay  $(\Delta t)_{uc}$  [Eq. (8.6)]. The joint two-electron emission time  $T_{EWS}^{DI}(E_{tot})$  [Eq. (8.5)] is shown by the squares.

$\Delta p(t) = -A(t + t_S)$ , and the intrinsic atomic time delay  $t_{EWS}$  valid for the photoelectric effect. For two-photon absorption an additional streaking-field-induced correction to the time shift  $\delta t_j^{(2\gamma, 2e)}$  arises (Pazourek, Nagele, and Burgdörfer, 2015) which can be determined from the shape function  $\mathcal{G}$  in second-order perturbation theory (Palacios, Rescigno, and McCurdy, 2009). Accordingly, the streaking time shift of the  $j$ th electron  $t_{S,j}^{DI}$  ( $j = 1, 2$ ) observed in TPDI of the fully Coulomb-interacting system reads

$$t_{S,j}^{DI} = t_{EWS,j}^{DI} + t_{CLC,j} + \delta t_j^{(2\gamma, 2e)}, \quad (8.7)$$

where  $t_{CLC,j}$  is the Coulomb-laser coupling correction of the  $j$ th electron. The accuracy of this relation is demonstrated for a wide range of XUV energies and pulse durations (Fig. 29). Equation (8.7) can be tested by determining  $t_{S,j}^{DI}$  on the left-hand side from the *ab initio* TDSE simulation in the presence of the IR streaking field and  $t_{EWS,j}^{DI}$  on the right-hand side by an independent TDSE calculation in the absence of the IR field.  $t_{CLC}$  [Eq. (4.18)] and  $\delta t_j^{(2\gamma, 2e)}$  (Pazourek, Nagele, and Burgdörfer, 2015) are known analytically or numerically. The good agreement on the  $\sim 10$  as level illustrates that two-electron EWS delays are also accessible through attosecond streaking with remarkable precision. This example illustrates the fact that the spatiotemporal correlation of a two-electron wave packet can be observed in time-resolved two-photon emission. Moreover, the pulse duration  $\tau_{XUV}$  can serve as a knob to actively control correlations in the continuum (Feist,

Nagele *et al.*, 2009). With decreasing  $\tau_{XUV}$ , the relative time delay becomes shorter (Fig. 29) enhancing the temporal correlation and “nonsequentiality” of the emission process. Moreover, this example underlines the fact that the notion of time ordering underlying time-dependent perturbation theory and the multistep models for photoemission from complex targets becomes accessible by streaking without destroying the coherence of the underlying time evolution. With the rapid progress in the development of more intense attosecond XUV pulses, experimental exploration of time-resolved two-photon ionization should soon come into reach.

## IX. ATTOSECOND STREAKING OF TUNNELING TIME?

Ever since the discovery of quantum tunneling of particles through potential barriers the question of whether tunneling is instantaneous or takes a finite time has been a matter of debate (MacColl, 1932). Viewed as a temporal evolution of a wave packet, the speed with which tunneling through the barrier proceeds has been the subject of a large number of theoretical investigations. Even the possibility of superluminal speeds for the traversal through the barrier have been discussed, referred to as the Hartman effect (Hartman, 1962). Accounts of this debate can be found in a large number of reviews (Hauge and Støvneng, 1989; Landauer and Martin, 1994; de Carvalho and Nussenzveig, 2002; Olkhovsky, Recami, and Jakiel, 2004; Winful, 2006; Muga, Mayato, and Egusquiza, 2007; Choi and Jordan, 2013). As a well-defined operator whose eigenvalue corresponds to the travel time through the classically forbidden region could not be identified, unconventional operational descriptions have been put forward, such as complex travel time based on a Feynman path integral formulation (Sokolovski, Brouard, and Connor, 1994) or contextual values replacing conventional eigenvalues of a self-adjointed operators for so-called weak measurements (Choi and Jordan, 2013). Closely related is the notion of a Larmor clock (Baz’, 1967a, 1967b; Büttiker, 1983) which yields, in general, two different precession times which can be interpreted in special cases as the real and imaginary parts of a complex time (Sokolovski, Brouard, and Connor, 1994). The Larmor clock exploiting the expectation value of the spin projection as a “hand” can be viewed as a realization of a quantum clock (Landauer and Martin, 1994). For scattering at potential barriers a consensus appears to have emerged on two complementary, yet consistent, characteristic times: the dwell time  $t_D$  of the wave packet in the scattering region and the EWS time  $t_{EWS}$  [Eqs. (2.22) and (2.24)], in this context often referred to as the asymptotic phase time or group delay of the wave packet. The dwell time is related to the expectation value  $\langle P_D \rangle_t$  of the Hermitian projection operator

$$P_D = \int_{(\text{scattering region})} d^3r |\vec{r}\rangle \langle \vec{r}|, \quad (9.1)$$

where the integration extends over a finite scattering region and is, at least in principle, an experimental observable. The dwell time provides intrinsically local information on where the wave packet spends its time but is not directly associated with an observable of a specific asymptotic scattering channel.

By contrast, the EWS time is unambiguously linked to a specific scattering channel while providing no local timing information on the motion of the wave packet in the scattering region. These two complementary times are related to each other and, in special cases, e.g., for well-isolated resonances, they agree with each other,

$$t_D = t_{\text{EWS}}, \quad (9.2)$$

(Smith, 1960; de Carvalho and Nussenzveig, 2002; Winful, 2006) and correspond in this case to the lifetime of the resonance  $t_{\text{res}}$ .

The question of tunneling times naturally resurfaced in attosecond chronoscopy for strong-field ionization by ultrashort and intense IR pulses (Uiberacker *et al.*, 2007; Eckle, Pfeiffer *et al.*, 2008; Eckle, Smolarski *et al.*, 2008; Shafir *et al.*, 2012; McDonald *et al.*, 2013; Landsman *et al.*, 2014; Orlando *et al.*, 2014; Landsman and Keller, 2015). Following the semiclassical analysis by Keldysh (1965), an atomic electron is emitted by tunneling through the potential barrier formed by the atomic Coulomb potential and the (quasi)static electric field of the IR pulse (Keldysh, 1965; Ammosov, Delone, and Krainov, 1986). For small Keldysh parameters  $\gamma \ll 1$  which we write as  $\gamma = 4\pi t_K/T_{\text{IR}}$ , where  $t_K$  is the Keldysh tunneling time,

$$t_K = \frac{R}{v_T}, \quad (9.3)$$

tunneling is the dominant ionization mechanism. In Eq. (9.3)  $R$  is the radial position of the tunnel exit ( $R \approx |e_i|/F_0$  for short-ranged binding potentials) and  $v_T$  is the (imaginary) speed of the electron traveling inside the barrier. For its magnitude  $v_T$ , the characteristic speed of the electronic initial bound state in the Coulomb field according to the virial theorem  $|v_T| = \sqrt{2|e_i|}$  is used here. Tunneling processes beyond the simple Keldysh picture have been identified for molecules which originate from the multicenter character of the binding potential [for a review, see Bandrauk and Légaré (2012)]. For example, differences in the timing of tunneling ionization originating from different force centers or different molecular orbitals have been explored (Takemoto and Becker, 2010; Bian and Bandrauk, 2012).

Applying the tunneling time concepts discussed for scattering at potential barriers to tunneling ionization is not straightforward since strong-field ionization is, just as photoionization, a half-scattering process with the initial state being a bound state. Consequently, the initial state does not satisfy incoming scattering boundary conditions and the splitting of a wave packet into a transmitted and a reflected part is not well defined. More importantly, the potential barrier to be penetrated by tunneling, unlike for potential scattering, is strongly time dependent, either appearing or disappearing every half period  $T_{\text{IR}}/2$  (for a linearly polarized IR field) or rotating in space with frequency  $\omega_{\text{IR}}$  (for a circularly polarized field). Therefore, an alternative view of the Keldysh time [Eq. (9.3)] is that of a characteristic response time to the time-dependent strong IR field within which the initial wave function of the bound electron builds up an outgoing flux component (Orlando *et al.*, 2014) rather than that of the time it takes a

wave packet to travel through a stationary tunneling barrier. In this context, the Keldysh time can be identified as the strong-field version of the Mandelstam-Tamm time (Mandelstam and Tamm, 1945). As pointed out by Dahlström, L’Huillier, and Maquet (2012) a difficulty in measuring the tunneling time by attosecond streaking by the attoclock (Eckle, Pfeiffer *et al.*, 2008; Eckle, Smolarski *et al.*, 2008; Landsman *et al.*, 2014) originates from self-referencing: the IR field that causes the (tunneling) ionization to be clocked acts also as the clock. Consequently, variation of parameters that control either the ionization process or the clock independently of each other is difficult to realize. Disentangling the information on the timing of the ionization process from that on the ionization dynamics itself is, thus, a challenge.

In order to inquire into the opportunities to determine characteristic times related to tunneling by attosecond streaking, we briefly discuss an alternative scenario (Fig. 30) more closely related to the theme of attosecond time-resolved photoemission that circumvents many of the conceptual difficulties mentioned previously. We consider a transition from a deeply bound atomiclike state in a Yukawa potential [see Eq. (2.36)] to a resonant state in the continuum confined by a radial and stationary potential barrier of height  $V_0$  and thickness  $\Delta$  (“shape resonance”). The attosecond XUV pulse which drives the transition provides a well-defined start signal at  $t_a = 0$ . The shape resonance subsequently decays by tunneling through the barrier and the emitted electron in the continuum will be streaked, i.e., “clocked” by the IR field. The IR field is taken to be sufficiently weak as to avoid any unwanted IR field-induced tunneling (or multiphoton) ionization and to isolate tunneling through the stationary barrier as the only relevant pathway toward ionization. The stationarity of the barrier bypasses the influence of the dynamical response associated with the Mandelstam-Tamm time. The following question is then posed: what temporal information on the decay dynamics does the observed streaking time shift  $t_S$  relative to the arrival time of the peak of the XUV pulse contain?

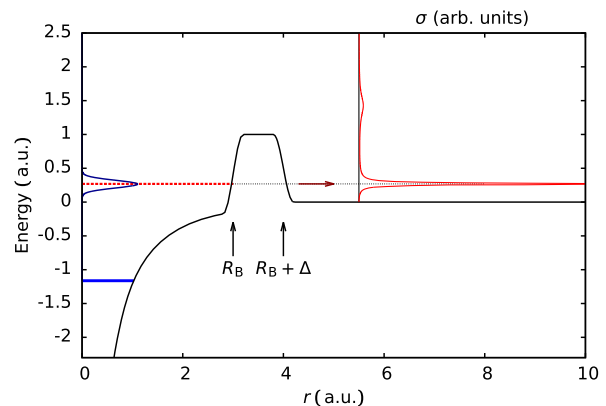


FIG. 30 (color online). Model for the excitation of a  $\ell = 1$  shape resonance induced by a barrier of width  $\Delta$  and height  $V_0 = 1$  a.u. superimposed on a short-ranged Yukawa-type potential  $V_Y(r) = -Z_{\text{eff}}/r e^{-r/a}$  [see Eq. (2.36)] with  $Z_{\text{eff}} = 2$  and  $a = 2$  from the ground state at  $e_{1s} = -1.16$  a.u. by an attosecond XUV pulse with  $\tau_{\text{XUV}} = 500$  as and  $\Delta\omega_{\text{XUV}} = 3.7$  eV. Upper right corner: photoionization cross section near the resonance  $E_R = 0.2686$  a.u. with width  $\Gamma = 0.0134$  a.u.

For attosecond streaking to operate in the regime of a classical clock (see Sec. IV.A) the lifetime of the decaying resonance  $t_{\text{res}}$  must be short compared to the optical cycle time  $T_{\text{IR}}$ . Accordingly, we focus on tunneling in the “thin barrier” regime (Hartman, 1962). Moreover, for optimal time resolution of the decay process, the exciting XUV pulse should be short compared to  $t_{\text{res}}$ , i.e., we use

$$\tau_{\text{XUV}} \ll t_{\text{res}} \ll T_{\text{IR}}. \quad (9.4)$$

Equation (9.4) translates into the spectral domain as

$$\omega_{\text{IR}} \ll \Gamma \ll \Delta\omega_{\text{XUV}}. \quad (9.5)$$

In addition, the spectral width  $\Delta\omega_{\text{XUV}}$  must be small compared to the barrier height  $V_0$ ,  $\Delta\omega_{\text{XUV}} \ll V_0$ , in order to prevent direct overbarrier ionization by the XUV pulse. Equations (9.4) and (9.5) can be fulfilled for streaking fields in the midinfrared ( $\lambda_{\text{IR}} = 5 \mu\text{m}$  in the present simulation) and an XUV pulse with  $\langle\omega_{\text{XUV}}\rangle = 39 \text{ eV}$  and  $\tau_{\text{XUV}} = 500 \text{ as}$  (Fig. 31). Such a scenario with suitable parameters for a spherical barrier enclosing a Yukawa-like central potential of height  $V_0 = 1 \text{ a.u.}$  extending from  $R_B = 3 \text{ a.u.}$  to  $R_B + \Delta = 4 \text{ a.u.}$  is shown in Fig. 30. This potential landscape features a single resonance in the  $p$  sector ( $\ell = 1$ ) with complex energy  $E_{\text{res}} = 0.2686 \text{ a.u.}$  and  $\Gamma = 0.0134 \text{ a.u.}$ , determined by exterior complex scaling (ECS). The corresponding lifetime of the shape resonance is  $t_{\text{res}} = 903 \text{ as}$ . We note that this potential landscape bears some similarity to the endohedral

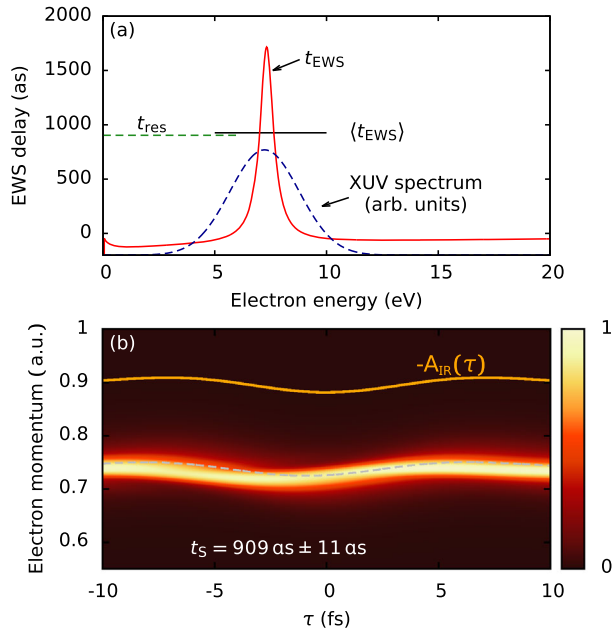


FIG. 31 (color online). Time delays of a shape resonance: (a) Energy-dependent EWS delay  $t_{\text{EWS}}$  and mean  $\langle t_{\text{EWS}} \rangle$  averaged over the spectral profile of the XUV pulse (dashed) for photoexcitation of the resonance at  $E_{\text{R}} = 0.2686 \text{ a.u.}$  with width  $\Gamma = 0.0134 \text{ a.u.}$  by an XUV pulse with  $\langle\omega_{\text{XUV}}\rangle = 39 \text{ eV}$  and  $\tau_{\text{XUV}} = 500 \text{ as}$ . (b) Streaking of resonance by an IR field with  $\lambda_{\text{IR}} = 5 \mu\text{m}$  and  $I_{\text{IR}} = 10^{10} \text{ W/cm}^2$  resulting in a streaking time shift of  $t_{\text{S}} = 909 \pm 11 \text{ as}$ .

$\text{C}_{60}$  (see Sec. VI). The most significant difference is that the attractive well provided by the  $\text{C}_{60}$  shell is replaced by a repulsive barrier. We emphasize, however, that we are not aware of any molecular realization of such a landscape.

A full 3D TDSE simulation for the attosecond streaking of the excitation and delay by tunneling (Fig. 31) yields  $t_{\text{S}} = 909 \text{ as}$  and to a remarkably good degree of approximation ( $\lesssim 1\%$ ),

$$t_{\text{S}} \approx t_{\text{res}}, \quad (9.6)$$

where  $t_{\text{S}}$  is numerically determined from the streaking trace generated by the solution of the TDSE and  $t_{\text{res}}$  is independently determined from the ECS method applied to the stationary Schrödinger equation. Thus, the streaking time shift provides direct and accurate information on the lifetime of the resonance. Furthermore, Eq. (9.6) agrees with the mean EWS delay  $\langle t_{\text{EWS}} \rangle$  for the photoexcitation of the resonance averaged over the spectral width [Fig. 31(a)]  $t_{\text{S}} \approx \langle t_{\text{EWS}} \rangle \approx 926 \text{ as}$  to within  $\approx 5\%$ . This value furthermore agrees with the dwell time  $t_{\text{D}}$  of the continuum wave packet (with angular momentum  $\ell = 1$ ) within the scattering region restricting the projection Eq. (9.1) to  $0 \leq r \leq R_B + \Delta$  (see Fig. 30). The equality of  $t_{\text{EWS}}$  and  $t_{\text{D}}$  [Eq. (9.2)], well known for scattering (Smith, 1960; de Carvalho and Nussenzveig, 2002; Winful, 2006), therefore applies also to the half-scattering scenario of photoemission. In the present context, one important consequence is that the experimentally observable streaking time shift does not provide any specific and separate information on the tunneling process itself, i.e., is unrelated to the transit time through the barrier but is identical to the dwell time inside the scattering region. Clearly, if a well-defined separate tunneling time were to exist, it would be included in the overall lifetime  $t_{\text{res}}$ .

It is now tempting to perform a numerical “gedanken experiment” in which we alter the streaking scenario such that more specific information on the transit time through the barrier rather than through the entire scattering region is probed. To this end, we first assume, inspired by the streaking simulations for  $\text{C}_{60}$ , that the outer surface of the spherical barrier at  $R_B + \Delta$  is metallic and provides perfect screening inside neglecting, however, any near-field enhancement. For otherwise identical parameters we find now an enhanced streaking delay

$$t_{\text{S}}(R_B + \Delta) = t_{\text{res}} + t_{\text{T}} = 1039 \text{ as}. \quad (9.7)$$

The additional contribution of  $t_{\text{T}} = 130 \text{ as}$  agrees to within  $\leq 1\%$  with the transport time  $t_{\text{T}} = (R_B + \Delta) / \sqrt{2\epsilon_f} = 131 \text{ as}$  for the electron traveling with the velocity  $\sqrt{2\epsilon_f}$  (corresponding to the energy  $\epsilon_f$ ) from its starting position  $\langle r \rangle_i = 0$  after photoexcitation to the outer rim of the potential well. The close analogy to  $t_{\text{T}}$  for the endohedral complex [Eq. (6.5)] is remarkable considering that we have replaced the attractive well by a potential barrier. The point to be noted is that the transport time  $t_{\text{T}}$  includes both the time the wave packet spends inside the classically allowed and the forbidden region until it reaches the streaking field. Following up on this observation we perform in the second step an analogous

simulation assuming now that the perfect screening occurs at the inner rather than the outer rim. For this scenario we find

$$t_S(R_B) = t_{\text{res}} + t'_T = 1006 \text{ as.} \quad (9.8)$$

Consequently, the difference between the two streaking times

$$t_S(R_B + \Delta) - t_S(R_B) = t_T - t'_T = 33 \text{ as} \quad (9.9)$$

can be interpreted as the transport time through the classically forbidden region of the barrier. Alternatively, Eq. (9.9) can be viewed as an estimate for the dwell time inside the barrier. We emphasize that these two quantities are not equivalent as the dwell time records both the transmitted and reflected portions of the wave packet while the transit time refers to the arrival in the streaking field, i.e., transmission. Equation (9.9) agrees to a remarkable degree of approximation with a Keldysh-like “tunneling time” for the transit through the barrier Eq. (9.3):

$$t_T - t'_T = \frac{\Delta}{v_T} = t_K \quad (9.10)$$

evaluated, however, for the (real) final state velocity of the electron in the continuum  $v_T = \sqrt{2e_f}$ . If such a scenario would be realizable, Eqs. (9.8) and Eq. (9.9) would constitute a protocol for extracting tunneling times in terms of a transit time of the wave packet through the barrier. It also would provide an estimate, most likely a lower bound, for the dwell time inside the barrier determined by restricting the projection operator [Eq. (9.1)] to the classically forbidden region.

It should be emphasized, however, that the perfect screening without accompanying near-field enhancement as assumed in this gedanken experiment has, to our knowledge, no immediate correspondence to a realistic physical system. It may serve only to illustrate the principle of extracting local dwell time information by attosecond streaking. It complements the well-defined time information for asymptotic scattering states in terms of the EWS (or group) delay  $t_{\text{EWS}}$ . Whether such a protocol can be implemented for a physically realizable setting remains an open question.

## X. CONCLUDING REMARKS

Within the first decade of the availability of well-controlled and well-characterized attosecond XUV pulses, the field of attosecond chronoscopy has made dramatic progress in observing electronic dynamics in real time. Using photoemission by absorption of an XUV photon and attosecond streaking by an IR field as a prototypical example, we illustrated its potential to provide novel information on electron correlations and electronic transport complementary to information accessible by time-integral spectroscopic techniques. The time delay (or, more precisely, time shift) of the outgoing wave packet relative to the incident XUV pulse has emerged as the key observable accessible by attosecond streaking. This Eisenbud-Wigner-Smith delay  $t_{\text{EWS}}$ , often referred to as the group delay, is an observable associated with the asymptotic scattering state, yet it provides information on the temporal evolution of the electronic wave packet on a length scale of angstroms. For atoms and

molecules,  $t_{\text{EWS}}$  provides critical tests of electron correlation effects in structured continua. Time-resolved photoemission from complex targets such as endohedral  $\text{C}_{60}$  and solid surfaces offers new insights into transport and screening effects on the attosecond scale. Even the time ordering within a coherent sequence of elementary processes becomes accessible by attosecond streaking, as demonstrated for two-photon double ionization of helium.

The search for additional observables related to the timing information accessible by streaking or other attoclocks is still ongoing. Whether or not attosecond streaking can address the controversially debated topic of tunneling time is still an open question. While lifetimes of resonances  $t_{\text{res}}$  delimited by tunneling through potential barriers are accessible by streaking, extraction of the local dwell time in classically forbidden regions remains to be demonstrated. Time-resolved electronic dynamics holds the promise to eventually go beyond observing and clocking the temporal evolution. The ultimate goal will be to actively control and manipulate electrons on the attosecond time and angstrom length scale (Leone *et al.*, 2014). Realization of such a vision, called “light-field electronics” (Goulielmakis *et al.*, 2007; Schiffrin *et al.*, 2012; Schultze *et al.*, 2012), remains a challenge. Future improvements in our understanding of microscopic observables and control knobs in the time domain will be a key prerequisite to meet this challenge.

## ACKNOWLEDGMENTS

The authors thank Sebastian Ecker, Johannes Feist, Christoph Lemell, Qi-Cheng Ning, Liang-You Peng, Stephan Preisinger, Georg Wachter, and Michael Wais for their valuable contributions to this manuscript and Marcus Dahlström, Gopal Dixit, and Anatoli Kheifets for providing data in numerical form. The authors acknowledge fruitful discussions with many colleagues including Andreas Becker, Paul Corkum, Marcus Dahlström, Katharina Doblhoff-Dier, Mette Gaarde, Ulrich Heinzmann, Sebastian Heuser, Kenichi Ishikawa, Misha Ivanov, Anatoli Kheifets, Reinhard Kienberger, Ferenc Krausz, Alfred Maquet, Johan Mauritsson, Stefan Neppl, Mazyar Sabbar, Ken Schafer, Martin Schultze, Uwe Thumm, Karoly Tőkési, Xiao-Min Tong, Hugo van der Haart, and Vlad Yakovlev. This work was supported by the FWF-Austria (SFB NEXTLITE, SFB VICOM, doctoral program W1243 and P23359-N16), and in part by the National Science Foundation through XSEDE resources provided by NICS and TACC under Grant TG-PHY090031. The computational results presented have also been achieved in part using the Vienna Scientific Cluster (VSC). R.P. acknowledges support by the TU Vienna Doctoral Program Functional Matter.

## REFERENCES

- Åberg, T., 1967, *Phys. Rev.* **156**, 35.
- Abrines, R., and I. C. Percival, 1966, *Proc. Phys. Soc. London* **88**, 861.
- Agostini, P., and L. F. DiMauro, 2004, *Rep. Prog. Phys.* **67**, 813.

- Ammosov, M. V., N. B. Delone, and V. P. Krainov, 1986, *Sov. Phys. JETP* **64**, 1191 [<http://www.jetp.ac.ru/cgi-bin/e/index/e/64/6/p1191?a=list>]; *Zh. Eksp. Teor. Fiz.* **91**, 2008 (1986).
- Amusia, M. Y., 1990, *Atomic Photoeffect* (Plenum Press, New York).
- Antoine, P., E. Fomouo, B. Piraux, T. Shimizu, H. Hasegawa, Y. Nabekawa, and K. Midorikawa, 2008, *Phys. Rev. A* **78**, 023415.
- Argenti, L., and E. Lindroth, 2010, *Phys. Rev. Lett.* **105**, 053002.
- Argenti, L., R. Pazourek, J. Feist, S. Nagele, M. Liertzer, E. Persson, J. Burgdörfer, and E. Lindroth, 2013, *Phys. Rev. A* **87**, 053405.
- Aryasetiawan, F., L. Hedin, and K. Karlsson, 1996, *Phys. Rev. Lett.* **77**, 2268.
- Baggesen, J. C., and L. B. Madsen, 2010a, *Phys. Rev. Lett.* **104**, 209903.
- Baggesen, J. C., and L. B. Madsen, 2010b, *Phys. Rev. Lett.* **104**, 043602.
- Baggesen, J. C., and L. B. Madsen, 2011, *Phys. Rev. A* **83**, 021403.
- Baltuska, A., *et al.*, 2003, *Nature (London)* **421**, 611.
- Bandrauk, A. D., and F. Légaré, 2012, “Enhanced ionization of molecules in intense laser fields,” in *Springer Series in Chemical Physics*, Vol. 103, edited by K. Yamanouchi, M. Nisoli, and W. T. Hill (Springer, Berlin/Heidelberg), pp. 29–46.
- Bauer, D., D. Milošević, and W. Becker, 2005, *Phys. Rev. A* **72**, 023415.
- Baz', A. I., 1967a, *Sov. J. Nucl. Phys.* **4**, 182; *Yad. Fiz.* **4**, 252 (1966).
- Baz', A. I., 1967b, *Sov. J. Nucl. Phys.* **5**, 161; *Yad. Fiz.* **5**, 229 (1967).
- Beck, A. R., D. M. Neumark, and S. R. Leone, 2015, *Chem. Phys. Lett.* **624**, 119.
- Bian, X.-B., and A. D. Bandrauk, 2012, *Phys. Rev. Lett.* **108**, 263003.
- Bollé, D., F. Gesztesy, and H. Grosse, 1983, *J. Math. Phys. (N.Y.)* **24**, 1529.
- Borisov, A., D. Sánchez-Portal, A. Kazansky, and P. Echenique, 2013, *Phys. Rev. B* **87**, 121110.
- Bourgain, R., J. Pellegrino, S. Jennewein, Y. R. P. Sortais, and A. Browaeys, 2013, *Opt. Lett.* **38**, 1963.
- Breidbach, J., and L. Cederbaum, 2005, *Phys. Rev. Lett.* **94**, 033901.
- Brenig, W., and R. Haag, 1959, *Fortschr. Phys.* **7**, 183.
- Bucksbaum, P. H., 2007, *Science* **317**, 766.
- Burgdörfer, J., C. Reinhold, J. Sternberg, and J. Wang, 1995, *Phys. Rev. A* **51**, 1248.
- Büttiker, M., 1983, *Phys. Rev. B* **27**, 6178.
- Caillaud, J., A. Maquet, S. Haessler, B. Fabre, T. Ruchon, P. Salières, Y. Mairesse, and R. Taïeb, 2011, *Phys. Rev. Lett.* **106**, 093002.
- Canright, G., 1988, *Phys. Rev. B* **38**, 1647.
- Carette, T., J. M. Dahlström, L. Argenti, and E. Lindroth, 2013, *Phys. Rev. A* **87**, 023420.
- Carpeggiani, P. A., P. Tzallas, A. Palacios, D. Gray, F. Martín, and D. Charalambidis, 2014, *Phys. Rev. A* **89**, 023420.
- Cavaliere, A. L., *et al.*, 2007, *Nature (London)* **449**, 1029.
- Cederbaum, L. S., and J. Zobeley, 1999, *Chem. Phys. Lett.* **307**, 205.
- Chacon, A., M. Lein, and C. Ruiz, 2014, *Phys. Rev. A* **89**, 053427.
- Chang, Z., 2011, *Fundamentals of Attosecond Optics* (CRC Press, New York).
- Chang, Z., and P. Corkum, 2010, *J. Opt. Soc. Am. B* **27**, B9.
- Chelkowski, S., T. Zuo, O. Atabek, and A. Bandrauk, 1995, *Phys. Rev. A* **52**, 2977.
- Chen, S., M. J. Bell, A. R. Beck, H. Mashiko, M. Wu, A. N. Pfeiffer, M. B. Gaarde, D. M. Neumark, S. R. Leone, and K. J. Schafer, 2012, *Phys. Rev. A* **86**, 063408.
- Chen, S., M. Wu, M. Gaarde, and K. Schafer, 2013, *Phys. Rev. A* **87**, 033408.
- Cherepkov, N. A., 1979, *J. Phys. B* **12**, 1279.
- Chini, M., X. Wang, Y. Cheng, and Z. Chang, 2014, *J. Phys. B* **47**, 124009.
- Chirilă, C., and M. Lein, 2006, *Phys. Rev. A* **73**, 023410.
- Chiu, K. W., and J. J. Quinn, 1972, *Am. J. Phys.* **40**, 1847.
- Choi, Y., and A. N. Jordan, 2013, *Phys. Rev. A* **88**, 052128.
- Cirelli, C., M. Sabbar, S. Heuser, R. Boge, M. Lucchini, L. Gallmann, and U. Keller, 2015, *IEEE J. Sel. Top. Quantum Electron.* **21**, 1.
- Clark, C. W., 1979, *Am. J. Phys.* **47**, 683.
- Cohen, H., and U. Fano, 1966, *Phys. Rev.* **150**, 30.
- Cohen-Tannoudji, C., B. Diu, and F. Laloë, 1977, *Quantum Mechanics* (Wiley, New York).
- Connerade, J. P., V. K. Dolmatov, and S. T. Manson, 2000, *J. Phys. B* **33**, 2279.
- Constant, E., V. D. Taranukhin, A. Stolow, and P. B. Corkum, 1997, *Phys. Rev. A* **56**, 3870.
- Cooper, J., 1962, *Phys. Rev.* **128**, 681.
- Corkum, P. B., and F. Krausz, 2007, *Nat. Phys.* **3**, 381.
- Dahlström, J. M., T. Carette, and E. Lindroth, 2012, *Phys. Rev. A* **86**, 061402.
- Dahlström, J. M., D. Guénot, K. Klünder, M. Gisselbrecht, J. Mauritsson, A. L'Huillier, A. Maquet, and R. Taïeb, 2013, *Chem. Phys.* **414**, 53.
- Dahlström, J. M., A. L'Huillier, and A. Maquet, 2012, *J. Phys. B* **45**, 183001.
- Dahlström, J. M., and E. Lindroth, 2014, *J. Phys. B* **47**, 124012.
- Dalgarno, A., and H. R. Sadeghpour, 1992, *Phys. Rev. A* **46**, R3591.
- de Carvalho, C. A. A., and H. M. Nussenzveig, 2002, *Phys. Rep.* **364**, 83.
- Deshmukh, P. C., A. Mandal, S. Saha, A. S. Kheifets, V. K. Dolmatov, and S. T. Manson, 2014, *Phys. Rev. A* **89**, 053424.
- Dimitriou, K., D. Arbó, S. Yoshida, E. Persson, and J. Burgdörfer, 2004, *Phys. Rev. A* **70**, 061401.
- Dixit, G., H. S. Chakraborty, and M. E. Madjet, 2013, *Phys. Rev. Lett.* **111**, 203003.
- Dolmatov, V. K., A. S. Baltenkov, J. P. Connerade, and S. T. Manson, 2004, *Radiat. Phys. Chem.* **70**, 417.
- Dolmatov, V. K., J. L. King, and J. C. Oglesby, 2012, *J. Phys. B* **45**, 105102.
- Dolmatov, V. K., and S. T. Manson, 2008, *J. Phys. B* **41**, 165001.
- Drescher, M., M. Hentschel, R. Kienberger, G. Tempea, C. Spielmann, G. A. Reider, P. B. Corkum, and F. Krausz, 2001, *Science* **291**, 1923.
- Drescher, M., M. Hentschel, R. Kienberger, M. Uiberacker, V. Yakovlev, A. Scrinzi, T. Westerwalbesloh, U. Kleineberg, U. Heinzmann, and F. Krausz, 2002, *Nature (London)* **419**, 803.
- Drescher, M., and F. Krausz, 2005, *J. Phys. B* **38**, S727.
- Dunning, F. B., J. J. Mestayer, C. O. Reinhold, S. Yoshida, and J. Burgdörfer, 2009, *J. Phys. B* **42**, 022001.
- Echenique, P., R. Ritchie, N. Barberán, and J. Inkson, 1981, *Phys. Rev. B* **23**, 6486.
- Eckle, P., A. N. Pfeiffer, C. Cirelli, A. Staudte, R. Dörner, H. G. Müller, M. Büttiker, and U. Keller, 2008, *Science* **322**, 1525.
- Eckle, P., M. Smolarski, P. Schlup, J. Biegert, A. Staudte, M. Schöffler, H. G. Müller, R. Dörner, and U. Keller, 2008, *Nat. Phys.* **4**, 565.
- Eisenbud, L., 1948, “Formal properties of nuclear collisions,” Ph.D. thesis (Princeton University).
- Emmanouilidou, A., A. Staudte, and P. B. Corkum, 2010, *New J. Phys.* **12**, 103024.
- Fano, U., 1969, *Phys. Rev.* **178**, 131.
- Feibelman, P., and D. Eastman, 1974, *Phys. Rev. B* **10**, 4932.
- Feist, J., S. Nagele, R. Pazourek, E. Persson, B. I. Schneider, L. A. Collins, and J. Burgdörfer, 2008, *Phys. Rev. A* **77**, 043420.
- Feist, J., S. Nagele, R. Pazourek, E. Persson, B. I. Schneider, L. A. Collins, and J. Burgdörfer, 2009, *Phys. Rev. Lett.* **103**, 063002.

- Feist, J., S. Nagele, C. Ticknor, B. I. Schneider, L. A. Collins, and J. Burgdörfer, 2011, *Phys. Rev. Lett.* **107**, 093005.
- Feist, J., R. Pazourek, S. Nagele, E. Persson, B. I. Schneider, L. A. Collins, and J. Burgdörfer, 2009, *J. Phys. B* **42**, 134014.
- Feist, J., O. Zatsarinny, S. Nagele, R. Pazourek, J. Burgdörfer, X. Guan, K. Bartschat, and B. I. Schneider, 2014, *Phys. Rev. A* **89**, 033417.
- Fernández, J., O. Fojón, A. Palacios, and F. Martín, 2007, *Phys. Rev. Lett.* **98**, 043005.
- Föhlisch, A., P. Feulner, F. Hennies, A. Fink, D. Menzel, D. Sanchez-Portal, P. M. Echenique, and W. Wurth, 2005, *Nature (London)* **436**, 373.
- Foumouo, E., A. Hamido, P. Antoine, B. Piroux, H. Bachau, and R. Shakeshaft, 2010, *J. Phys. B* **43**, 091001.
- Frasinski, L., K. Codling, P. Hatherly, J. Barr, I. Ross, and W. Toner, 1987, *Phys. Rev. Lett.* **58**, 2424.
- Gaarde, M. B., C. Buth, J. L. Tate, and K. J. Schafer, 2011, *Phys. Rev. A* **83**, 013419.
- Gagnon, J., E. Goulielmakis, and V. S. Yakovlev, 2008, *Appl. Phys. B* **92**, 25.
- Gallagher, T. F., 2005, *Rydberg Atoms*, Cambridge Monographs on Atomic, Molecular and Chemical Physics (Cambridge University Press, Cambridge, England).
- Gallmann, L., C. Cirelli, and U. Keller, 2012, *Annu. Rev. Phys. Chem.* **63**, 447.
- Gallmann, L., J. Herrmann, R. Locher, M. Sabbar, A. Ludwig, M. Lucchini, and U. Keller, 2013, *Mol. Phys.* **111**, 2243.
- Gardiner, C., and P. Zoller, 2004, *Quantum Noise: A Handbook of Markovian and Non-Markovian Quantum Stochastic Methods with Applications to Quantum Optics*, Springer Series in Synergetics (Springer, New York).
- Gilbertson, S., S. D. Khan, Y. Wu, M. Chini, and Z. Chang, 2010, *Phys. Rev. Lett.* **105**, 093902.
- Gilbertson, S., Y. Wu, S. D. Khan, M. Chini, K. Zhao, X. Feng, and Z. Chang, 2010, *Phys. Rev. A* **81**, 043810.
- Goos, F., and H. Hänchen, 1947, *Ann. Phys. (Berlin)* **436**, 333.
- Göppert-Mayer, M., 1931, *Ann. Phys. (Berlin)* **401**, 273.
- Gottfried, K., 1966, *Quantum Mechanics: Fundamentals*, Quantum Mechanics (W. A. Benjamin, New York).
- Goulielmakis, E., V. S. Yakovlev, A. L. Cavalieri, M. Uiberacker, V. Pervak, A. Apolonski, R. Kienberger, U. Kleineberg, and F. Krausz, 2007, *Science* **317**, 769.
- Goulielmakis, E., *et al.*, 2004, *Science* **305**, 1267.
- Goulielmakis, E., *et al.*, 2008, *Science* **320**, 1614.
- Goulielmakis, E., *et al.*, 2010, *Nature (London)* **466**, 739.
- Guan, X., K. Bartschat, and B. I. Schneider, 2011, *Phys. Rev. A* **83**, 043403.
- Guénot, D., *et al.*, 2012, *Phys. Rev. A* **85**, 053424.
- Guénot, D., *et al.*, 2014, *J. Phys. B* **47**, 245602.
- Guzzo, M., J. J. Kas, L. Sponza, C. Giorgetti, F. Sottile, D. Pierucci, M. G. Silly, F. Sirotti, J. J. Rehr, and L. Reining, 2014, *Phys. Rev. B* **89**, 085425.
- Haessler, S., *et al.*, 2009, *Phys. Rev. A* **80**, 011404.
- Hartman, T. E., 1962, *J. Appl. Phys.* **33**, 3427.
- Hauge, E., and J. Støvneng, 1989, *Rev. Mod. Phys.* **61**, 917.
- Heinzmann, U., 2013, in *Attosecond Physics*, Springer Series in Optical Sciences, Vol. 177, edited by L. Plaja, R. Torres, and A. Zähr (Springer, Berlin/Heidelberg), pp. 231–253.
- Heinzmann, U., and J. H. Dil, 2012, *J. Phys. Condens. Matter* **24**, 173001.
- Hentschel, M., R. Kienberger, C. Spielmann, G. A. Reider, N. Milosevic, T. Brabec, P. Corkum, U. Heinzmann, M. Drescher, and F. Krausz, 2001, *Nature (London)* **414**, 509.
- Holler, M., F. Schapper, L. Gallmann, and U. Keller, 2011, *Phys. Rev. Lett.* **106**, 123601.
- Horner, D. A., F. Morales, T. N. Rescigno, F. Martín, and C. W. McCurdy, 2007, *Phys. Rev. A* **76**, 030701(R).
- Hou, X.-F., L.-Y. Peng, Q.-C. Ning, and Q. Gong, 2012, *J. Phys. B* **45**, 074019.
- Hu, S. X., and L. A. Collins, 2006, *Phys. Rev. Lett.* **96**, 073004.
- Hu, S. X., L. A. Collins, and B. I. Schneider, 2009, *Phys. Rev. A* **80**, 023426.
- Huber, R., F. Tauser, A. Brodschelm, M. Bichler, G. Abstreiter, and A. Leitenstorfer, 2001, *Nature (London)* **414**, 286.
- Ishikawa, K. L., and K. Midorikawa, 2005, *Phys. Rev. A* **72**, 013407.
- Itatani, J., J. Levesque, D. Zeidler, H. Niikura, H. Pepin, J. C. Kieffer, P. B. Corkum, and D. M. Villeneuve, 2004, *Nature (London)* **432**, 867.
- Itatani, J., F. Quéré, G. L. Yudin, M. Y. Ivanov, F. Krausz, and P. B. Corkum, 2002, *Phys. Rev. Lett.* **88**, 173903.
- Ito, S., A. Takeda, T. Miyazaki, Y. Yokoyama, M. Saunders, R. J. Cross, H. Takagi, P. Berthet, and N. Dragoe, 2004, *J. Phys. Chem. B* **108**, 3191.
- Ivanov, I. A., A. S. Kheifets, and V. V. Serov, 2012, *Phys. Rev. A* **86**, 063422.
- Ivanov, M., and O. Smirnova, 2011, *Phys. Rev. Lett.* **107**, 213605.
- Jensen, L., and P. T. Van Duijnen, 2005, *Int. J. Quantum Chem.* **102**, 612.
- Joachain, C. J., N. J. Kylstra, and R. M. Potvliege, 2012, *Atoms in Intense Laser Fields* (Cambridge University Press, Cambridge, England).
- Kazansky, A., and P. Echenique, 2009, *Phys. Rev. Lett.* **102**, 177401.
- Kazansky, A. K., N. M. Kabachnik, and I. P. Sazhina, 2008, *Europhys. Lett.* **82**, 13001.
- Keldysh, L. V., 1965, *Sov. Phys. JETP* **20**, 1307 [<http://www.jetp.ac.ru/cgi-bin/e/index/e/20/5/p1307?a=list>]; *Zh. Eksp. Teor. Fiz.* **47**, 1945 (1964).
- Kheifets, A. S., 2013, *Phys. Rev. A* **87**, 063404.
- Kheifets, A. S., and I. A. Ivanov, 2010, *Phys. Rev. Lett.* **105**, 233002.
- Kienberger, R., *et al.*, 2004, *Nature (London)* **427**, 817.
- Kilcoyne, *et al.*, 2010, *Phys. Rev. Lett.* **105**, 213001.
- Kim, K. T., D. M. Villeneuve, and P. B. Corkum, 2014, *Nat. Photonics* **8**, 187.
- Kitzler, M., N. Milosevic, A. Scrinzi, F. Krausz, and T. Brabec, 2002, *Phys. Rev. Lett.* **88**, 173904.
- Klaiber, M., E. Yakaboylu, H. Bauke, K. Hatsagortsyan, and C. Keitel, 2013, *Phys. Rev. Lett.* **110**, 153004.
- Kling, M. F., and M. J. J. Vrakking, 2008, *Annu. Rev. Phys. Chem.* **59**, 463.
- Klünder, K., P. Johnsson, M. Swoboda, A. L'Huillier, G. Sansone, M. Nisoli, M. J. J. Vrakking, K. J. Schafer, and J. Mauritsson, 2013, *Phys. Rev. A* **88**, 033404.
- Klünder, K., *et al.*, 2011, *Phys. Rev. Lett.* **106**, 143002.
- Kolomeitsev, E. E., and D. N. Voskresensky, 2013, *J. Phys. G* **40**, 113101.
- Komninos, Y., T. Mercouris, and C. A. Nicolaides, 2011, *Phys. Rev. A* **83**, 022501.
- Krasovskii, E. E., 2011, *Phys. Rev. B* **84**, 195106.
- Krasovskii, E. E., V. M. Silkin, V. U. Nazarov, P. M. Echenique, and E. V. Chulkov, 2010, *Phys. Rev. B* **82**, 125102.
- Krausz, F., and M. Ivanov, 2009, *Rev. Mod. Phys.* **81**, 163.
- Krausz, F., and M. I. Stockman, 2014, *Nat. Photonics* **8**, 205.
- Kurka, M., *et al.*, 2010, *New J. Phys.* **12**, 073035.
- Lan, P., E. J. Takahashi, and K. Midorikawa, 2011, *Phys. Rev. A* **83**, 063839.

- Landau, L. D., and E. M. Lifshitz, 1958, *Quantum Mechanics: Non-relativistic Theory*, A-W Series in Advanced Physics (Pergamon Press, New York).
- Landauer, R., and T. Martin, 1994, *Rev. Mod. Phys.* **66**, 217.
- Landsman, A. S., and U. Keller, 2015, *Phys. Rep.* **547**, 1.
- Landsman, A. S., M. Weger, J. Maurer, R. Boge, A. Ludwig, S. Heuser, C. Cirelli, L. Gallmann, and U. Keller, 2014, *Optica* **1**, 343.
- Langer, R. E., 1937, *Phys. Rev.* **51**, 669.
- Laulan, S., and H. Bachau, 2003, *Phys. Rev. A* **68**, 013409.
- Lee, J. D., 2012, *Phys. Rev. B* **86**, 035101.
- Lee, J. D., 2013, *Phys. Rev. Lett.* **111**, 027401.
- Lee, T. G., M. S. Pindzola, and F. Robicheaux, 2009, *Phys. Rev. A* **79**, 053420.
- Lein, M., N. Hay, R. Velotta, J. Marangos, and P. Knight, 2002, *Phys. Rev. A* **66**, 023805.
- Lemell, C., S. Neppl, G. Wachter, K. Tőkési, R. Ernstorfer, P. Feulner, R. Kienberger, and J. Burgdörfer, 2015, *Phys. Rev. B* **91**, 241101(R).
- Lemell, C., B. Solleder, K. Tőkési, and J. Burgdörfer, 2009, *Phys. Rev. A* **79**, 062901.
- Lemell, C., K. Tőkési, and J. Burgdörfer, 2012, *J. Phys. Conf. Ser.* **388**, 012048.
- Leone, S. R., *et al.*, 2014, *Nat. Photonics* **8**, 162.
- Lepine, F., M. Y. Ivanov, and M. J. J. Vrakking, 2014, *Nat. Photonics* **8**, 195.
- Liao, Q., and U. Thumm, 2014, *Phys. Rev. Lett.* **112**, 023602.
- Libisch, F., J. Möller, S. Rotter, M. G. Vavilov, and J. Burgdörfer, 2008, *Europhys. Lett.* **82**, 47006.
- Liebsch, A., 1997, *Electronic Excitations at Metal Surfaces*, Interdisciplinary Contributions to Archaeology (Springer, New York).
- Liertzer, M., J. Feist, S. Nagele, and J. Burgdörfer, 2012, *Phys. Rev. Lett.* **109**, 013201.
- MacColl, L., 1932, *Phys. Rev.* **40**, 621.
- Mahan, G., 1970, *Phys. Rev. B* **2**, 4334.
- Mairesse, Y., and F. Quéré, 2005, *Phys. Rev. A* **71**, 011401.
- Maksimchuk, A., M. Kim, J. Workman, G. Korn, J. Squier, D. Du, D. Umstadter, G. Mourou, and M. Bouvier, 1996, *Rev. Sci. Instrum.* **67**, 697.
- Mandelstam, L., and I. Tamm, 1945, *J. Phys. (USSR)* **9**, 249 [[http://link.springer.com/chapter/10.1007%2F978-3-642-74626-0\\_8](http://link.springer.com/chapter/10.1007%2F978-3-642-74626-0_8)].
- Månsson, E. P., *et al.*, 2014, *Nat. Phys.* **10**, 207.
- Maquet, A., 2014 (private communication).
- Maquet, A., J. Caillat, and R. Taïeb, 2014, *J. Phys. B* **47**, 204004.
- Martin, P. A., 1981, *Acta Phys. Austriaca, Suppl.* **23**, 157.
- Mauritsson, J., M. Gaarde, and K. Schafer, 2005, *Phys. Rev. A* **72**, 013401.
- Mauritsson, J., *et al.*, 2010, *Phys. Rev. Lett.* **105**, 053001.
- McCurdy, C. W., M. Baertschy, and T. N. Rescigno, 2004, *J. Phys. B* **37**, R137.
- McDonald, C. R., G. Orlando, G. Vampa, and T. Brabec, 2013, *Phys. Rev. Lett.* **111**, 090405.
- McDowell, R. C., and J. P. Coleman, 1970, *Introduction to the theory of ion-atom collisions* (North-Holland Pub. Co., Amsterdam).
- Mercouris, T., Y. Komninos, and C. A. Nicolaidis, 2010, *Adv. Quantum Chem.* **60**, 333.
- Möbus, B., B. Magel, K. H. Schartner, B. Langer, U. Becker, M. Wildberger, and H. Schmoranzler, 1993, *Phys. Rev. A* **47**, 3888.
- Moore, L. R., M. A. Lysaght, J. S. Parker, H. W. van der Hart, and K. T. Taylor, 2011, *Phys. Rev. A* **84**, 061404.
- Morishita, T., S. Watanabe, and C. D. Lin, 2007, *Phys. Rev. Lett.* **98**, 083003.
- Muga, G., R. S. Mayato, and I. Egusquiza, 2007, *Time in Quantum Mechanics*, Lecture Notes in Physics Vol. 1 (Springer, New York).
- Muller, H. G., 2002, *Appl. Phys. B* **74**, s17.
- Murnane, M. M., H. C. Kapteyn, and R. W. Falcone, 1990, *Appl. Phys. Lett.* **56**, 1948.
- Nabekawa, Y., H. Hasegawa, E. J. Takahashi, and K. Midorikawa, 2005, *Phys. Rev. Lett.* **94**, 043001.
- Nagele, S., R. Pazourek, J. Feist, and J. Burgdörfer, 2012, *Phys. Rev. A* **85**, 033401.
- Nagele, S., R. Pazourek, J. Feist, K. Doblhoff-Dier, C. Lemell, K. Tőkési, and J. Burgdörfer, 2011, *J. Phys. B* **44**, 081001.
- Nagele, S., R. Pazourek, M. Wais, G. Wachter, and J. Burgdörfer, 2014, *J. Phys. Conf. Ser.* **488**, 012004.
- Nagele, S., M. Wais, G. Wachter, R. Pazourek, and J. Burgdörfer, 2015 (unpublished).
- Neppl, S., 2012, "Attosecond Time-Resolved Photoemission from Surfaces and Interfaces," Ph.D. thesis (Technische Universität München, München).
- Neppl, S., R. Ernstorfer, E. M. Bothschafter, A. L. Cavalieri, D. Menzel, J. V. Barth, F. Krausz, R. Kienberger, and P. Feulner, 2012, *Phys. Rev. Lett.* **109**, 087401.
- Neppl, S., *et al.*, 2015, *Nature (London)* **517**, 342.
- Nepstad, R., T. Birkeland, and M. Førre, 2010, *Phys. Rev. A* **81**, 063402.
- Nicholson, R. J. F., I. E. McCarthy, and W. Weyrich, 1999, *J. Phys. B* **32**, 3873.
- Nikolopoulos, L. A. A., and P. Lambropoulos, 2007, *J. Phys. B* **40**, 1347.
- Ning, Q.-C., L.-Y. Peng, S.-N. Song, W.-C. Jiang, S. Nagele, R. Pazourek, J. Burgdörfer, and Q. Gong, 2014, *Phys. Rev. A* **90**, 013423.
- Olkhovskiy, V. S., E. Recami, and J. Jakiel, 2004, *Phys. Rep.* **398**, 133.
- Orlando, G., C. R. McDonald, N. H. Protik, G. Vampa, and T. Brabec, 2014, *J. Phys. B* **47**, 204002.
- Ortiz, J. V., 2003, *Int. J. Quantum Chem.* **95**, 593.
- Ott, C., A. Kaldun, P. Raith, K. Meyer, M. Laux, J. Evers, C. H. Keitel, C. H. Greene, and T. Pfeifer, 2013, *Science* **340**, 716.
- Ott, C., *et al.*, 2014, *Nature (London)* **516**, 374.
- Pabst, S., L. Greenman, P. J. Ho, D. A. Mazziotti, and R. Santra, 2011, *Phys. Rev. Lett.* **106**, 053003.
- Pabst, S., A. Sytcheva, A. Moulet, A. Wirth, E. Goulielmakis, and R. Santra, 2012, *Phys. Rev. A* **86**, 063411.
- Palacios, A., T. N. Rescigno, and C. W. McCurdy, 2008, *Phys. Rev. A* **77**, 032716.
- Palacios, A., T. N. Rescigno, and C. W. McCurdy, 2009, *Phys. Rev. A* **79**, 033402.
- Palatchi, C., J. M. Dahlström, A. S. Kheifets, I. A. Ivanov, D. M. Canaday, P. Agostini, and L. F. DiMauro, 2014, *J. Phys. B* **47**, 245003.
- Palik, E. D., 1998, *Handbook of Optical Constants of Solids*, Vol. 3 (Academic Press, New York).
- Paul, P. M., E. S. Toma, P. Breger, G. Mullot, F. Audebert, P. Balcou, H. G. Muller, and P. Agostini, 2001, *Science* **292**, 1689.
- Pauli, W., 1926, in *Handbuch der Physik*, Vol. 23, edited by H. Geiger and K. Scheel, 1st ed. (Springer, Berlin/Heidelberg), pp. 1–278.
- Pauli, W., 1933, in *Handbuch der Physik*, Vol. 24, edited by H. Geiger and K. Scheel, 2nd ed. (Springer, Berlin/Heidelberg), pp. 83–272.
- Pazourek, R., J. Feist, S. Nagele, and J. Burgdörfer, 2012, *Phys. Rev. Lett.* **108**, 163001.
- Pazourek, R., J. Feist, S. Nagele, E. Persson, B. I. Schneider, L. A. Collins, and J. Burgdörfer, 2011, *Phys. Rev. A* **83**, 053418.

- Pazourek, R., S. Nagele, and J. Burgdörfer, 2013, *Faraday Discuss.* **163**, 353.
- Pazourek, R., S. Nagele, and J. Burgdörfer, 2015, *J. Phys. B* **48**, 061002.
- Pazourek, R., S. Nagele, K. Doblhoff-Dier, J. Feist, C. Lemell, K. Tökési, and J. Burgdörfer, 2012, *J. Phys. Conf. Ser.* **388**, 012029.
- Peng, L.-Y., W.-C. Jiang, J.-W. Geng, W.-H. Xiong, and Q. Gong, 2015, *Phys. Rep.* **575**, 1.
- Pfeiffer, A. N., C. Cirelli, M. Smolarski, D. Dimitrovski, M. Abu-samha, L. B. Madsen, and U. Keller, 2011, *Nat. Phys.* **8**, 76.
- Pfeiffer, A. N., C. Cirelli, M. Smolarski, R. Dörner, and U. Keller, 2011, *Nat. Phys.* **7**, 428.
- Pfeiffer, A. N., C. Cirelli, M. Smolarski, and U. Keller, 2013, *Chem. Phys.* **414**, 84.
- Plaja, L., R. Torres, and A. Zaïr, 2013, *Attosecond Physics: Attosecond Measurements and Control of Physical Systems*, Springer Series in Optical Sciences (Springer London, Limited, London).
- Price, H., A. Staudte, P. B. Corkum, and A. Emmanouilidou, 2012, *Phys. Rev. A* **86**, 053411.
- Price, H., A. Staudte, and A. Emmanouilidou, 2011, *New J. Phys.* **13**, 093006.
- Quéré, F., Y. Mairesse, and J. Itatani, 2005, *J. Mod. Opt.* **52**, 339.
- Reider, G. A., 2004, *J. Phys. D* **37**, R37.
- Rosker, M. J., M. Dantus, and A. H. Zewail, 1988, *J. Chem. Phys.* **89**, 6113.
- Rotter, S., P. Ambichl, and F. Libisch, 2011, *Phys. Rev. Lett.* **106**, 120602.
- Rüdel, A., R. Hentges, U. Becker, H. Chakraborty, M. Madjet, and J. Rost, 2002, *Phys. Rev. Lett.* **89**, 125503.
- Rudenko, A., *et al.*, 2008, *Phys. Rev. Lett.* **101**, 073003.
- Runge, E., and E. K. U. Gross, 1984, *Phys. Rev. Lett.* **52**, 997.
- Sabbar, M., S. Heuser, R. Boge, M. Lucchini, T. Carette, E. Lindroth, L. Gallmann, C. Cirelli, and U. Keller, 2015, *arXiv:1407.6623*.
- Saha, S., A. Mandal, J. Jose, H. R. Varma, P. C. Deshmukh, A. S. Kheifets, V. K. Dolmatov, and S. T. Manson, 2014, *Phys. Rev. A* **90**, 053406.
- Salecker, H., and E. Wigner, 1958, *Phys. Rev.* **109**, 571.
- Samson, J. A. R., and W. C. Stolte, 2002, *J. Electron Spectrosc. Relat. Phenom.* **123**, 265.
- Sansone, G., *et al.*, 2006, *Science* **314**, 443.
- Santra, R., V. S. Yakovlev, T. Pfeifer, and Z.-H. Loh, 2011, *Phys. Rev. A* **83**, 033405.
- Sassoli de Bianchi, M., 2012, *Open Phys.* **10**, 282.
- Sayers, D., E. Stern, and F. Lytle, 1971, *Phys. Rev. Lett.* **27**, 1204.
- Schiffrin, A., *et al.*, 2012, *Nature (London)* **493**, 70.
- Schoun, S. B., R. Chirla, J. Wheeler, C. Roedig, P. Agostini, L. F. DiMauro, K. J. Schafer, and M. B. Gaarde, 2014, *Phys. Rev. Lett.* **112**, 153001.
- Schultz, T., and M. Vrakking, 2013, *Attosecond and XUV Spectroscopy: Ultrafast Dynamics and Spectroscopy* (Wiley, New York).
- Schultze, M., *et al.*, 2010, *Science* **328**, 1658.
- Schultze, M., *et al.*, 2012, *Nature (London)* **493**, 75.
- Scrinzi, A., M. Y. Ivanov, R. Kienberger, and D. M. Villeneuve, 2006, *J. Phys. B* **39**, R1.
- Scully, M. O., and M. S. Zubairy, 1997, *Quantum Optics* (Cambridge University Press, Cambridge, England).
- Serov, V. V., V. L. Derbov, and T. A. Sergeeva, 2013, *Phys. Rev. A* **87**, 063414.
- Shafir, D., H. Soifer, B. D. Bruner, M. Dagan, Y. Mairesse, S. Patchkovskii, M. Y. Ivanov, O. Smirnova, and N. Dudovich, 2012, *Nature (London)* **485**, 343.
- Shepherd, R., R. Booth, D. Price, M. Bowers, D. Swan, J. Bonlie, B. Young, J. Dunn, B. White, and R. Stewart, 1995, *Rev. Sci. Instrum.* **66**, 719.
- Smirnova, O., A. S. Mouritzen, S. Patchkovskii, and M. Y. Ivanov, 2007, *J. Phys. B* **40**, F197.
- Smirnova, O., M. Spanner, and M. Y. Ivanov, 2006, *J. Phys. B* **39**, S323.
- Smith, F. T., 1960, *Phys. Rev.* **118**, 349.
- Sokolovski, D., S. Brouard, and J. Connor, 1994, *Phys. Rev. A* **50**, 1240.
- Sorokin, A. A., M. Wellhofer, S. V. Bobashev, K. Tiedtke, and M. Richter, 2007, *Phys. Rev. A* **75**, 051402(R).
- Śpiewanowski, M. D., and L. B. Madsen, 2012, *Phys. Rev. A* **86**, 045401.
- Stapelfeldt, H., E. Constant, and P. Corkum, 1995, *Phys. Rev. Lett.* **74**, 3780.
- Starace, A., 2006, in *Springer Handbook of Atomic, Molecular, and Optical Physics*, edited by G. Drake, Chap. 24 (Springer, New York), pp. 379–390.
- Staudte, A., *et al.*, 2007, *Phys. Rev. Lett.* **98**, 073003.
- Steinberg, A., 1995, *Phys. Rev. Lett.* **74**, 2405.
- Stern, E. A., and S. M. Heald, 1983, “Basic Principles and Applications of EXAFS,” *Handbook on Synchrotron Radiation*, Chap. 1, pp. 955–1014.
- Su, J., H. Ni, A. Becker, and A. Jaroń-Becker, 2013a, *Phys. Rev. A* **88**, 023413.
- Su, J., H. Ni, A. Becker, and A. Jaroń-Becker, 2013b, *Phys. Rev. A* **87**, 033420.
- Su, J., H. Ni, A. Becker, and A. Jaron-Becker, 2013c, *J. Mod. Opt.* **60**, 1484.
- Su, J., H. Ni, A. Becker, and A. Jaroń-Becker, 2014, *Phys. Rev. A* **89**, 013404.
- Su, J., H. Ni, A. Jaroń-Becker, and A. Becker, 2014, *Phys. Rev. Lett.* **113**, 263002.
- Sukiasyan, S., K. L. Ishikawa, and M. Ivanov, 2012, *Phys. Rev. A* **86**, 033423.
- Svensson, S., B. Eriksson, N. Mårtensson, G. Wendin, and U. Gelius, 1988, *J. Electron Spectrosc. Relat. Phenom.* **47**, 327.
- Swoboda, M., T. Fordell, K. Klünder, J. M. Dahlström, M. Miranda, C. Buth, K. J. Schafer, J. Mauritsson, A. L’Huillier, and M. Gisselbrecht, 2010, *Phys. Rev. Lett.* **104**, 103003.
- Takahashi, E. J., P. Lan, O. D. Mücke, Y. Nabekawa, and K. Midorikawa, 2010, *Phys. Rev. Lett.* **104**, 233901.
- Takemoto, N., and A. Becker, 2010, *Phys. Rev. Lett.* **105**, 203004.
- Tanuma, S., C. J. Powell, and D. R. Penn, 2011, *Surf. Interface Anal.* **43**, 689.
- Taylor, J. R., 1974, *Nuovo Cimento Soc. Ital. Fis.*, B **23**, 313.
- Toma, E. S., and H. G. Muller, 2002, *J. Phys. B* **35**, 3435.
- Tzallas, P., E. Skantzakis, L. A. A. Nikolopoulos, G. D. Tsakiris, and D. Charalambidis, 2011, *Nat. Phys.* **7**, 781.
- Uiberacker, M., *et al.*, 2007, *Nature (London)* **446**, 627.
- Vager, Z., R. Naaman, and E. P. Kanter, 1989, *Science* **244**, 426.
- Véniard, V., R. Taïeb, and A. Maquet, 1996, *Phys. Rev. A* **54**, 721.
- Vozzi, C., *et al.*, 2005, *Phys. Rev. Lett.* **95**, 153902.
- Vozzi, C., *et al.*, 2006, *J. Phys. B* **39**, S457.
- Wachter, G., 2014, “Simulation of condensed matter dynamics in strong femtosecond laser pulses,” Ph.D. thesis (Vienna University of Technology).
- Wachter, G., C. Lemell, J. Burgdörfer, S. A. Sato, X.-M. Tong, and K. Yabana, 2014, *Phys. Rev. Lett.* **113**, 087401.
- Wachter, G., C. Lemell, J. Burgdörfer, M. Schenk, M. Krüger, and P. Hommelhoff, 2012, *Phys. Rev. B* **86**, 035402.

- Wais, M., 2014, "Time-resolved photoemission from endohedral fullerenes using attosecond streaking," Bachelor's thesis (Vienna University of Technology).
- Wang, H., M. Chini, S. Chen, C. H. Zhang, F. He, Y. Cheng, Y. Wu, U. Thumm, and Z. Chang, 2010, *Phys. Rev. Lett.* **105**, 143002.
- Wätzel, J., A. S. Moskalenko, Y. Pavlyukh, and J. Berakdar, 2015, *J. Phys. B* **48**, 025602.
- Weiss, U., 2012, *Quantum Dissipative Systems*, Series in Modern Condensed Matter Physics (World Scientific, Singapore).
- Wickenhauser, M., J. Burgdörfer, F. Krausz, and M. Drescher, 2005, *Phys. Rev. Lett.* **94**, 023002.
- Wickenhauser, M., J. Burgdörfer, F. Krausz, and M. Drescher, 2006, *J. Mod. Opt.* **53**, 247.
- Wigner, E. P., 1955, *Phys. Rev.* **98**, 145.
- Winful, H. G., 2006, *Phys. Rep.* **436**, 1.
- Wirth, A., R. Santra, and E. Goulielmakis, 2013, *Chem. Phys.* **414**, 149.
- Xu, M.-H., L.-Y. Peng, Z. Zhang, Q. Gong, X.-M. Tong, E. A. Pronin, and A. F. Starace, 2011, *Phys. Rev. Lett.* **107**, 183001.
- Yabana, K., and G. F. Bertsch, 1993, *Phys. Scr.* **48**, 633.
- Yakovlev, V. S., F. Bammer, and A. Scrinzi, 2005, *J. Mod. Opt.* **52**, 395.
- Yakovlev, V. S., J. Gagnon, N. Karpowicz, and F. Krausz, 2010, *Phys. Rev. Lett.* **105**, 073001.
- Yudin, G., A. Bandrauk, and P. Corkum, 2006, *Phys. Rev. Lett.* **96**, 063002.
- Yudin, G. L., S. Chelkowski, J. Itatani, A. D. Bandrauk, and P. B. Corkum, 2005, *Phys. Rev. A* **72**, 051401.
- Zatsarinny, O., 2006, *Comput. Phys. Commun.* **174**, 273.
- Zatsarinny, O., and C. Froese Fischer, 2009, *Comput. Phys. Commun.* **180**, 2041.
- Zewail, A. H., 1988, *Science* **242**, 1645.
- Zewail, A. H., 2000a, *Angew. Chem., Int. Ed. Engl.* **39**, 2586.
- Zewail, A. H., 2000b, *Pure Appl. Chem.* **72**, 2219.
- Zhang, C. H., and U. Thumm, 2009, *Phys. Rev. Lett.* **102**, 123601.
- Zhang, C. H., and U. Thumm, 2010, *Phys. Rev. A* **82**, 043405.
- Zhang, C. H., and U. Thumm, 2011a, *Phys. Rev. A* **84**, 065403.
- Zhang, C. H., and U. Thumm, 2011b, *Phys. Rev. A* **84**, 063403.
- Zhang, C. H., and U. Thumm, 2011c, *Phys. Rev. A* **84**, 033401.
- Zhao, J., and M. Lein, 2013, *Phys. Rev. Lett.* **111**, 043901.
- Zhao, K., Q. Zhang, M. Chini, Y. Wu, X. Wang, and Z. Chang, 2012, *Opt. Lett.* **37**, 3891.
- Zurek, W. H., 2003, *Rev. Mod. Phys.* **75**, 715.